



ADVANCING C1 CATALYSIS BY SPATIOTEMPORAL ANALYSIS AND DYNAMIC OPERATION

Lingjun Hu

ADVERTIMENT. L'accés als continguts d'aquesta tesi doctoral i la seva utilització ha de respectar els drets de la persona autora. Pot ser utilitzada per a consulta o estudi personal, així com en activitats o materials d'investigació i docència en els termes establerts a l'art. 32 del Text Refós de la Llei de Propietat Intel·lectual (RDL 1/1996). Per altres utilitzacions es requereix l'autorització prèvia i expressa de la persona autora. En qualsevol cas, en la utilització dels seus continguts caldrà indicar de forma clara el nom i cognoms de la persona autora i el títol de la tesi doctoral. No s'autoritza la seva reproducció o altres formes d'explotació efectuades amb finalitats de lucre ni la seva comunicació pública des d'un lloc aliè al servei TDX. Tampoc s'autoritza la presentació del seu contingut en una finestra o marc aliè a TDX (framing). Aquesta reserva de drets afecta tant als continguts de la tesi com als seus resums i índexs.

ADVERTENCIA. El acceso a los contenidos de esta tesis doctoral y su utilización debe respetar los derechos de la persona autora. Puede ser utilizada para consulta o estudio personal, así como en actividades o materiales de investigación y docencia en los términos establecidos en el art. 32 del Texto Refundido de la Ley de Propiedad Intelectual (RDL 1/1996). Para otros usos se requiere la autorización previa y expresa de la persona autora. En cualquier caso, en la utilización de sus contenidos se deberá indicar de forma clara el nombre y apellidos de la persona autora y el título de la tesis doctoral. No se autoriza su reproducción u otras formas de explotación efectuadas con fines lucrativos ni su comunicación pública desde un sitio ajeno al servicio TDR. Tampoco se autoriza la presentación de su contenido en una ventana o marco ajeno a TDR (framing). Esta reserva de derechos afecta tanto al contenido de la tesis como a sus resúmenes e índices.

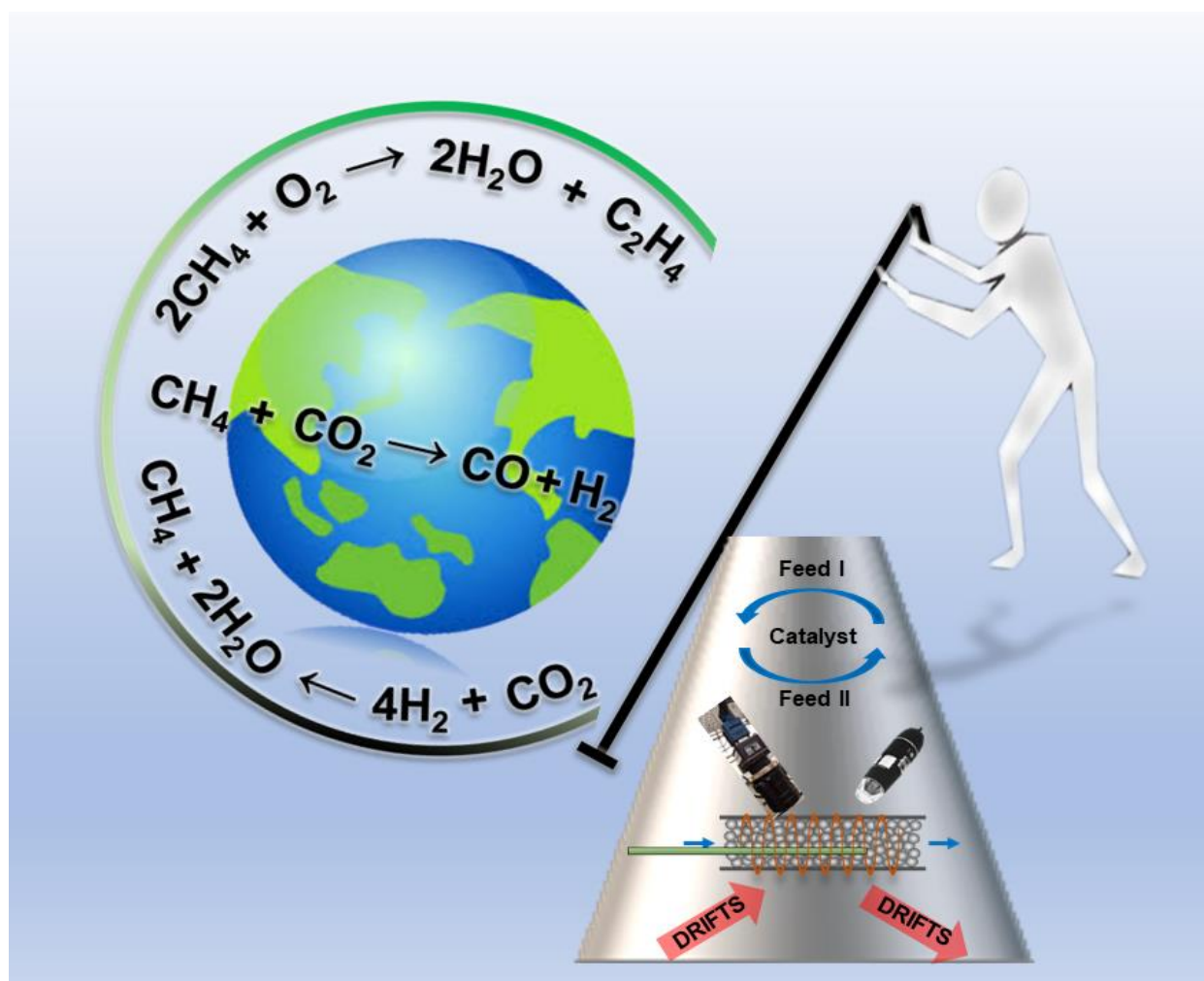
WARNING. Access to the contents of this doctoral thesis and its use must respect the rights of the author. It can be used for reference or private study, as well as research and learning activities or materials in the terms established by the 32nd article of the Spanish Consolidated Copyright Act (RDL 1/1996). Express and previous authorization of the author is required for any other uses. In any case, when using its content, full name of the author and title of the thesis must be clearly indicated. Reproduction or other forms of for profit use or public communication from outside TDX service is not allowed. Presentation of its content in a window or frame external to TDX (framing) is not authorized either. These rights affect both the content of the thesis and its abstracts and indexes.



UNIVERSITAT ROVIRA I VIRGILI

Advancing C1 catalysis by spatiotemporal analysis and dynamic operation

LINGJUN HU



DOCTORAL THESIS

2020

DOCTORAL THESIS

ADVANCING C1 CATALYSIS BY SPATIOTEMPORAL ANALYSIS AND DYNAMIC OPERATION

LINGJUN HU

Supervised by:

Prof. Dr. Atsushi Urakawa

ICIQ-URV



UNIVERSITAT
ROVIRA I VIRGILI

Tarragona

2020

Prof. Dr. Atsushi Urakawa Group

Leader

Institute of Chemical Research of Catalonia (ICIQ) The
Barcelona Institute of Science and Technology Av. Països
Catalans 16
43007 Tarragona, Spain

CERTIFIES THAT:

The present study, entitled “Advancing C1 catalysis by spatiotemporal analysis and dynamic operation”, presented by Lingjun Hu for the award of the degree of Doctor, has been carried out under my supervision at the Institute of Chemical Research of Catalonia (ICIQ), and that it fulfils all the requirements to obtain the Degree of Doctor in Chemical Science and Technology.

Tarragona, 7th of April, 2020

Doctoral Thesis Supervisor

浦川 篤

Prof. Dr. Atsushi Urakawa



UNIVERSITAT
ROVIRA i VIRGILI

ACKNOWLEDGEMENTS

A PhD studying with four years and four months is very short in terms of the whole life of one person, but could be a very long journey for the person who really experienced it. I am so grateful to all the people who I have met during this journey. It is them who made the period of time such a special adventure in my life.

First of all, I would like to express my deep gratitude to my thesis supervisor, Prof. Dr. Atsushi Urakawa. Thanks for offering me the opportunity to start my PhD in Institute of Chemical Research of Catalonia (ICIQ). Doing research with him is really an impressive experience. I cannot forget the shiny star in his eyes when he was explaining us the charm of spectroscopy or talking about chemistry. His passion to science and optimism to life always cheer me up, encourage me to overcome the obstacles on the way. Although it has always been tough time to meet his perfectionism about work, I have to admit that is where I grow most. Sincerely, ありがとうございます, 浦川先生!

I would like to thank Prof. Rosa Caballol Lorenzo, my Coordinator from University of Rovira i Virgili (URV). Your care and kindness are so warm. I am so grateful for having you taking care of our administrative management in URV. Muchas gracias!

I would like to thank all the staff in ICIQ who gave me their hands when I needed. Special thanks to Georgiana and Dolores in Heterogeneous Catalysis Unit, Jose Luis in Mechanical Workshop, Xavier Asensio in Glass Blowing Workshop), Marta in X-ray Diffraction Unit, Leticia and Mara in Human Resource. Your professional work made my life and work in Tarragona much easier. Muchas gracias!

I would also like to express my sincere gratitude to the staff that came across my path in Delft University of Technology (TUD), especially the catalysis engineering (CE) group. Special thanks to Els Arkesteijn, Willy Rook, Liliana Baron and Harrie Jansma. With your kind help, I could start my stay in TUD easily. Huge support from Bart van der Linden is highly appreciated. Your efficient and reliable work have solved so many problems on my way. Hartelijk bedankt! Many thanks to the lab mates in Building 58, Han, Adrian, David, Robert, Jiayou, Xuerui, Xinlei, Riming, Chuncheng, Srinidhi, Tomas, Disha, Kevin, Dean, Adarsh, Viraisha, Stefano, Giacomo, and many others. Your kind help and warm company made me enjoy my stay in TUD. Thanks to all of you!

Of course, I would like to thank the Urakawa group members. Great thanks to Sergio Roso, Yi Zhang, Andrea Alvarez, Rohit Gaikwad, Marta Borges, Dragos Constantin Stoian, Muralidhar Chourashiya, Damien Cornu, Rui Huang, Joan Giner, Silvia Caminero Huertas, Shunsaku Yasumura, Shintaro Hara, Takuya Sukanuma. As the 'smallest' lady in the lab, I am really grateful for all the men and women power you have lent me. Special thanks to Atul Bansode. Your strong background in

engineering and creative ideas removed so many technical problems on my way building setups. Your assistance on LabVIEW programming is also highly acknowledged. खूप खूप धन्यवाद! The remote support from Tsuyoshi Hyakutake is also very appreciated. ありがとうございます! Many thanks to Jordi Ampurdanés. I benefited so much from your patient instructions on the operation of instruments in the lab, especially the time- and spatial- resolved diffuse reflectance infrared fourier transform spectroscopy (DRIFTS). Merci! The great assistance of interpreting Spanish from Juan José Corral (and the care from your mom) is also appreciated and unforgettable. Muchas gracias guapo! Special thanks to our secretary, Aurora Càceres. You made my other Chinese friends envy me a lot because of your kind and full-scale care. Muchas gracias! Many thanks to Sorin Bunea (and your wife) and Nat Phongprueksathat. Your kind support and warm company during my stay in TUD are really appreciated. Mulțumesc foarte mult! ขอขอบคุณมาก! At the end, great thanks to my best collaborators, Donato Pinto and Reina Kaneda. Your efficient and reliable work gave me the best support. Grazie mille! ありがとうございます! The lab time in P211 had some joys because of all my best colleagues! Those calçot, barbecue, beers (water for me), crazy dancing, Christmas dinner and so much fun we had together, are unforgettable memories for me, as well as those complains and arguments. Lots of thanks to all of you, my lovely colleagues!

I would also like to express my sincere thanks to the Chinese communities in Tarragona and Delft. The life abroad these years is much easier and has more fun because of all of you. 谢谢!

非常感谢我的家人。感谢爸妈，尽管一开始你们并不赞同我出国读博，却不曾收回一丝对我的关心，一如既往的默默护我前行。感谢哥哥，虽然你总是挑剔我，但也是你，愿意拿出所有，全力支持我去追逐自己梦想。感谢嫂子，谢谢你与哥哥一起照顾爸妈，守护我们的大家，让我在千里之外安心做自己的事。感谢在巴黎的另一个大家庭，谢谢你们四年多来的关心和照顾，让我在异乡不曾有异乡之感。 Je souhaiterai remercier particulièrement mon mari. Merci pour ses encouragements et son soutien continu. Sa confiance en moi m'a éclairé la voie qui, par moment, a été obstruée par les problèmes du travail et de la vie. Je suis très reconnaissante pour ses supports techniques en programmation, langage, etc. Merci beaucoup!

At the end, URV, TUD, ICIQ Foundation, especially Precursory Research for Embryonic Science and Technology program (PRESTO) from Japan Science and Technology Agency (JST) are kindly acknowledged for financial support, and Repsol is appreciated for allowing us using their equipment during my first year of PhD studying. They all together make this doctoral project possible.



Table of Contents

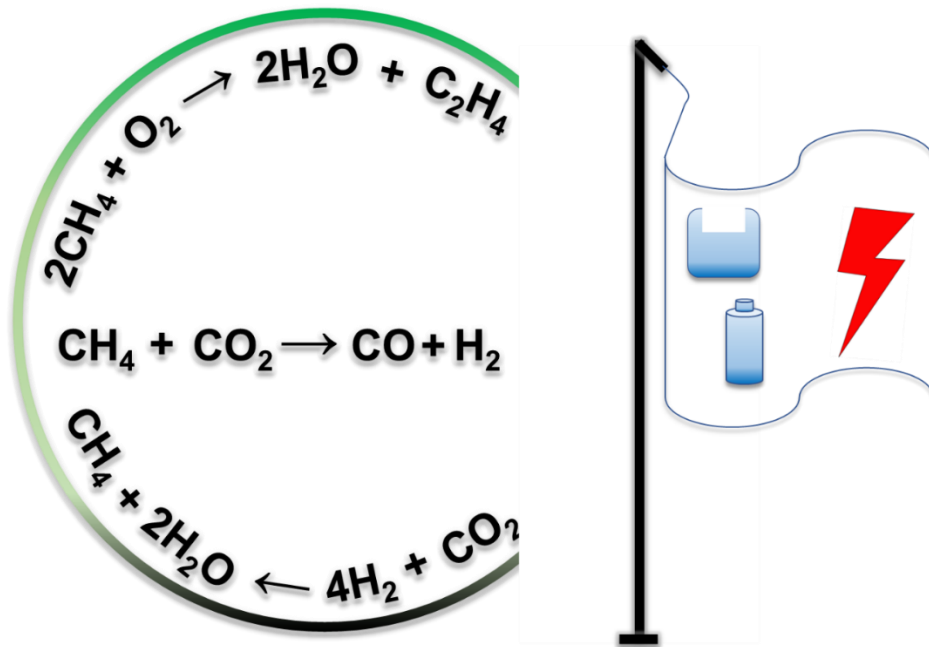
1 Introduction and overviews	1
1.1 The dilemma related to the consumption of fossil fuel resources	2
1.2 C1 chemistry: the solution to the dilamma	4
1.3 Oxidative coupling of methane	6
1.3.1 A brief historical evolution of OCM	6
1.3.2 OCM reaction mechanism	7
1.3.2.1 C ₂ H ₆ formation	7
1.3.2.2 C ₂ H ₄ formation	8
1.3.2.3 CO _x formation	8
1.3.3 Challenges for OCM	10
1.3.3.1 Trade-off between CH ₄ conversion and C ₂ selectivity	10
1.3.3.2 Interconnectedness of influencing factors for OCM	13
1.3.3.3 Spatial gradients present in the OCM system	15
1.4 CO ₂ hydrogenation reaction	19
1.4.1 Brief review of several CO ₂ hydrogenation pathways	19
1.4.2 CO ₂ methanation development	20
1.5 Dry reforming of methane	24
1.5.1 The advantage, the challenge, and the exploration	24
1.5.2 A new path: Chemical looping dry reforming of methane	27
1.6 Aim and overview of the thesis	29
Bibliography	31
2 Materials and methods	39
2.1 Catalysts synthesis	40
2.1.1 Impregnation method	40
2.1.2 Mechanical milling method	40
2.2 Catalyst characterization tools	40

2.3 Reaction systems and <i>operando</i> measurement setups	41
2.3.1 CO ₂ capture and reduction (CCR) reaction system	41
2.3.2 CCR Space- and time-resolved <i>operando</i> DRIFTS	42
2.3.3 Oxidative coupling of methane (OCM) and dry reforming of methane (DRM) reaction system	42
2.3.4 Spatial analysis module	46
2.3.5 Visualization analysis module	47
2.3.6 Microwave reactor system	49
2.4 Methods	50
2.4.1 Alpha calibration	50
2.4.2 IR camera calibration	52
2.4.3 Reaction operation and data analysis	54
2.4.4 Catalytic activity characterization parameters	57
Bibliography	58
3 OCM in cofeed mode	59
3.1 Introduction	60
3.2 Experimental	61
3.2.1 Catalyst preparation	61
3.2.2 Catalyst characterization	61
3.2.3 Catalytic reactions	61
3.2.4 Spatial analysis and visual inspection	62
3.3 Results and discussion	62
3.4 Conclusion	68
Bibliography	69
4 OCM under unsteady state operation	71
4.1 Introduction	72
4.2 Experimental	73
4.2.1 Catalyst preparation	73
4.2.2 Catalytic reactions	73

4.3 Results and discussion	74
4.4 Conclusion	80
Bibliography	81
5 Microwave-assisted oxidative coupling of methane	83
5.1 Introduction	84
5.2 Experimental	85
5.2.1 Catalyst preparation	85
5.2.2 Catalytic reactions	85
5.3 Results and discussion	86
5.3.1 Activation of customized microwave reactor for OCM reaction	86
5.3.2 The effect of microwave heating on MgO-based catalysts for OCM reaction	88
5.3.3 The effect of microwave heating on La ₂ O ₃ -based catalysts for OCM reaction	90
5.4 Conclusion	93
Bibliography	95
6 CO₂ hydrogenation	97
6.1 Introduction	98
6.2 Experimental	99
6.2.1 Materials and catalyst preparation	99
6.2.2 Catalyst characterization	99
6.2.3 Catalytic reaction	100
6.2.4 Space- and time-resolved DRIFTS	101
6.3 Results and discussion	101
6.3.1 CCR performance of unpromoted and K- or La-promoted Ni/ZrO ₂ catalysts	101
6.3.2 Catalyst characterization	107
6.3.3 Space- and time-resolved operando DRIFTS	110
6.4 Conclusions	114
Bibliography	116
7 Dry reforming of methane	117
7.1 Introduction	118

7.2 Experimental.....	119
7.2.1 Materials and catalyst preparation.....	119
7.2.2 Catalyst characterization	119
7.2.3 Catalytic reaction	119
7.3 Results and discussion.....	121
7.3.1 The effect of different support materials	122
7.3.2 Temperature effect on CO ₂ conversion and CH ₄ decomposition.....	123
7.3.3 The effect of different promoters (Fe, K, La).....	125
7.3.4 The effect of CH ₄ phase length on CO ₂ conversion.....	129
7.4 Conclusion.....	130
Bibliography.....	132
8 Conclusion and outlook.....	133
8.1 Summary of the thesis	134
8.2 Outlook	137
Bibliography.....	140
9 Appendices.....	141
Shorthand and glossary	151
List of publications	153
Curriculum vitae	157

1 INTRODUCTION AND OVERVIEWS



1.1 The dilemma related to the consumption of fossil fuel resources

Modern chemical industrials strongly rely on crude oil and its consumption grows very fast and even faster than its production as shown in Figure 1.1. The limited reserves (around 1.7×10^{12} barrels proved by 2018) calls for more abundant substitutions¹. Methane, the main component in natural gas, has been considered as a promising substitution. The increasing natural gas reserves shown in Figure 1.2 guarantees relatively abundant availability of methane¹.

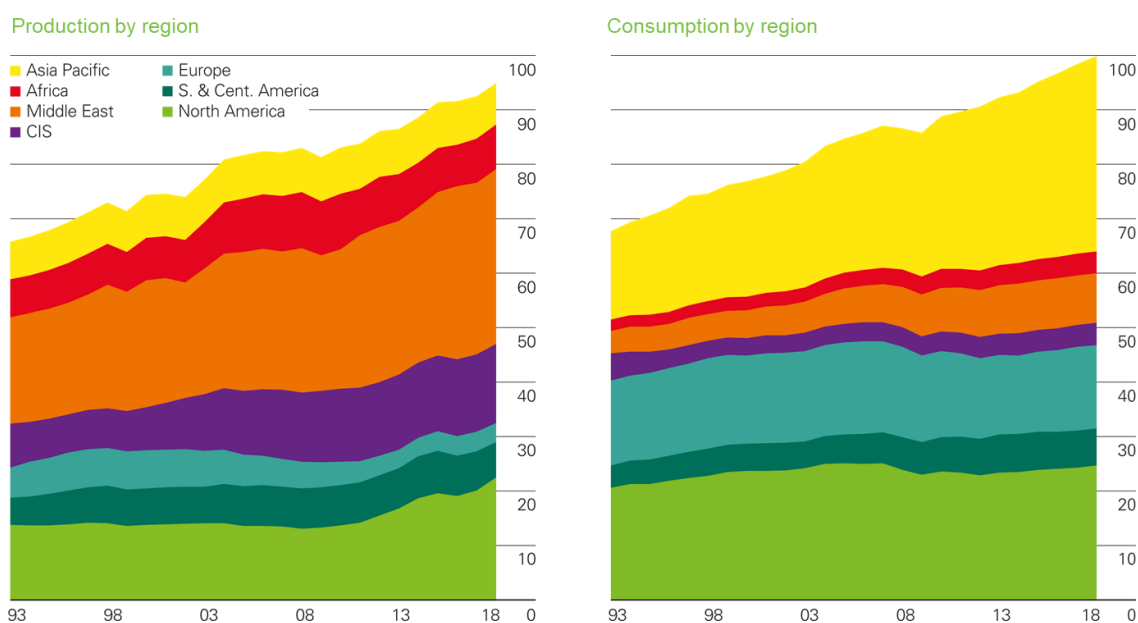


Figure 1.1 - Oil production and consumption by region (Million barrels daily)¹.

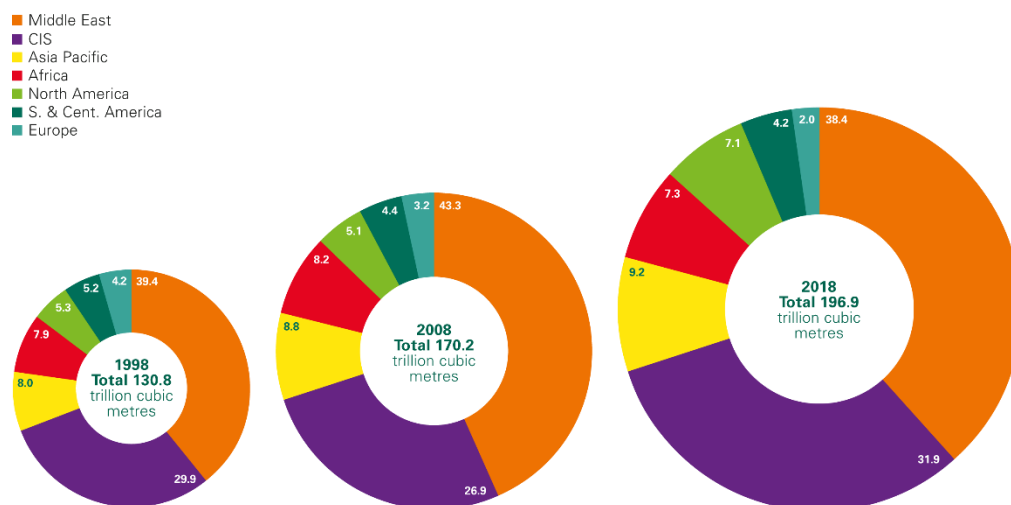


Figure 1.2 - Distribution of proved gas reserves: 1998, 2008 and 2018 (Percentage)¹.

However, the wide use and large consumption of fossil fuels like coal, crude oil, and natural gas which establish the pillars of modern industrials, as well as the main energy source for our daily electricity and transportation, brings large CO₂ emission, while they make modern life much more convenient comparing to that in the pre-industrial age. The combustion of fossil fuels contributes to the main anthropogenic CO₂ emission. As shown in Figure 1.3, global CO₂ emissions keep growing in the last seven decades², which accelerates global warming since CO₂ is green-house gas³. This is detrimental to the eco-system of the earth. As an evidence, the global mean surface temperature accordingly increases in the past years (Figure 1.4)⁴. To limit the global temperature rise within 1.5 °C in the next two or three decades, efficient measures have to be taken instantly. Since fossil fuels will still be the main energy source in the next decades, reducing emitted CO₂ is a more realistic direction against the urgent environmental issue.

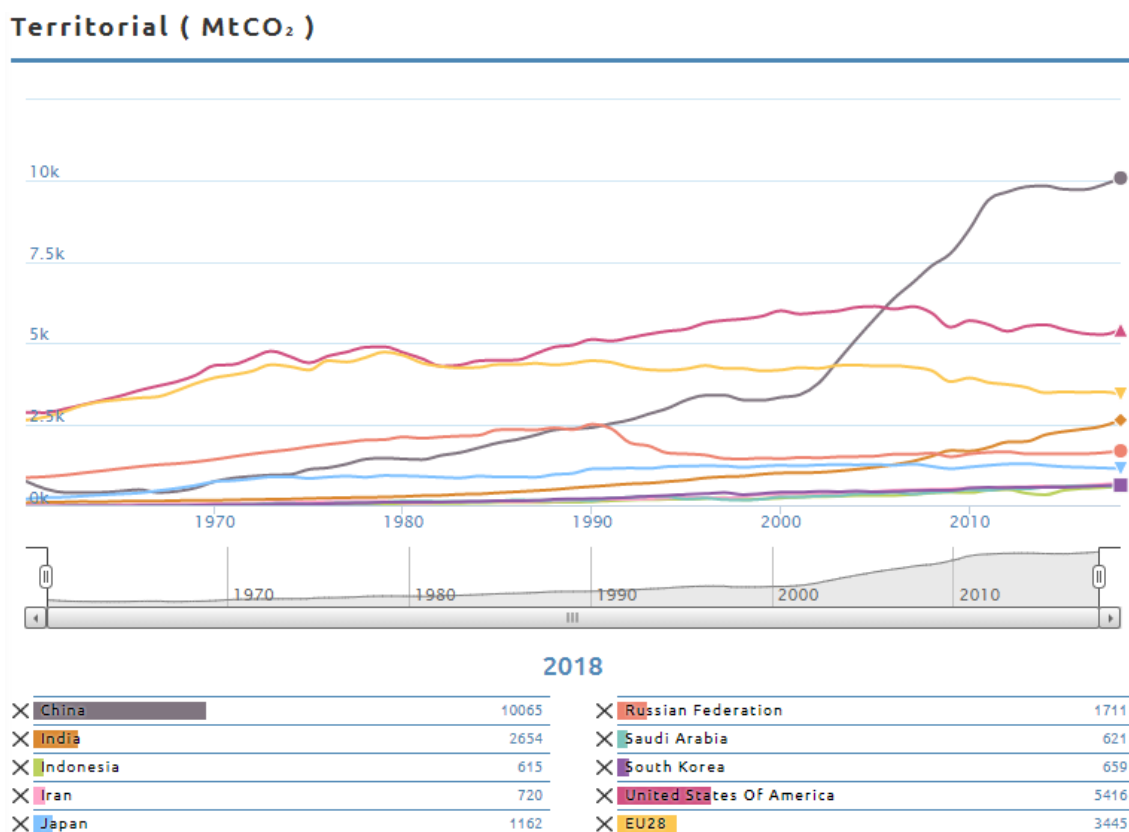


Figure 1.3 - Global territorial CO₂ emissions from 1960 to 2018². Sources: Gilfillan et al. (2019), UNFCCC (2019), BP (2019).

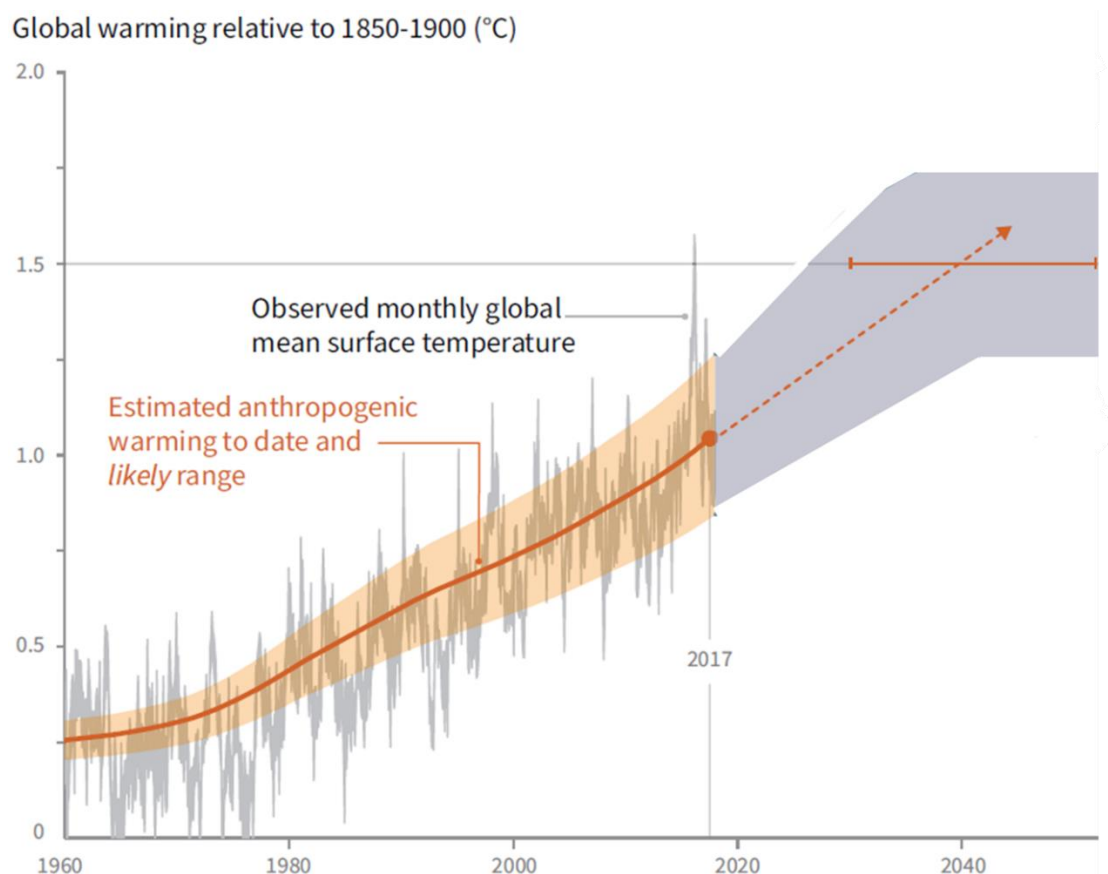


Figure 1.4 - Observed monthly global mean surface temperature (GMST, grey line up to 2017, from the HadCRUT4, GISTEMP, Cowtan–Way, and NOAA datasets) change and estimated anthropogenic global warming (solid orange line up to 2017, with orange shading indicating assessed likely range). Orange dashed arrow and horizontal orange error bar show respectively the central estimate and likely range of the time at which 1.5°C is reached if the current rate of warming continues⁴.

1.2 C1 chemistry: the solution to the dilemma

C1 chemistry is the chemistry of molecules containing only one carbon, mainly involving carbon dioxide, methane, carbon monoxide, methanol and similar other one-carbon compounds⁵. As illustrated in Figure 1.5, it is possible to produce lots of useful chemicals from the C1 chemistry building-blocks. Methane, carbon monoxide, carbon dioxide and methanol can play a role as the starting block, broadening modern chemical feedstocks from crude oil to coal, natural gas or biomass via reactions viz. dry/steam reforming of methane (DRM or SRM), oxidative coupling of methane (OCM), Fischer-Tropsch (FT), CO₂ hydrogenation and methanol to olefins (MTO)⁵⁻⁷. Hence, C1 chemistry, which makes use of one-carbon containing compounds is considered as the most promising strategy targeting both the environment, energy and resources issues related to petrol.

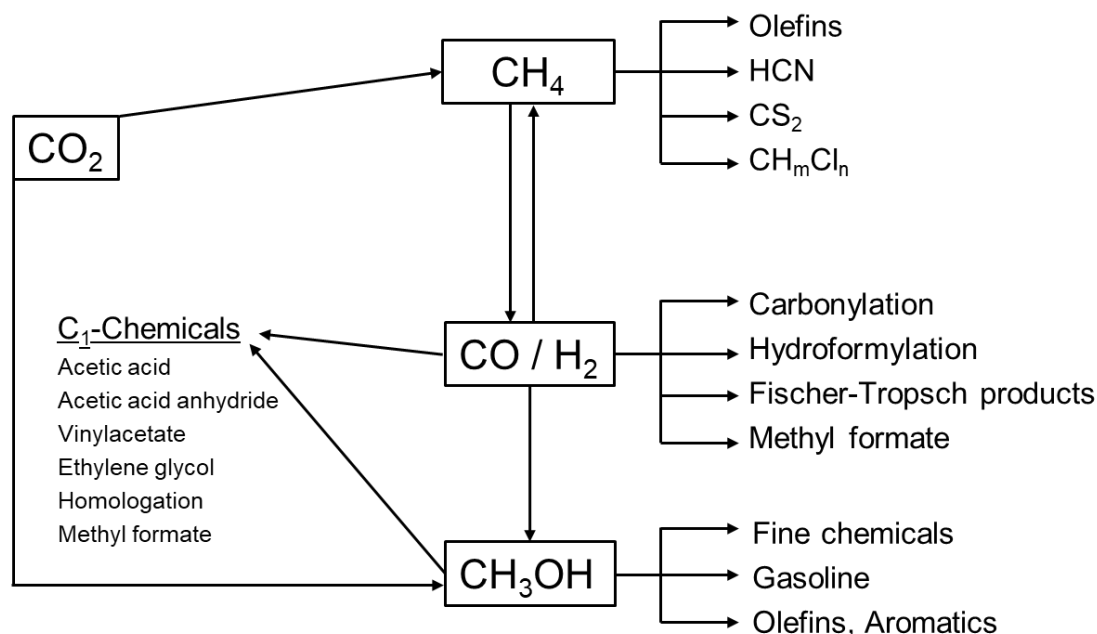


Figure 1.5 - C1 chemistry block reaction network⁵.

Among those reactions in C1 chemistry, OCM bridges CH₄ to the feedstocks for chemical industries, attracting intensive interest of researchers. CO₂ hydrogenation converts CO₂ to useful compounds, becoming a more positive means to lower down carbon emission comparing to simply capturing it and burying it underground⁸. Besides, the hydrogenation product, CH₄, CO or methanol, can start a new carbon cycle, making CO₂ hydrogenation a promising routine to close the carbon cycle. And dry reforming of methane (DRM) combines methane functionalization and carbon dioxide functionalization into one reaction. Therefore, OCM, CO₂ hydrogenation and DRM reactions occupy an important portion of C1 chemistry.

As well known, catalysis plays an indispensable role in C1 chemistry. Catalysts are normally applied in C1 chemistry reactions to maximize the conversion of reactant, the selectivity of targeted products and optimize reaction time needed to reach desired conversion and selectivity^{6, 7, 9}. Understanding how catalysis function in these reactions offer guidance to catalyst screening and reaction conditions optimization, expediting the development of C1 chemistry. Therefore, investigation of catalysis in OCM, CO₂ hydrogenation and DRM reactions has huge practical significance.

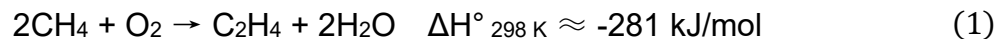
1.3 Oxidative coupling of methane

1.3.1 A brief historical evolution of OCM

Methane conversion to value-added products represents an attractive answer to the need for more sustainable and efficient processes for the production and storage of energy and chemicals. The large availability of natural gas reservoir, together with the environmental urgency of alternatives to crude oil, brought the attention of the chemical industry on these processes. In addition, natural gas resources are normally explored in remote regions. A huge demand for pipelines is required for transportation, which is economically unfavorable. Therefore, converting methane, the main component of natural gas, to more transportable forms with high energy density or higher chemical values on-site represents a more efficient alternative than the common burning of methane to generate heat or electricity. A lot of efforts have been done to achieve that since the last decades, for example, Andrussov or Degussa processes that directly convert methane and ammonia into hydrogen cyanide. On the other hand, methane steam reforming is the well-established technology to produce syngas as an intermediate, before converting into desired products such as long-chain hydrocarbon via FT synthesis. Among these approaches, steam reforming truly enables us to build a route from natural gas to a more transportable energy source and feedstock basis for chemical industrial. However, such an indirect route requires high energy, space, and facilities demanding. Therefore, the direct carbon chain expansion of methane is more promising.

Methane pyrolysis was firstly implemented in the 1970s to double the methane carbon chain by gas-phase homogeneous reaction¹⁰. Methane is chemically 'inert' due to its strong and stable C-H bonds (439 kJ/mol). The C-H bond cleavage is highly endothermic and requires a high temperature up to 1300 °C for methane pyrolysis, making the process energy-intensive. To milden the process conditions, Kellar and Bhasin brought up the new idea of OCM over heterogeneous catalysts in 1982, enabling methane coupling with an exothermic reaction¹¹. The global reaction is normally described as equation (1): methane and oxygen react to produce ethylene. Ethylene can be directly used as a feed in widely-mature industrial processes such as polyethylene production which is widely used for producing plastic commodities. In the last three decades, this 'dream reaction' has attracted great interest from researchers.

Although some works tried to use other oxidants such as N₂O and S₂, the non-toxic and cheap O₂ was found to be the most commonly used in OCM studies, which is more practical for commercializing the process.

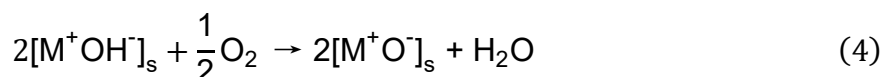
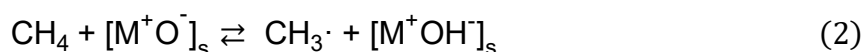


In 2015, Siluria Technologies built a pilot plant with the ambition to offer industrial application service for OCM reaction. However, large-scale commercialized industrial plant for OCM process is still not in production yet due to lower C₂ (ethane and ethylene) yield than the commercial target. In order to make the OCM reaction commercially viable and meet the economical goal, C₂ yield is of critical importance and has to be above 30%. Yet, it is very challenging for this reaction since the C₂ yield is limited by the nature of the OCM reaction mechanism which is described in the proceeding section.

1.3.2 OCM reaction mechanism

1.3.2.1 C₂H₆ formation

The generally accepted mechanism of OCM reaction involves radicals and proceeds through both heterogeneous (reactions on the catalyst surface) and homogeneous pathways (reactions in the gas phase). In general, CH₄ is firstly activated on catalyst surface generating methyl radicals (eq. 2), these methyl radicals are then released and coupled to form ethane in the gas phase (eq. 3). Finally, the active sites on catalyst surface are recovered by O₂ (eq. 4)¹²⁻¹⁴.



Theoretical studies and experimental proofs support such a heterogeneous-homogeneous reaction mechanism¹⁴⁻²². Methyl radicals have been witnessed directly or indirectly by various techniques, such as matrix isolation electron spin resonance (MIESR)¹⁶, lead mirror experiments¹⁷, multiphoton ionization time-of-flight mass spectrometry (MPI-TOFMS)²² and synchrotron vacuum ultraviolet photoionization

mass spectroscopy (SVUV-PIMS)^{18, 19}. Furthermore, regarding the next step, i.e. coupling of methyl radicals, Nelson and coworkers performed OCM reaction over Li/MgO at 750 °C using isotopes of methane (50/50% CH₄/CD₄)¹². As a result, C₂H₆, CD₃CH₃, and C₂D₆ were detected as ethane, whereas C₂H₄, CD₂CH₂, and C₂D₄ were detected as ethylene. The observed kinetic isotope effects clearly suggest that the coupling of methyl radicals takes place in the gas phase without the involvement of surfaces at this step.

1.3.2.2 C₂H₄ formation

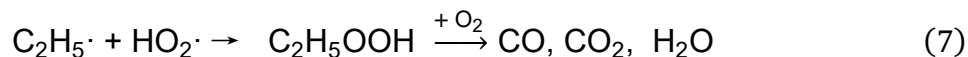
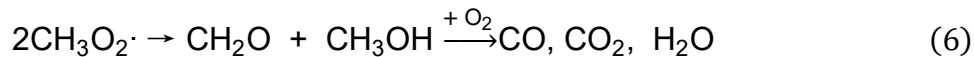
Ethylene is the most desired product of the 'dream' OCM reaction. Otsuka and coworkers confirmed that there is a negligible direct formation of C₂H₄ from CH₄^{23, 24}. Afterwards, Nelson and coworkers demonstrated that C₂H₆ is the main source of C₂H₄¹². Nowadays it is well accepted that C₂H₄ is formed via dehydrogenation of C₂H₆ under OCM reaction condition.

Ethane dehydrogenation can take place in two pathways: (i) direct thermal pyrolysis without oxygen and (ii) oxidative dehydrogenation of ethane (ODH). The former only takes place at high temperatures (>700 °C) with prominent coke formation²⁵. The latter ODH occurs in both homogeneous and heterogeneous pathways. Heracleous and Lemonidou studied oxidative dehydrogenation of C₂H₆ in the presence and absence of catalyst and found that the presence of O₂ accelerates overall reaction rates in the homogeneous reaction, whereas catalyst decreases the initial reaction temperature from 650 to 490 °C²⁶. Although the heterogeneous reaction pathway with catalyst leads to comparably lower C₂H₄ selectivity, the total C₂H₄ yield was enhanced due to higher C₂H₆ conversion.

1.3.2.3 CO_x formation

Hydrocarbon radicals can also react with oxygen, producing CO and CO₂ (CO_x, eq. 5-7). Recently, a study using SVUV-PIMS directly confirms methyl radicals in the gas phase during OCM and ODH reaction as well as another two radicals, C₂H₅· and CH₃OO·, and two reactive intermediates, CH₃OOH and C₂H₅OOH¹⁸. This provides convincing proofs of the elementary reaction steps related to targeted C₂ (C₂H₆ and C₂H₄), as previously mentioned. The unwanted CO_x formations involve radical

reactions, which proceed through both homogeneous pathways and heterogeneous pathways.



The homogeneous pathways of CO_x formation are expected to be more relevant at high temperatures and low dilution of reactants. Marquaire and coworkers²⁷ reported a relevant contribution from gas-phase oxidation reactions at 800 °C over La₂O₃. Methoxy and methylperoxy radicals together with formaldehyde have been proposed as intermediate for the homogeneous formation of CO_x species^{28, 29}.

Besides the gas-phase oxidation reactions, experimental evidence shows the existence of a heterogeneous mechanism for partial and total oxidation, i.e. a surface-mediated oxidation reactions^{30, 31}. A balance between homogeneous and heterogeneous reaction steps has to be considered in the consecutive oxidation of methyl radicals (Figure 1.6). Simple metal oxides as La₂O₃ and MgO are known to show good catalytic activity in OCM reaction and considerable activity in CO_x formation^{23, 32, 33}. The evaluation of the CO₂ formation over La₂O₃ at 750 °C (CH₄/O₂=2:1) upon switching between ¹⁶O₂ and ¹⁸O₂ showed distinct profiles for the concentrations of oxygen and carbon dioxide, proving the existence of surface-mediated oxidation rather than fast gas-phase oxidation³⁰. The direct involvement of lattice oxygen was also demonstrated in similar experiments over Sm₂O₃ and Li/MgO as catalyst³⁴. A proposed mechanism for catalytic (i.e. surface) total oxidation of methane involves the formation of methoxy species as the intermediate generated through the interaction between a methyl radical with surface oxygen³⁵. These adsorbed species undergo several oxidation steps with either lattice oxygen or gas-phase oxygen species, leading to the final CO_x products.

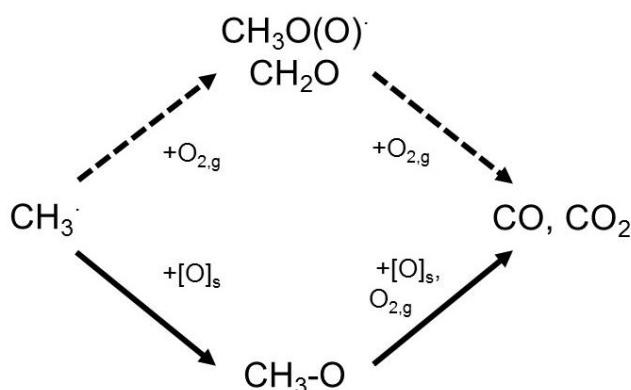


Figure 1.6 - Suggested pathways and intermediates in the partial and total oxidation of methyl radicals through gas-phase (dashed line) and heterogeneous (solid line) oxidation steps.

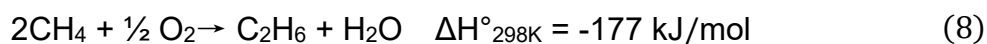
1.3.3 Challenges for OCM

1.3.3.1 Trade-off between CH₄ conversion and C₂ selectivity

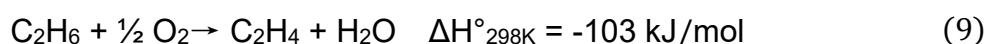
The uncertainty of radical reactions and the tightly correlated elementary reaction steps bring an intrinsic limit to the balance of C₂ selectivity and CH₄ conversion during OCM^{36, 37}. An upper bound of C₂ yield was predicted to be 28% under conventional, packed-bed and continuous-feed operation based on reported kinetic models and parameters³⁶.

As reported in the literature, over 160 elementary steps can be involved^{21, 38-41} in the OCM reaction system due to the complexity of radical reaction nature. For the sake of clear view of OCM reaction system, main (net) reactions and respective reaction enthalpies are listed below⁴².

Oxidative coupling of methane to ethane



Oxidative dehydrogenation of ethane



Total oxidation of methane, ethane and ethylene





Partial oxidation of methane



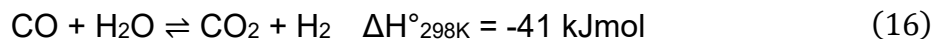
Steam reforming of methane



Dry reforming of methane



Water-gas shift



One obvious remark is that the net reaction can become exothermic despite the high energy required to break C-H bonds as noted above. On the other hand, although the steam and dry reforming reactions are highly endothermic, they can take place under OCM condition which normally means high temperature (above 600 °C).

Another remark is that both CH₄ reactant and targeted C₂ products are involved in side products (CO_x) formation. Partial and total oxidation of CH₄ are also highly exothermic as well as C₂ further oxidation. The stronger C-H bond in CH₄ (439 kJ/mol) comparing to that in C₂H₆ (423 kJ/mol)⁴³ results in more competitive C₂H₆ conversion reactions rather than CH₄ oxidative coupling. Lunsford and coworkers reported that the contribution of C₂ oxidation to the CO_x formation passed from 16% (700 °C) to 41% (800 °C) of the total CO_x over Sr/La₂O₃, and from 16% (700 °C) to 91% (850 °C) over Ba/MgO⁴⁴. At high methane conversions, CO₂ formation has been attributed mainly to total oxidation of ethylene via both reactions with the active oxygen on the catalyst and the interaction with a methyl radical in the gas-phase, forming acetylene as intermediate⁴⁵. These CO_x formation reactions are beneficial to CH₄ conversion but detrimental to C₂ selectivity. Without a catalyst, where OCM is a totally homogeneous reaction, C₂ selectivity during OCM decreases with increased CH₄ conversion, as the temperature increases (Figure 1.7)⁴⁶. The trade-off between CH₄ conversion and C₂

selectivity brings the challenge to lift up C₂ yield to the desired level for commercialization.

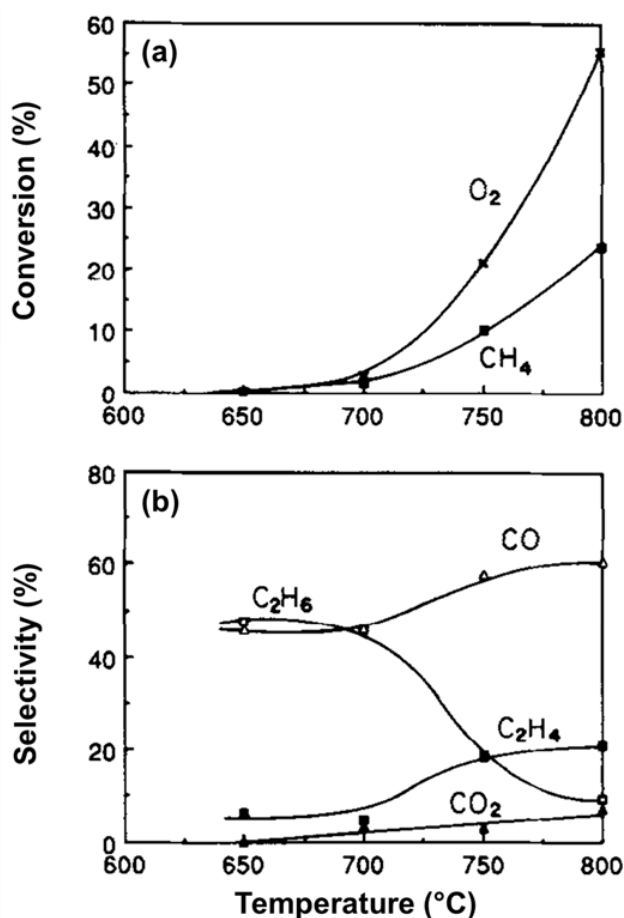


Figure 1.7 - Influence of temperature effects on methane and oxygen conversions and on product selectivity in an empty quartz reactor with a total feed flow rate of 50 cm³ min⁻¹, methane partial pressure of 0.66 atm, oxygen partial pressure of 0.23 atm: (a) ×, oxygen conversion; ■, methane conversion. (b) □, ethane selectivity; ■, ethylene selectivity; Δ, CO selectivity; ▲, CO₂ selectivity⁴⁶.

To overcome this trade-off and alter the reaction pathway toward a high-C₂-yield direction, the catalyst is applied for OCM reaction. During the past decades, a wide range of different catalysts and reaction conditions have been studied. According to statistical studies based on published reports, strongly basic oxides, mainly Mg and La oxides, tend to be good candidate catalysts for OCM reaction while alkali (Cs, Na) and alkaline earth (Sr, Ba) metal dopants have a positive effect on C₂ selectivity^{47, 48}. Even so, few reports show C₂ yield over 30% as shown in Figure 1.8^{48, 49}.

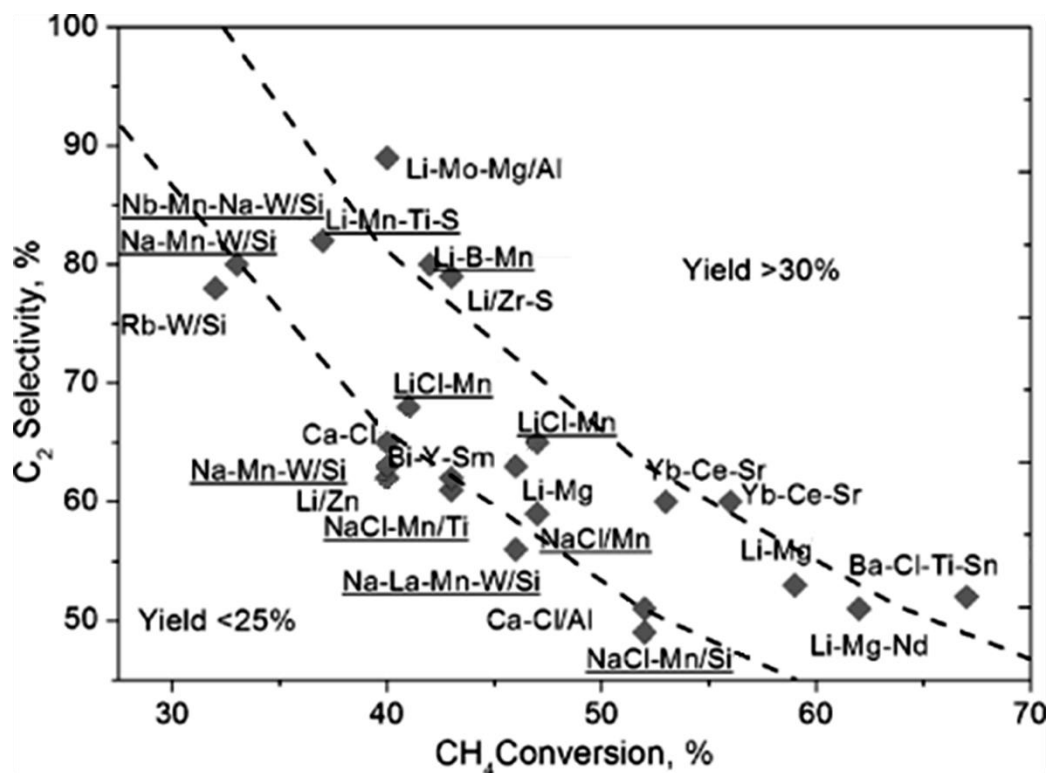


Figure 1.8 - Elemental compositions of OCM catalysts with a C₂ yield of >25% reported in the literature. All the catalysts were tested in a fixed-bed reactor in the co-feed mode under atmospheric pressure at temperatures from 670 to 950 °C, CH₄/O₂ = 1.7–9.0, and contact times of 0.2-5.5 s⁴⁸.

1.3.3.2 Interconnectedness of influencing factors for OCM

In the studies of OCM reaction, the CH₄/O₂ ratio, contact time, catalyst properties, and reaction temperature are the widely investigated influence factors.

From the discussion about the OCM reaction mechanism, we can learn that the abundant O-containing sites and gas-phase O₂ largely increase the chance of hydrocarbon radicals to collide with them under low CH₄/O₂ ratio condition, leading to total or partial oxidation reactions. Reversely, a higher CH₄/O₂ ratio enhances the collision of hydrocarbon radicals with each other, lifting up C₂ selectivity⁵⁰. However, too high CH₄/O₂ ratio also results in low coverage of active O species required for activating CH₄ and eventually leads to low CH₄ conversion⁵⁰. The effect of the CH₄/O₂ ratio inspired the concept of membrane reactors that allow dispersing O₂ all along the catalyst bed. In such a configuration, OCM reaction can be operated at a locally low O₂ concentration but with high total O₂ in the feed. Multiple O₂ dosing points along the

reactor is another answer to optimize the O₂ concentration along the bed. Up to now, the discussion seems to show that the effect of the CH₄/O₂ ratio on C₂ yield is a balance of CH₄ conversion and C₂ selectivity.

Another decisive property is the contact time that mainly affects the heterogeneous process. Since over-oxidation of hydrocarbons involves more heterogeneous steps, increasing contact time should lead to higher CO_x production, i.e. lower C₂ selectivity⁵¹. However, it also increases C₂ yield to some extent. The latter consequence is due to an increase of all reactions rates especially when the mass transfer rates are the limiting process^{52, 53}.

Catalyst properties also affect reaction orientations and the choice of particular catalysts can influence the distribution of the final products. For example, CeO₂ seems to favor over-oxidation of hydrocarbons than other catalysts⁵⁴. This can be explained by high CH₃• sticking coefficient of CeO₂ that represents a ratio of the number of CH₃• reacted on catalyst surface to the number of the collisions between CH₃• and the catalyst surface⁵⁴. Catalyst basicity has also been studied to correlate to inhibiting CO_x formation^{55, 56}, as well as surface area, although it is not clear if high surface area clearly promotes combustion reactions^{57, 58} or it plays a marginal role.

Temperature is another key factor influencing OCM reaction, which not only affects the CO_x direct sources and CO_x-formation reaction rates but also has a different level effect on OCM. High-temperature condition exhibits positive influence on C₂ selectivity⁵⁰. As shown in reactions (8) to (13), they all manifest a highly exothermic character. The heat released by these reactions can have a significant effect on the local temperature generating a huge temperature gradient within the catalyst bed as well as in the gas phase.

However, other possible side reactions such as steam and dry reforming of hydrocarbons, are endothermic. Although steam reforming of methane on typical OCM catalysts has not been detected at a temperature lower than 800 °C⁵⁹, the process cannot be neglected and evidence is found on different catalysts, including La₂O₃-CaO and CaO-CeO₂ at higher temperatures. Detailed experimental analysis was conducted by exposing the catalyst to a mixture of hydrocarbons and steam. Traces of steam reforming products were found at 850 °C, and they were probably formed by the consecutive reaction of C₂ products since a relevant conversion was found when

substituting methane with ethylene⁵⁹. For example, on CaO-CeO₂, the amount of H₂ produced by ethylene steam reforming at 850 °C was comparable to that produced in the OCM test at the same temperature⁶⁰. Obviously, this reaction is detrimental to the final C₂ yield, and in this sense, higher temperatures can lead to unfavorable path regarding OCM reaction.

Temperature also affects catalyst properties. Dominant active sites on the catalyst surface can vary from weakly bonded adsorbed oxygen to lattice oxygen for CH₄ combustion⁶¹. When lattice oxygen is the dominant active sites for CH₄ combustion, oxygen ion mobility in the catalyst bulk takes a role in influencing the reaction. For instance, La₂O₃ exhibited much higher oxygen ion mobility than Li/MgO³⁴, which is possibly one of the reasons that Li/MgO holds higher C₂ selectivity at high temperatures.

It is clear that temperature already has complex effects on reactions in the OCM system. CH₄/O₂ ratio, contact time and catalyst properties, which affect highly exothermic hydrocarbon combustion or partial oxidation reactions, certainly influence the temperature of the catalyst bed, which in return contributes to the adjustment of the distribution of the final products. This interconnectedness of different influence factors makes it very challenging to optimize the reaction conditions.

1.3.3.3 Spatial gradients present in the OCM system

Due to the exo- and/or endo-thermicity of reactions occurring in methane & oxygen co-feed OCM reactor, as well as complex gas composition (C₂H₆, C₂H₄, H₂O, CO₂, CO, and H₂) present simultaneously, the temperature gradient, gaseous concentration gradient, and available active sites gradient on the catalyst surface, can happen along the catalyst bed. Generally, OCM performance is evaluated by analyzing the gas composition at the reactor outlet, which is a common methodology in heterogeneous catalysis research. However, it is much less informative way especially for the reactions having various gradients in the reactor, and the OCM reactor is in such kind of condition. Thus, studying those gradients is vital for fair and clear OCM performance evaluation.

However, it is challenging to integrate available spatial analysis tools to the OCM reaction system attributed to the harsh reaction condition (generally above 600 °C),

resulting in limited reports containing spatial information during OCM. Among them, the Senkan group has done considerable contributions^{53, 62-64}. With the system they developed (as shown in Figure 1.9), both spatial gas concentration and temperature data can be obtained. Based on $\text{La}_2\text{O}_3\text{-CeO}_2$ nanofiber-based catalysts (Figure 1.10), the hotspot in front of the catalyst bed was confirmed. Temperature gradient within the catalyst varied with the change in reaction condition (CH_4/O_2 ratio, space velocity, and furnace temperature), and can go up to over 200 °C. Accordingly, products are mainly formed in front of the catalyst bed, indicating that effective catalyst bed is only a small part and reasonable catalyst amount diminution does no harm on catalytic performance. Besides, the position of CO_x peak is the same as the temperature peak position, which reasonably indicates the most exothermic nature of CO_x formation reactions in OCM system^{53, 63}. On the other hand, steam reforming reaction is witnessed for the first time after the intensive reaction zone via analyzing H_2O concentration evolution along catalyst bed⁶⁴. The Senkan group also reported interesting work implementing OCM in a dual-packed-bed reactor with split O_2 introduction at both the inlet and the inter-bed position, demonstrated a significant increase in C_2 yield and $\text{C}_2\text{H}_4/\text{C}_2\text{H}_6$ ratio with the same total amount O_2 feed, comparing to the experiment done with O_2 introduction at the inlet the alone. Strikingly, although it was not discussed in the report, second O_2 introduction promotes less C_2H_6 formation in the second catalyst bed than the first catalyst bed. On the other hand, C_2H_4 formation reaches similar extent in both catalyst beds, and CO_x formation exhibits the opposite trend of C_2H_6 formation⁶². This verifies that the formed products also play a role in influencing reaction directions. In addition, the Senken group also noticed significant levels of prompt H_2 formation at the front of the catalyst bed, but further discussion is absent⁶³.

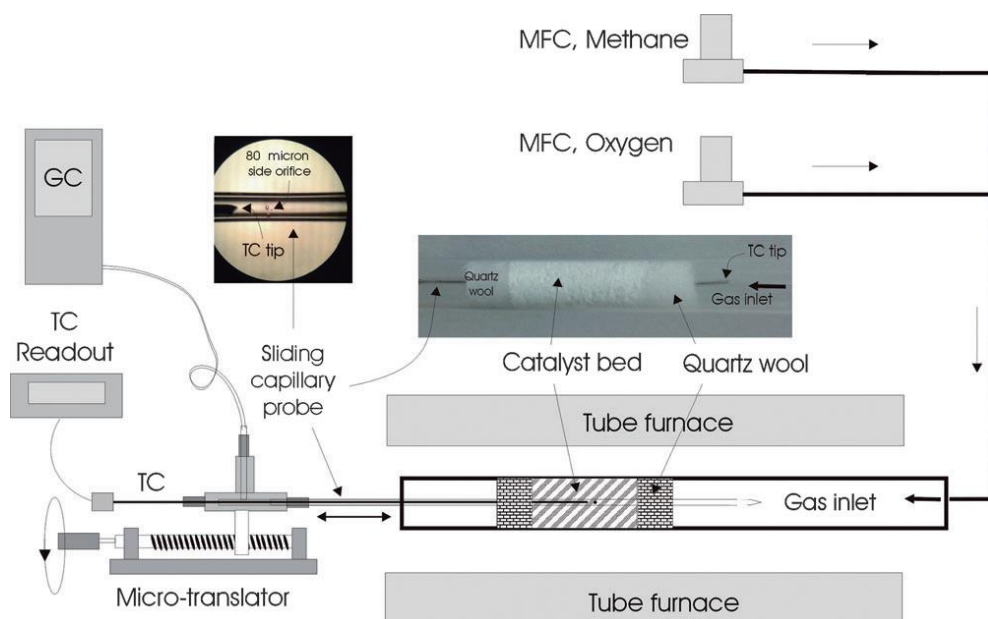


Figure 1.9 - The reactor system used by Senkan and coworkers to perform space-resolved gas sampling and temperature profiling along the axial direction⁶³.

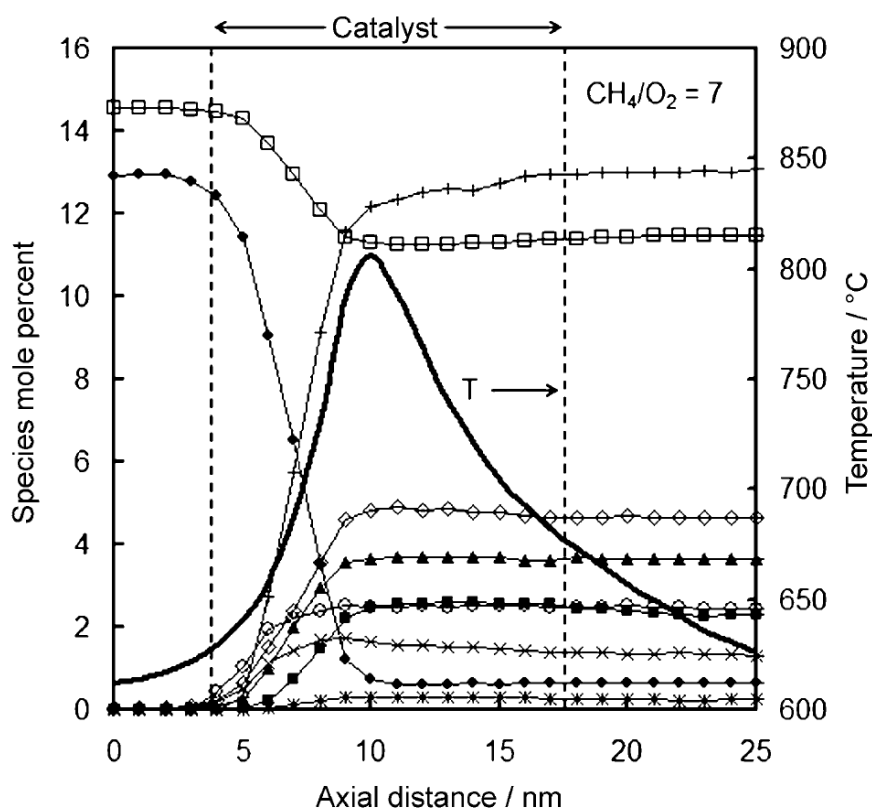


Figure 1.10 - Space-resolved profiles of catalyst ($\text{La}_2\text{O}_3\text{-CeO}_2$) temperature and gaseous species in the reactor under OCM condition at the feed CH_4/O_2 ratio of 4, furnace temperature of 600 °C. The following symbols are used: CH_4 (\square), O_2 (\blacklozenge), C_2H_6 (\blacktriangle), C_2H_4 (\blacksquare), C_3 ($*$), H_2O ($+$), H_2 (\circ), CO_2 (\blacklozenge), CO (\times), T (—)⁶³.

Apart from this group, Harold and coworkers also applied spatial analysis to OCM studying⁶⁵. In their work, only the spatial temperature profile was studied. The temperature rise was studied on different catalysts and associated with catalyst stability. As they claimed, although high temperature rise benefits C_2 yield, it deactivates the catalyst over time as indicated the shift of the temperature peak position toward the back of catalyst bed during the time-on-stream experiment (Figure 1.11)⁶⁵. It brings a new view of the temperature effect in the OCM system. With the operando X-ray diffraction computed tomography technique, Matras and coworkers were able to study La-Sr/CaO catalyst structure evolution during OCM reaction. Temperature and partial pressure of CO_2 are found to be related to the structure change. High temperature causes the catalyst sintering and CO_2 leads to inactive $SrCO_3$ phase formation⁶⁶.

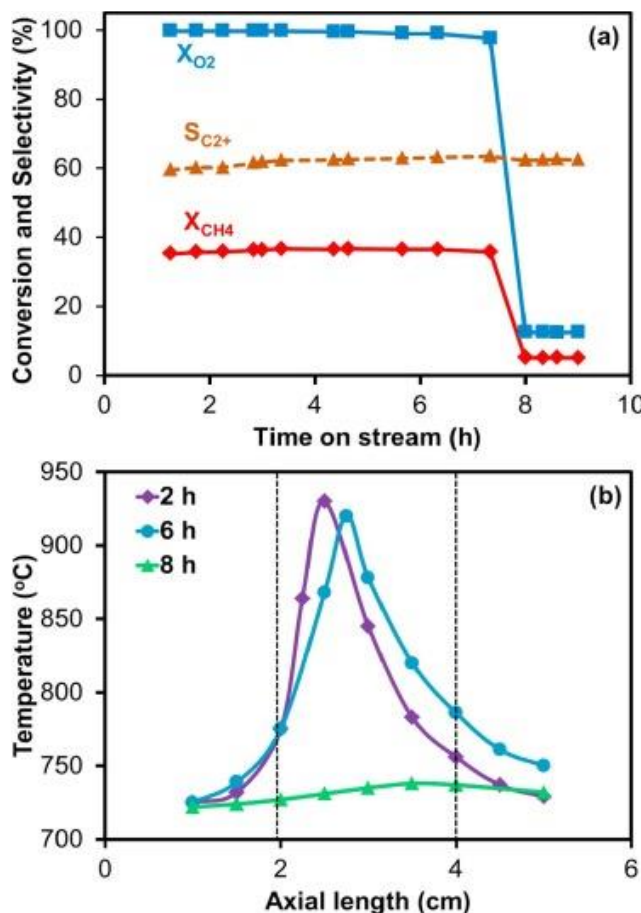


Figure 1.11 - (a) Dependence of conversion X_i (solid line), selectivity S_i (dashed line), and yield Y_i (dotted line) for species i as a function of TOS for Na_2WO_4 -Mn/SiO₂ catalyst ($T_f = 725$ °C; WHSV = 14,400 cm³/(h•g); CH₄:O₂:N₂ = 3:1:2.5). (b)

Variation in axial temperature profile with TOS. The length between the dotted lines represents the catalyst bed⁶⁵.

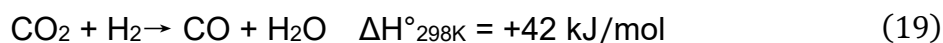
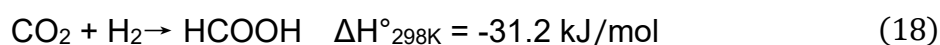
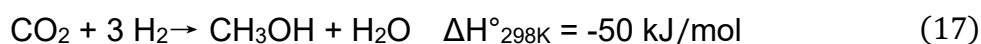
Obviously, OCM spatial analysis gives more informative details than traditional evaluation methods. As observed, intensive reactions happen only in the front of the catalyst bed and a huge temperature gradient can be achieved along that part of catalyst. This helps to understand the interconnectedness of the OCM system. However, current spatial analysis work is still not enough to unravel the detailed reaction pathways during OCM. More characterization techniques need to be involved in spatial analysis during OCM.

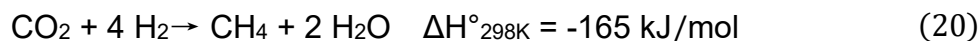
1.4 CO₂ hydrogenation reaction

1.4.1 Brief review of several CO₂ hydrogenation pathways

Among those strategies targeting the reduction of CO₂ emission, converting CO₂ into valuable chemicals can not only lower down CO₂ levels in the atmosphere but also change waste (CO₂) into wealth, which is more attractive comparing to simply capturing CO₂ and storing it underground. In nature, plants and some organisms are already doing this via photosynthesis – converting CO₂ into carbohydrate molecules – to close the carbon cycle. However, the self-recycling system of nature is not able to handle the growing anthropogenic CO₂ emission and artificial efforts are needed. CO₂ hydrogenation is one promising strategy, with the sustainable hydrogen source coming from photo- or electric- catalytic water splitting. Its hydrogenated products, CO, CH₄, CH₃OH or formic acid, can all be used as a building block in C1 chemistry, which enables the carbon recycled in unwanted CO₂ and close the carbon cycle at the end.

As well known, CO₂ is relatively chemically inert. Hydrogenation of CO₂ is a challenging process. Several reactions have been studied, such as CO₂ to methanol (equation 17), CO₂ to formic acid (equation 18), reverse water gas shift reaction (equation 19, RWGS), CO₂ methanation or Sabatier reaction (equation 20)⁶⁷⁻⁷⁰.





The first two reactions, methanol, and formic acid synthesis are suffering from the low CO₂ conversion at atmospheric pressure. Relatively harsh reaction conditions, i.e. high pressure, are required for higher CO₂ conversion and desired product selectivity. Reverse water gas shift reaction is endothermic and favourable at high temperature, resulting in high energy input demand. Among them, CO₂ methanation can be conducted under a mild condition with considerable CO₂ conversion and CH₄ selectivity. More importantly, the CH₄ product can use existing natural gas pipelines and infrastructures for transportation. In conclusion, CO₂ methanation is a feasible and attractive pathway for closing the carbon cycle.

1.4.2 CO₂ methanation development

CO₂ methanation already exists in nature in methanogens⁷¹. Nevertheless, biological CO₂ methanation exhibits slow kinetics and poor flexibility, making it unfavoured for industrial applications. Therefore, chemical CO₂ methanation, mainly heterogeneously catalysed CO₂ methanation reaction, has attracted much more attention⁷².

Heterogeneous catalytic CO₂ methanation reaction is mostly based on metal oxides supported metal catalysts and the active components in the catalysts are metals during CO₂ methanation reaction. Noble metals such as Rh, Ru, Pd, and Pt⁷³⁻⁸⁰, and different metal oxides, for example, Al₂O₃, TiO₂, SiO₂, MgO, MgAl₂O₄, CeO₂, and BaZrO₃, are comprehensively studied for this reaction^{75, 79, 81-84}.

Regarding the reaction mechanism, it is commonly agreed that the reaction occurs in the Langmuir-Hinshelwood pathway, namely CO₂ and H₂ are firstly adsorbed or dissociated on the catalyst surface and then react to form products. However, the active sites for CO₂ and H₂ adsorption and/or dissociation generate some disputes. Figure 1.12 illustrates two types of catalyst where metals are the only active components or both metal and metal oxide support are the active components^{79, 80}. Hyun et. al. and Simon et. al. studied the kinetics of CO₂ methanation on spatially separated Pt and Co nanoparticles and Co decorated Pt atoms supported on BaZrO₃ and Al₂O₃. From the catalytic activity and selectivity results, they suggested that Co is the active component for CO₂ activation, while Pt is active for H₂ dissociation^{79, 85}. On the other hand, over Pd/Al₂O₃ and Ru/CeO₂ catalysts, H₂ is dissociated on noble

metals while CO₂ is activated on metal oxides supports. The dissociated hydrogen spilled over to the interface of the metal and metal oxide support and then reacted with activated CO₂ forming the active intermediate, namely formate, then further hydrogenated to the final products^{78, 80}. These pieces of evidence are confirmed with the help of advanced characterization techniques such as *in situ* diffuse reflectance infrared Fourier Transform spectroscopy combined with mass spectrometric (DRIFTS-MS) or *operando* X-ray absorption near edge structure spectroscopy (XANES) and Raman spectroscopy. Besides, Ja Hun Kwat et. al found that when using inert multiwall carbon nanotubes (MWCNT) as support, no reaction takes place over Pd/MWCNT catalyst. However, by simply replacing MWCNT with Al₂O₃ or adding La₂O₃ into Pd/MWCNT, the catalyst becomes active for CO₂ hydrogenation, which verifies the metal oxide participation in CO₂ activation⁸⁶.

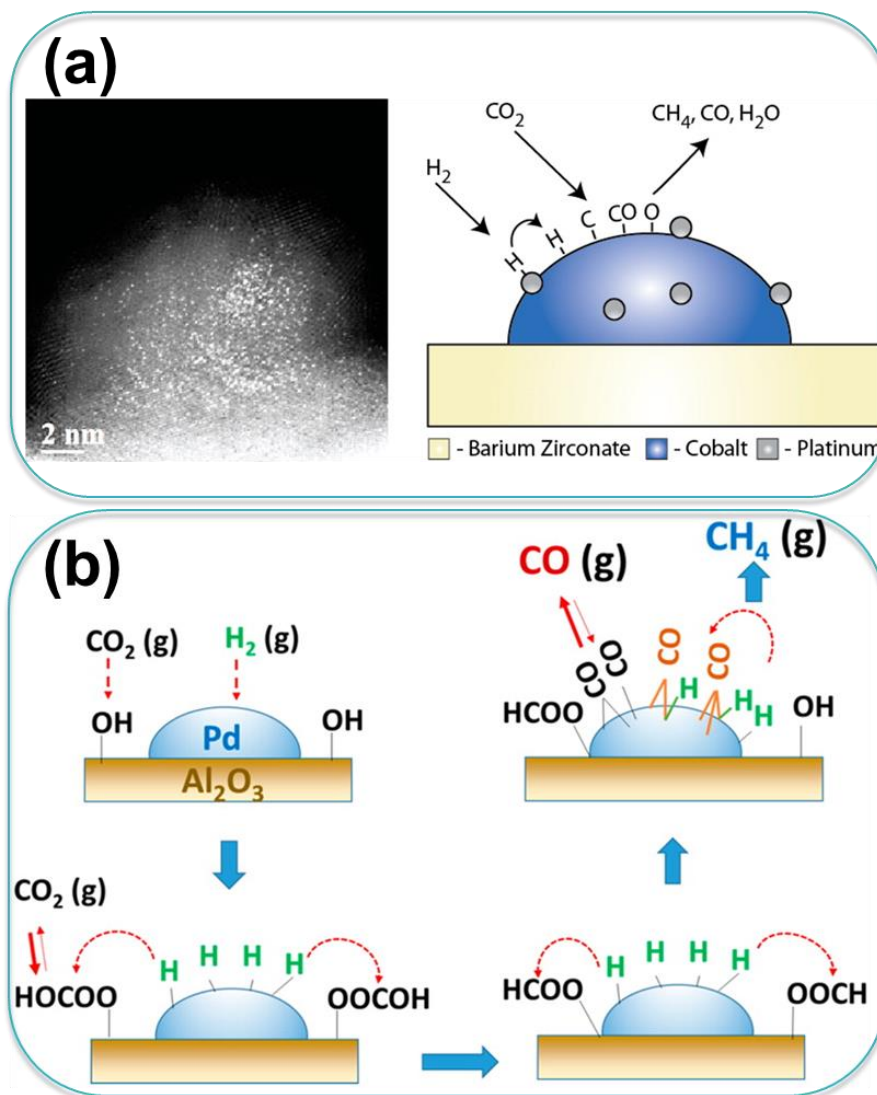


Figure 1.12 - Two different reaction mechanism types of CO₂ methanation based on Pt-Co/BaZrO₃ (a) and Pd/Al₂O₃ (b): (a) metals are the only active components⁷⁹; (b) metal and metal oxide support are both active components⁸⁰.

Another argument in the CO₂ methanation reaction mechanism is whether CO₂ is firstly reduced to CO following by CO methanation or proceeds directly via formate-intermediated species⁸⁷⁻⁸⁹. Although the agreement on this issue is not reached yet, it is clear that CO₂ activation in this reaction is important. To improve the activity of the catalysts, promoters such as alkali salts and alkaline earth are normally added. Such metal oxides are considered as active promoters for CO₂ hydrogenation due to their strong adsorption with CO₂^{90, 91}. Besides, industrial CO₂ emission sources normally contain various gases, adding gas purification costs for CO₂ conversion in the traditional co-feed mode. To mitigate this situation, a novel CO₂ capture and reduction

strategy was proposed to reduce high CO₂ source purification cost and applied to RWGS reaction⁹²⁻⁹⁴. As shown in Figure 1.13, operating under unsteady-state operation by switching between H₂ and CO₂ flow could provide an efficient CO₂ conversion process with CO₂-containing effluent directly, saving high CO₂ purification cost.. The catalysts suitable for this process are bifunctional catalysts such as FeCrCu/K/MgO–Al₂O₃ that could capture CO₂ from industrial effluent by strong adsorption on alkali and alkaline-earth metals (K and Mg), while captured CO₂ could be further reduced into desired products over active metal (Fe, Cr and Cu) in the next half-cycle⁹³. This concept is quite attractive for industrial implementation of CO₂ hydrogenation. Moreover, from the separation between CO₂ activation and reduction in this concept, we can learn that the catalyst must have efficient CO₂ capture ability, which is also applicable for the CO₂ methanation reaction as mentioned above. Therefore, it is promising and viable to apply the CO₂ capture and reduction concept to the CO₂ methanation reaction.

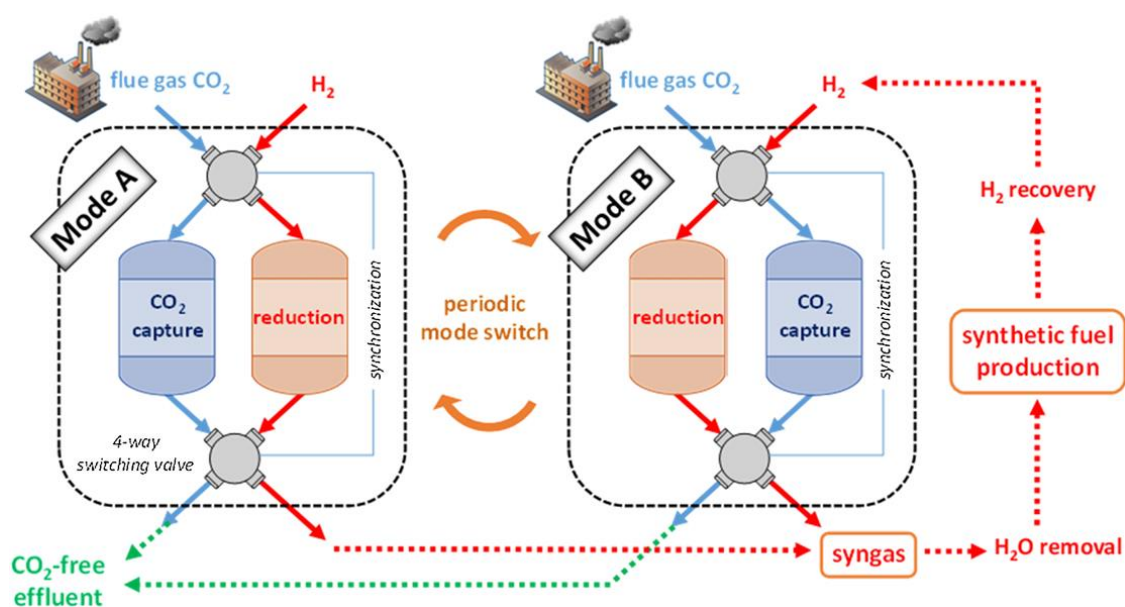


Figure 1.13 - Scheme of continuous capture and catalytic conversion of flue gas CO₂ to syngas in one process⁹³.

As mentioned in the beginning, noble metals are active and have been widely studied for CO₂ methanation. However, its high cost hinders the commercialization of CO₂ methanation. Targeting this issue, some transition metals such as Fe, Ni, Cu, and Co have gone into the vision of researchers and been investigated for the reaction⁹⁵⁻⁹⁶⁻⁹⁹. Among them, Ni is the most active one¹⁰⁰⁻¹⁰⁴.

In conclusion, adopting the new efficient strategy and exploring cheap but active catalysts are the potential directions coping with CO₂ methanation.

1.5 Dry reforming of methane

1.5.1 The advantage, the challenge, and the exploration

Dry reforming of methane (DRM), as shown in eq. 15., is the reaction converting CO₂ and CH₄ to CO and H₂. The products, known as syngas, are widely used as feedstock in the modern chemical industry as illustrated in Figure 1.5. The syngas is mostly provided by steam reforming of methane (SRM) industrially¹⁰⁵. Superior to SRM, DRM can not only make use of CH₄ but also mitigates CO₂ emission. Moreover, the produced syngas from DRM has a lower H₂/CO ratio (1:1) which is preferable for synthesizing heavy hydrocarbons in FT plants since excess of hydrogen suppresses carbon chain growth and leads to methanation reaction¹⁰⁶⁻¹⁰⁸. Meantime, DRM can make it easier to utilize some CH₄ and CO₂ co-containing gas sources such as natural gas, associated gas, unmineable coal seams, and biogas from biomass to avoid CO₂ sequestration process, as indicated in Figure 1.14¹⁰⁹.

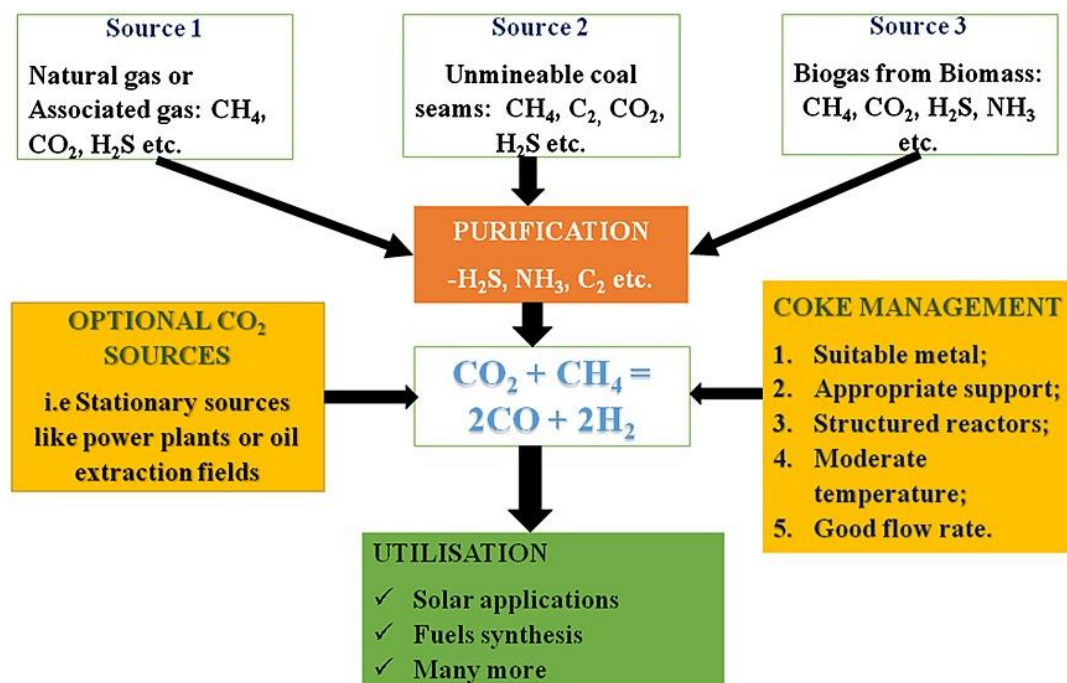
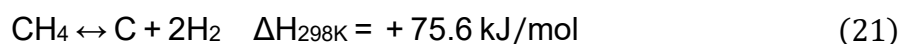


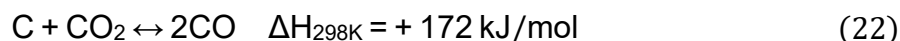
Figure 1.14 - The role of dry methane reforming in mitigating CO₂ and in the valorisation of methane, both from biogas and natural gas¹⁰⁹.

Following the initial concept of DRM brought up by Fischer and Tropsch in 1928¹¹⁰, DRM has attracted great attention and been deeply studied in terms of the reaction mechanism, catalyst design and reaction condition optimization etc.¹¹¹⁻¹¹⁴. DRM is generally considered to occur in two intermediate steps: methane decomposition (Eq. 21), CO₂ activation and reduction by the coke formed in methane decomposition (Eq. 22) which is also called carbon gasification or Boudouard reaction¹¹⁵.

Methane decomposition



Carbon Gasification



Similar to CO₂ hydrogenation, catalysts applied in DRM reaction are also mostly metal oxide supports supported noble metals (Pt, Rh, Ru, and Pd)¹¹⁶⁻¹²² or non-noble transition metals (Ni, Fe, and Co)¹²³⁻¹³². Among them, supported noble metals catalysts are active towards DRM and exhibit excellent coke resistance, which ensures the stability of the catalytic performance^{121, 133, 134}. On the other hand, non-noble transition metals, mainly nickel, gives excellent initial activity but suffer severe deactivation during the long-term experiment^{109, 135, 136}. From the economic perspective, bimetallic catalysts combining low-cost metal and noble metal are able to balance the activity and stability while using less noble metal, which turns out to be promising¹³⁷⁻¹⁴¹. Furthermore, coke resistance of the bimetallic catalysts with two low-cost metals also get improved comparing to supported monometallic catalysts^{124, 128-130}.

Although we have gained massive knowledge about DRM, the reaction alone is not ready for industrial application. So far, DRM has to be combined with SRM in order to be conducted on an industrial scale, which required huge amount of water steam^{105, 142}. The main obstacle for DRM commercialization at the moment is the rapid deactivation of the catalysts; there is no commercial catalyst able to maintain the high catalytic activity in a long-term operation period. The deactivation of the catalyst mainly arises from coke formation and active metal particles sintering. According to the thermodynamic study as shown in Figure 1.15, the equilibrium conversion of CO₂ is always lower than that of CH₄ in studied temperature range. This indicates that the coke formed via CH₄ decomposition could not be totally removed by CO₂

simultaneously, resulting in its accumulation. The coke formation during the reaction will eventually block the active sites and deactivate the catalyst. In order to get the equilibrium conversion of CH₄ and CO₂ over 80% and considerable syngas yield, high temperature (~800 °C) has to be applied for DRM^{143, 144}. At such high temperature, CH₄ decomposition occurs rapidly which leads to strong whisker-type coke formation and it contributes to nickel particles sintering^{145, 146}.

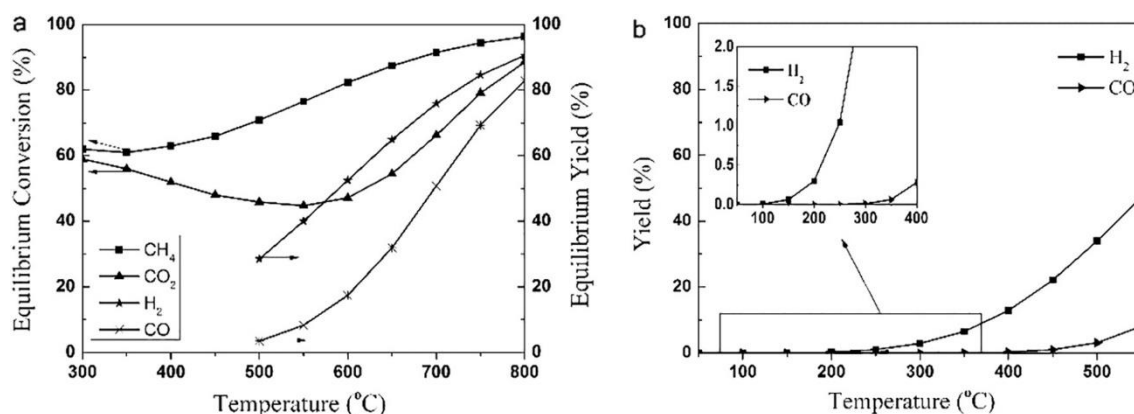


Figure 1.15 - The detailed theoretical thermodynamics calculation of the DRM reaction. Condition: $F(\text{CH}_4) = F(\text{CO}_2)$; $p = 1 \text{ atm}$ ^{143, 144}.

Many efforts have been devoted to avoid the fatal coke formation and active metal sintering. As discussed in the catalyst part, bimetallic catalysts are one of the options. Apart from that, the core-shell type of catalysts are also reported to be coke-resistant¹⁴⁷. For example, a type of Ni@SiO₂ core-shell catalyst was tested at 850 °C for 40 hours under the DRM reaction condition and negligible coke was detected¹⁴⁸. SiO₂-CeO₂ sandwiched Ni core-shell catalysts¹⁴⁹, multi-Ni-core@Ni phyllosilicate@CeO₂ shell hollow spheres¹⁵⁰ and bimetallic core@SiO₂¹⁵¹ have been synthesized and proven to prevent coke formation during DRM at high temperature. Adding promoters such as La, Ce, and Pr also improves the stability of the catalyst¹⁵²⁻¹⁵⁴. By stabilizing nanoparticles of the active metals via core-shell structure, the synergic effect or enhanced metal-support interaction could also be achieved and the rational design of such is the most intensively studied direction targeting the coke issues^{112, 114, 123, 155}. Apart from that, other attempts focusing on the reaction condition such as increasing CO₂/CH₄ ratios and lowering the reaction temperatures have also been conducted^{144, 156}. Nevertheless, more efforts or creative ideas are needed for industrial application of DRM coming true.

1.5.2 A new path: Chemical looping dry reforming of methane

Inspired by the chemical looping of methane partial oxidation which separates the reactants (CH_4 and O_2) into two independent processes, some researchers came up with this new path for DRM. The same principles are applied in chemical looping of methane dry reforming (CLDR), since the active metal under DRM conditions undergoes a similar redox cycle during CH_4 and CO_2 conversion as occurring in partial oxidation of methane¹⁵⁷. As shown in Figure 1.16, there are two types of CLDR based on the redox cycle of the active metal in DRM: the left scheme aims at full usage of carbon suitable for CO_2 sequestration¹⁵⁸; while the right scheme makes use of both carbon and hydrogen in the feed giving exactly DRM as a global reaction¹⁵⁹. In both cases, the oxygen storage of catalysts is the important parameter on account of its direct influence on the redox cycle^{131, 159-161}. Therefore, excellent oxygen storage materials such as CeO_2 are commonly used as a support for Ni-, Co-, and Fe-based catalysts^{131, 159}. Fe_xO_y is not only reported as a good oxygen carrier but also advantageous for the formation of Ni-Fe alloy as active metal. By adjusting the ratio of Ni/Fe in the bimetallic catalysts, More et al. proves that Ni content is responsible for the reducibility of the catalyst that determines CH_4 decomposition rate, while Fe content is more related to the oxidizability that affects CO_2 conversion rate¹⁶¹. On the other hand, CO_2 formation during CH_4 conversion procedure in the second type of CLDR is difficult to avoid with the catalyst having strong oxidizability, reducing the syngas selectivity. This is the disadvantage or the challenge for the process.

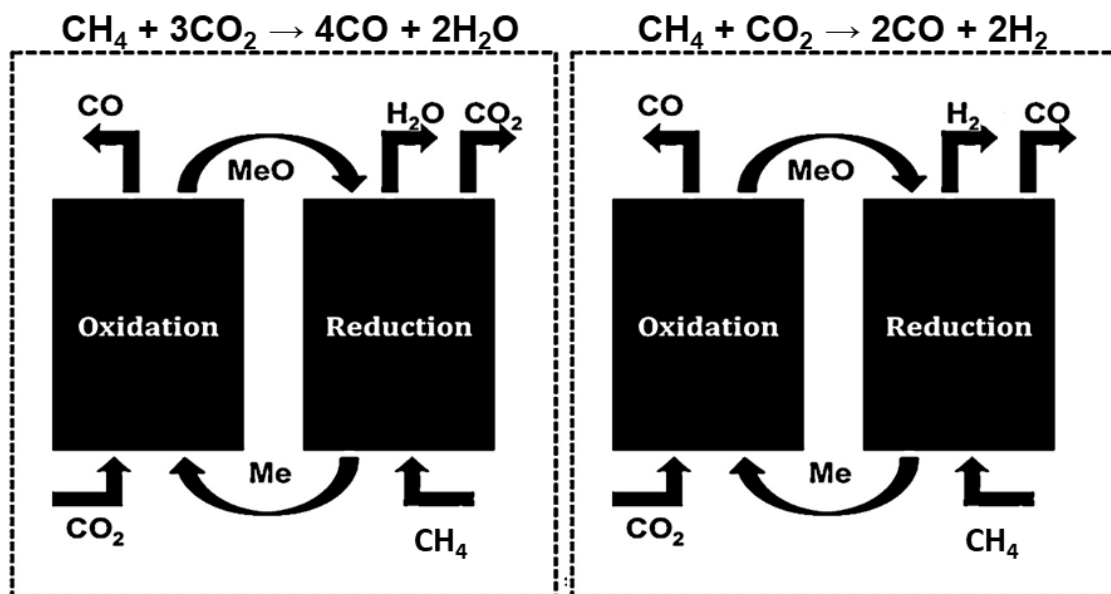


Figure 1.16 - Schematic for two types of CLDR based on the redox cycle of the active metal, shown with reduction of CO_2 to CO and full oxidation of methane^{159, 162}.

Apart from using the redox cycle of active metals, CLDR can be also performed in a similar way using CO_2 capture and reduction processes. For example, CaO supported Ni is used as the catalyst for the CO_2 hydrogenation (Figure 1.17)¹⁶³, where CO_2 is firstly captured by CaO forming CaCO_3 , then catalytically reduced by CH_4 over the adjacent Ni . Although this process is efficient for recycling CO_2 , it is currently performed in a non-isothermal manner, i.e. CO_2 capture and conversion processes are conducted under different temperatures. In order to take advantage of CO_2 looping on CaO , Buelens et al. developed a super-dry reforming of methane process for CO_2 utilization under isothermal condition. However, the major drawback of this process is not able to produce hydrogen.

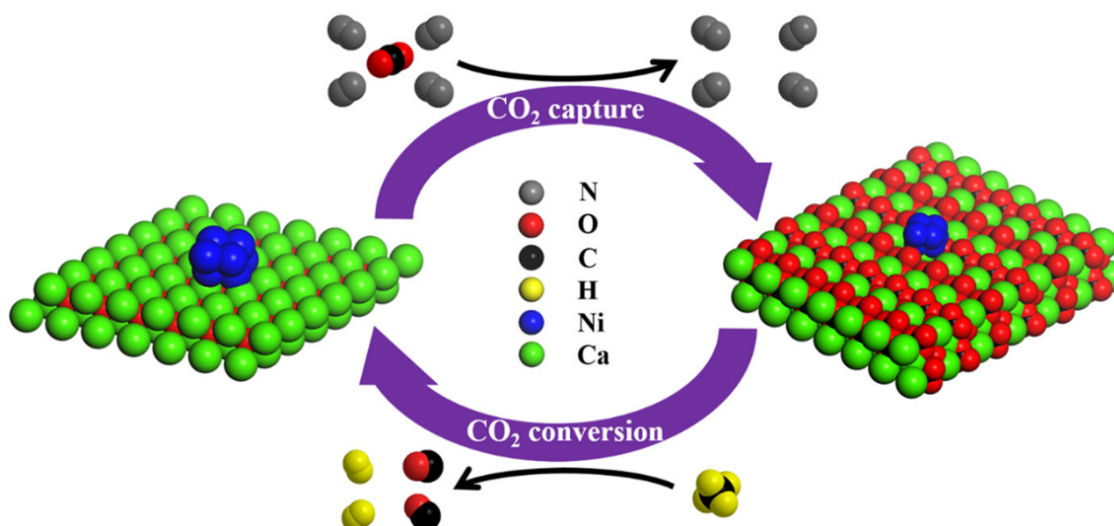


Figure 1.17 - Process schematic of catalytic CLDR in the CO₂ capture and conversion way based on CaO supported Ni catalyst.

From the DRM reaction mechanism, we have learned that the overall DRM reaction involves two intermediate reactions. Hereby, the concept of splitting these two intermediate reactions as a chemical looping process was proposed¹⁶⁴. In this type of CLDR, products are generated separately omitting further purification units on the occasions where pure hydrogen or pure CO is required. Currently, limited work has been reported on this topic and more effort is desired^{164, 165}.

1.6 Aim and overview of the thesis

The aim of the present thesis is to develop novel approaches for studying the catalysis and bring new possible solutions to CH₄ functionalization and CO₂ emissions mitigation in C1 chemistry. Herein, OCM, CO₂ methanation and DRM are the corresponding target reactions. Targeting the prominent spatial gaseous and thermal gradients along the catalyst bed and the complex radical-mediated reaction network during OCM with O₂ presence, operando spatial-resolved gas and temperature analysis techniques, high-temperature microscope, periodic operation and microwave reactor system were developed and applied for better understanding of OCM reaction mechanism. A novel CO₂ capture and reduction (CCR) strategy was explored in CO₂ methanation in order to make use of industrial CO₂ emission sources. To combine CO₂ and CH₄ functionalization, the chemical looping of DRM concept was implemented.

Chapter 2 describes methods, reaction systems, materials and reaction evaluation tools and techniques involved in the thesis. The emphasis is on the self-designed,

multiple-mode reaction system integrated with operando spatial analysis and visualisation tools, and its operation and corresponding data analysis methods.

Chapter 3 comprehensively shows the global and spatial OCM behaviour in the co-feed mode at different temperatures based on two simple metal oxides, La_2O_3 and MgO , as well as doping effect of alkali and alkali-earth metals (Li and Sr). By analysing the similar or different OCM performance, the contribution of spatial gradients to the catalytic performance evaluated at the outlet of the reactor and the preferable reaction pathways (heterogeneous or homogeneous) of the catalysts are discussed.

Chapter 4 further investigates the intrinsic activity of the two simple metal oxides to C_2 formation, CO formation and the coking behaviour with the aid of different modes of unsteady state operation and visualisation tools.

Chapter 5 shows some preliminary results of the application of microwave heating in OCM reaction based on the catalysts used in Chapter 3. This attempt evaluates the potential of microwave heating in radical-mediated catalytic reaction.

Chapter 6 deals with the application of CCR strategy in CO_2 methanation based on ZrO_2 supported Ni catalyst. The impact of the two promoters, K and La, are thoroughly investigated on the CO_2 capture capacity and reduction rate. Further unravelling of reaction mechanism is conducted with operando DRIFTS.

Chapter 7 presents the attempt of the chemical looping concept for DRM. Ni-based catalysts are applied in this reaction strategy. Several parameters such as supports, promoters and temperature are explored in terms of CO_2 conversion and CH_4 conversion in the two phases respectively.

Chapter 8 concludes the most remarkable results of the thesis and offers a brief outlook on the application of new techniques in C1 chemistry.

Bibliography

1. W. Keim, in *Pure Appl. Chem.*, 1986, vol. 58, p. 825.
2. J. Bao, G. Yang, Y. Yoneyama and N. Tsubaki, *ACS Catalysis*, 2019, **9**, 3026-3053.
3. W. Zhou, K. Cheng, J. Kang, C. Zhou, V. Subramanian, Q. Zhang and Y. Wang, *Chem Soc Rev*, 2019, **48**, 3193-3228.
4. J. H. Mercer, *Nature*, 1978, **271**, 321-325.
5. X. Xiaoding and J. A. Moulijn, *Energy & Fuels*, 1996, **10**, 305-325.
6. *bp statistical review of world energy*, BP Magazine, 2019.
7. J. Ma, N. Sun, X. Zhang, N. Zhao, F. Xiao, W. Wei and Y. Sun, *Catalysis Today*, 2009, **148**, 221-231.
8. C. J. Chen, M. H. Back and R. A. Back, *Can. J. Chem.*, 1975, **53**, 3580-3590.
9. G. E. Keller and M. M. Bhasin, *J. Catal.*, 1982, **73**, 9-19.
10. P. F. Nelson, C. A. Lukey and N. W. Cant, *J. Phys. Chem-us*, 1988, **92**, 6176-6179.
11. P. F. Nelson, C. A. Lukey and N. W. Cant, *J. Catal.*, 1989, **120**, 216-230.
12. K. D. Campbell, E. Morales and J. H. Lunsford, *J. Am. Chem. Soc.*, 1987, **109**, 7900-7901.
13. J. B. Kimble and J. H. Kolts, *Oxidative coupling of methane to higher hydrocarbons*, American Institute of Chemical Engineers, New York, NY; None, 1986.
14. D. J. Driscoll, W. Martir, J. X. Wang and J. H. Lunsford, *J. Am. Chem. Soc.*, 1985, **107**, 58-63.
15. C. A. Jones, J. J. Leonard and J. A. Sofranko, *J. Catal.*, 1987, **103**, 311-319.
16. L. Luo, R. You, Y. Liu, J. Yang, Y. Zhu, W. Wen, Y. Pan, F. Qi and W. Huang, *ACS Catalysis*, 2019, **9**, 2514-2520.
17. L. Luo, X. Tang, W. Wang, Y. Wang, S. Sun, F. Qi and W. Huang, *Sci Rep*, 2013, **3**, 1625.
18. Y. Tong, M. P. Rosynek and J. H. Lunsford, *J. Phys. Chem-us*, 1989, **93**, 2896-2898.
19. C.-H. Lin, J.-X. Wang and J. H. Lunsford, *J. Catal.*, 1988, **111**, 302-316.
20. E. E. Gulcicek, S. D. Colson and L. D. Pfefferle, *J. Phys. Chem-us*, 1990, **94**, 7069-7074.
21. K. Otsuka, K. Jinno and A. Morikawa, *J. Catal.*, 1986, **100**, 353-359.
22. S. Pak, P. Qiu and J. H. Lunsford, *J. Catal.*, 1998, **179**, 222-230.
23. R. Burch and E. M. Crabb, *Applied Catalysis A: General*, 1993, **97**, 49-65.
24. E. Heracleous and A. A. Lemonidou, *Applied Catalysis A: General*, 2004, **269**, 123-135.
25. M. Fleys, Y. Simon and P.-M. Marquaire, *Ind. Eng. Chem. Res.*, 2007, **46**, 1069-1078.
26. C. K. Westbrook and F. Dryer, *Chemical Kinetic Modeling of Hydrocarbon Combustion*, 1984.

27. J. C. Mackie, *Catalysis Reviews*, 1991, **33**, 169-240.
28. S. Lacombe, C. Geantet and C. Mirodatos, *Journal of Catalysis*, 1995, **151**, 439-452.
29. S. Lacombe, Z. Durjanova, L. Mleczko and C. Mirodatos, *Chemical Engineering & Technology*, 1995, **18**, 216-223.
30. P. Schwach, X. Pan and X. Bao, *Chemical Reviews*, 2017, **117**, 8497-8520.
31. S. J. Korf, J. A. Roos, J. M. Diphoorn, R. H. J. Veehof, J. G. van Ommen and J. R. H. Ross, *Catalysis Today*, 1989, **4**, 279-292.
32. K. P. Peil, G. Marcelin and J. G. Goodwin, in *Methane Conversion by Oxidative Processes: Fundamental and Engineering Aspects*, ed. E. E. Wolf, Springer Netherlands, Dordrecht, 1992, pp. 138-167.
33. G. A. Martin and C. Mirodatos, *Fuel Processing Technology*, 1995, **42**, 179-215.
34. Y. S. Su, J. Y. Ying and W. H. Green, *J. Catal.*, 2003, **218**, 321-333.
35. A. Kooh, J. L. Dubois, H. Mimoun and C. J. Cameron, *Catalysis Today*, 1990, **6**, 453-462.
36. J. W. M. H. Geerts, Q. Chen, J. M. N. van Kasteren and K. van der Wiele, *Catalysis Today*, 1990, **6**, 519-526.
37. H. Zanthoff and M. Baerns, *Industrial & Engineering Chemistry Research*, 1990, **29**, 2-10.
38. C. Karakaya, H. Zhu, C. Loebick, J. G. Weissman and R. J. Kee, *Catalysis Today*, 2018, **312**, 10-22.
39. J. Sun, J. W. Thybaut and G. B. Marin, *Catalysis Today*, 2008, **137**, 90-102.
40. R. Horn and R. Schlögl, *Catal. Lett.*, 2015, **145**, 23-39.
41. S. J. Blanksby and G. B. Ellison, *Acc. Chem. Res.*, 2003, **36**, 255-263.
42. C. Shi, M. P. Rosynek and J. H. Lunsford, *J. Phys. Chem-us*, 1994, **98**, 8371-8376.
43. J. A. Labinger, *Catalysis Letters*, 1988, **1**, 371-375.
44. G. S. Lane and E. E. Wolf, *J. Catal.*, 1988, **113**, 144-163.
45. E. V. Kondratenko, M. Schlüter, M. Baerns, D. Linke and M. Holena, *Catalysis Science & Technology*, 2015, **5**, 1668-1677.
46. U. Zavyalova, M. Holena, R. Schlögl and M. Baerns, *ChemCatChem*, 2011, **3**, 1935-1947.
47. S. Zarrinpashne, R. Ahmadi and S. M. Zekordi, Google Patents, 2011.
48. V. R. Choudhary, V. H. Rane and S. T. Chaudhari, *Applied Catalysis A: General*, 1997, **158**, 121-136.
49. C. T. Tye, A. R. Mohamed and S. Bhatia, *Chem. Eng. J.*, 2002, **87**, 49-59.
50. A. Nouralishahi, H. Pahlavanzadeh, M. Choolaei, E. Esmacili and A. Yadegari, *Korean J. Chem. Eng.*, 2013, **30**, 1213-1221.

51. D. Noon, B. Zohour and S. Senkan, *Journal of Natural Gas Science and Engineering*, 2014, **18**, 406-411.
52. Y. Tong and J. H. Lunsford, *J. Am. Chem. Soc.*, 1991, **113**, 4741-4746.
53. C. Chu, Y. Zhao, S. Li and Y. Sun, *Phys. Chem. Chem. Phys.*, 2016, **18**, 16509-16517.
54. L. Yu, W. Li, V. Ducarme, C. Mirodatos and G. A. Martin, *Applied Catalysis A: General*, 1998, **175**, 173-179.
55. Z. Gao and Y. Shi, *Journal of Natural Gas Chemistry*, 2010, **19**, 173-178.
56. V. I. Alexiadis, T. Serres, G. B. Marin, C. Mirodatos, J. W. Thybaut and Y. Schuurman, *AIChE Journal*, 2018, **64**, 2603-2611.
57. Z. Stansch, L. Mleczko and M. Baerns, *Industrial & Engineering Chemistry Research*, 1997, **36**, 2568-2579.
58. Z. Zhang and M. Baerns, *Applied Catalysis*, 1991, **75**, 299-310.
59. H. Arai, T. Yamada, K. Eguchi and T. Seiyama, *Applied Catalysis*, 1986, **26**, 265-276.
60. B. Zohour, D. Noon and S. Senkan, *ChemCatChem*, 2014, **6**, 2815-2820.
61. B. Zohour, D. Noon and S. Senkan, *ChemCatChem*, 2013, **5**, 2809-2812.
62. D. Noon, B. Zohour, A. Bae, A. Seubsai and S. Senkan, *RSC Advances*, 2017, **7**, 26783-26789.
63. A. Aseem, G. G. Jebe, M. T. Conato, J. D. Rimer and M. P. Harold, *Chem. Eng. J.*, 2018, **331**, 132-143.
64. D. Matras, S. D. M. Jacques, S. Poulston, N. Grosjean, C. Estruch Bosch, B. Rollins, J. Wright, M. Di Michiel, A. Vamvakeros, R. J. Cernik and A. M. Beale, *J. Phys. Chem. C*, 2019, **123**, 1751-1760.
65. <http://www.globalcarbonatlas.org/en/CO2-emissions>, 2018.
66. *Global Warming of 1.5°C. An IPCC Special Report on the impacts of global warming of 1.5°C above pre-industrial levels and related global greenhouse gas emission pathways, in the context of strengthening the global response to the threat of climate change, sustainable development, and efforts to eradicate poverty*, IPCC, 2018.
67. W. Wei and G. Jinlong, *Frontiers of Chemical Science and Engineering*, 2011, **5**, 2-10.
68. M. Schuessler, O. Lamla, T. Stefanovski, C. Klein and D. zur Megede, *Chemical Engineering & Technology*, 2001, **24**, 1141-1145.
69. Y. Shi, Y. Yang, Y.-W. Li and H. Jiao, *Applied Catalysis A: General*, 2016, **524**, 223-236.
70. W. Wang, S. Wang, X. Ma and J. Gong, *Chem Soc Rev*, 2011, **40**, 3703-3727.
71. R. K. Thauer, A.-K. Kaster, H. Seedorf, W. Buckel and R. Hedderich, *Nature Reviews Microbiology*, 2008, **6**, 579-591.

72. K. Ghaib, K. Nitz and F.-Z. Ben-Fares, *ChemBioEng Reviews*, 2016, **3**, 266-275.
73. M. Jacquemin, A. Beuls and P. Ruiz, *Catalysis Today*, 2010, **157**, 462-466.
74. A. Karelovic and P. Ruiz, *Appl. Catal. B-Environ*, 2012, **113-114**, 237-249.
75. F. Solymosi, I. Tombácz and J. Koszta, *J. Catal.*, 1985, **95**, 578-586.
76. S. Toemen, W. A. W. Abu Bakar and R. Ali, *Journal of CO2 Utilization*, 2016, **13**, 38-49.
77. G. Garbarino, D. Bellotti, E. Finocchio, L. Magistri and G. Busca, *Catalysis Today*, 2016, **277**, 21-28.
78. F. Wang, S. He, H. Chen, B. Wang, L. Zheng, M. Wei, D. G. Evans and X. Duan, *J. Am. Chem. Soc.*, 2016, **138**, 6298-6305.
79. H. H. Shin, L. Lu, Z. Yang, C. J. Kiely and S. McIntosh, *ACS Catalysis*, 2016, **6**, 2811-2818.
80. X. Wang, H. Shi, J. H. Kwak and J. Szanyi, *ACS Catalysis*, 2015, **5**, 6337-6349.
81. A. Karelovic and P. Ruiz, *J. Catal.*, 2013, **301**, 141-153.
82. C. Deleitenburg and A. Trovarelli, *J. Catal.*, 1995, **156**, 171-174.
83. T. Li, S. Wang, D.-n. Gao and S.-d. Wang, *Journal of Fuel Chemistry and Technology*, 2014, **42**, 1440-1446.
84. Z. Kowalczyk, K. Stolecki, W. Raróg-Pilecka, E. Miśkiewicz, E. Wilczkowska and Z. Karpiński, *Applied Catalysis A: General*, 2008, **342**, 35-39.
85. S. K. Beaumont, S. Alayoglu, C. Specht, N. Kruse and G. A. Somorjai, *Nano Lett.*, 2014, **14**, 4792-4796.
86. J. H. Kwak, L. Kovarik and J. Szanyi, *ACS Catalysis*, 2013, **3**, 2094-2100.
87. S. Eckle, H.-G. Anfang and R. J. Behm, *J. Phys. Chem. C*, 2011, **115**, 1361-1367.
88. C. Schild, A. Wokaun and A. Baiker, *J Mol. Catal.*, 1991, **69**, 347-357.
89. J. Szanyi and J. H. Kwak, *Phys. Chem. Chem. Phys.*, 2014, **16**, 15117-15125.
90. S. Hwang, U. G. Hong, J. Lee, J. H. Baik, D. J. Koh, H. Lim and I. K. Song, *Catal. Lett.*, 2012, **142**, 860-868.
91. A. Bansode, B. Tidona, P. R. von Rohr and A. Urakawa, *Catalysis Science & Technology*, 2013, **3**, 767-778.
92. Y. A. Daza, R. A. Kent, M. M. Yung and J. N. Kuhn, *Industrial & Engineering Chemistry Research*, 2014, **53**, 5828-5837.
93. L. F. Bobadilla, J. M. Riesco-García, G. Penelás-Pérez and A. Urakawa, *Journal of CO2 Utilization*, 2016, **14**, 106-111.
94. T. Hyakutake, W. van Beek and A. Urakawa, *J. Mater. Chem. A*, 2016, **4**, 6878-6885.
95. C. Liu, T. R. Cundari and A. K. Wilson, *J. Phys. Chem. C*, 2012, **116**, 5681-5688.
96. R. Razzaq, C. Li, M. Usman, K. Suzuki and S. Zhang, *Chem. Eng. J.*, 2015, **262**, 1090-1098.

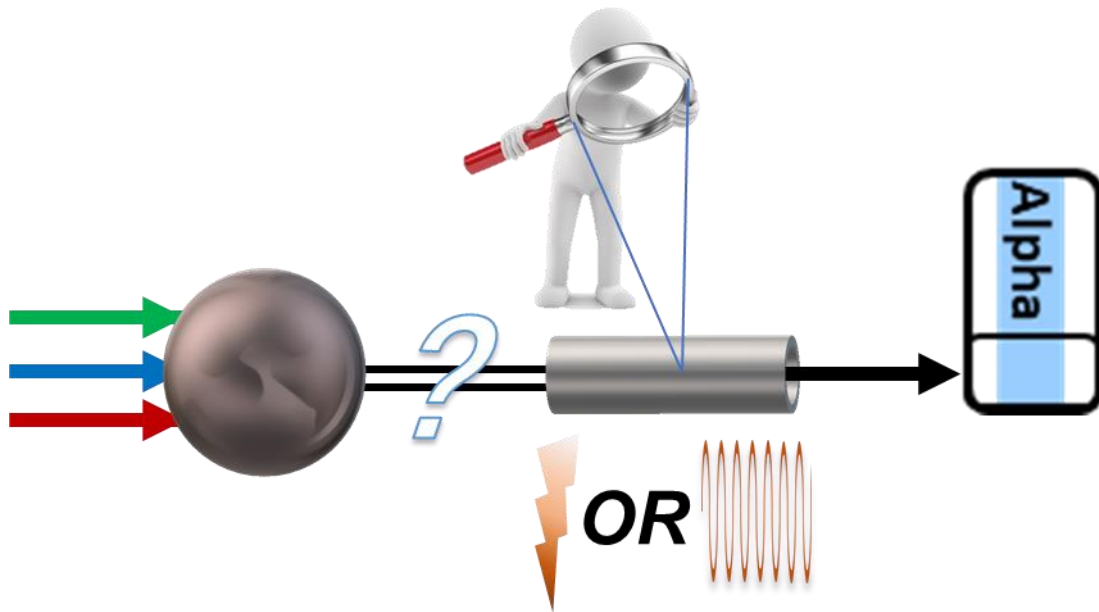
97. W. L. Vrijburg, E. Moioli, W. Chen, M. Zhang, B. J. P. Terlingen, B. Zijlstra, I. A. W. Filot, A. Züttel, E. A. Pidko and E. J. M. Hensen, *ACS Catalysis*, 2019, **9**, 7823-7839.
98. F. Solymosi, *J Mol. Catal.*, 1991, **65**, 337-358.
99. H. Lu, X. Yang, G. Gao, J. Wang, C. Han, X. Liang, C. Li, Y. Li, W. Zhang and X. Chen, *Fuel*, 2016, **183**, 335-344.
100. H. Muroyama, Y. Tsuda, T. Asakoshi, H. Masitah, T. Okanishi, T. Matsui and K. Eguchi, *J. Catal.*, 2016, **343**, 178-184.
101. R. Delmelle, R. B. Duarte, T. Franken, D. Burnat, L. Holzer, A. Borgschulte and A. Heel, *International Journal of Hydrogen Energy*, 2016, **41**, 20185-20191.
102. S. Danaci, L. Protasova, J. Lefevre, L. Bedel, R. Guilet and P. Marty, *Catalysis Today*, 2016, **273**, 234-243.
103. H. Song, J. Yang, J. Zhao and L. Chou, *Chinese Journal of Catalysis*, 2010, **31**, 21-23.
104. P. Frontera, A. Macario, M. Ferraro and P. Antonucci, *Catalysts*, 2017, **7**, 59.
105. P. Gangadharan, K. C. Kanchi and H. H. Lou, *Chem. Eng. Res. Des.*, 2012, **90**, 1956-1968.
106. M. Ding, Y. Yang, Y. Li, T. Wang, L. Ma and C. Wu, *Applied Energy*, 2013, **112**, 1241-1246.
107. I. C. Yates and C. N. Satterfield, *Energy & fuels*, 1992, **6**, 308-314.
108. A. A. Lemonidou and I. A. Vasalos, *Applied Catalysis A: General*, 2002, **228**, 227-235.
109. O. Muraza and A. Galadima, *International Journal of Energy Research*, 2015, **39**, 1196-1216.
110. F. Fisher and H. Tropsch, *Brennst.-Chem.*, 1928, **9**.
111. S. Wang, G. Q. Lu and G. J. Millar, *Energy & Fuels*, 1996, **10**, 896-904.
112. N. A. K. Aramouni, J. G. Touma, B. A. Tarboush, J. Zeaiter and M. N. Ahmad, *Renewable and Sustainable Energy Reviews*, 2018, **82**, 2570-2585.
113. M. Usman, W. M. A. Wan Daud and H. F. Abbas, *Renewable and Sustainable Energy Reviews*, 2015, **45**, 710-744.
114. X. Du, D. Zhang, R. Gao, L. Huang, L. Shi and J. Zhang, *Chem Commun (Camb)*, 2013, **49**, 6770-6772.
115. L. S. Gangurde, G. S. J. Sturm, M. J. Valero-Romero, R. Mallada, J. Santamaria, A. I. Stankiewicz and G. D. Stefanidis, *Chemical Engineering and Processing - Process Intensification*, 2018, **127**, 178-190.
116. M. Safariamin, L. H. Tidahy, E. Abi-Aad, S. Siffert and A. Aboukais, *Comptes Rendus Chimie*, 2009, **12**, 748-753.
117. Z. Hou, P. Chen, H. Fang, X. Zheng and T. Yashima, *International Journal of Hydrogen Energy*, 2006, **31**, 555-561.
118. C. Shi and P. Zhang, *Appl. Catal. B-Environ*, 2012, **115-116**, 190-200.

119. Ş. Özkara-Aydınoglu, E. Özensoy and A. E. Aksoylu, *International Journal of Hydrogen Energy*, 2009, **34**, 9711-9722.
120. I. Sarusi, K. Fodor, K. Baán, A. Oszkó, G. Pótári and A. Erdőhelyi, *Catalysis Today*, 2011, **171**, 132-139.
121. H. S. Whang, M. S. Choi, J. Lim, C. Kim, I. Heo, T.-S. Chang and H. Lee, *Catalysis Today*, 2017, **293-294**, 122-128.
122. C. Egawa, *J. Catal.*, 2018, **358**, 35-42.
123. X. Li, D. Li, H. Tian, L. Zeng, Z.-J. Zhao and J. Gong, *Appl. Catal. B-Environ*, 2017, **202**, 683-694.
124. Z. Bian and S. Kawi, *Journal of CO2 Utilization*, 2017, **18**, 345-352.
125. A. Kambolis, H. Matralis, A. Trovarelli and C. Papadopoulou, *Applied Catalysis A: General*, 2010, **377**, 16-26.
126. A. Djaidja, S. Libs, A. Kiennemann and A. Barama, *Catalysis Today*, 2006, **113**, 194-200.
127. S. Zhang, S. Muratsugu, N. Ishiguro and M. Tada, *ACS Catalysis*, 2013, **3**, 1855-1864.
128. H. Ay and D. Üner, *Appl. Catal. B-Environ*, 2015, **179**, 128-138.
129. S. M. de Lima and J. M. Assaf, *Catal. Lett.*, 2006, **108**, 63-70.
130. A. Tsoukalou, Q. Imtiaz, S. M. Kim, P. M. Abdala, S. Yoon and C. R. Müller, *J. Catal.*, 2016, **343**, 208-214.
131. J. Guerrero-Caballero, T. Kane, N. Haidar, L. Jalowiecki-Duhamel and A. Löfberg, *Catalysis Today*, 2019, **333**, 251-258.
132. M. C. J. Bradford and M. A. Vannice, *Applied Catalysis A: General*, 1996, **142**, 73-96.
133. M. Rezaei, S. M. Alavi, S. Sahebdehfar and Z.-F. Yan, *Journal of Natural Gas Chemistry*, 2006, **15**, 327-334.
134. D. Pakhare and J. Spivey, *Chem Soc Rev*, 2014, **43**, 7813-7837.
135. D. Chen, R. Lødeng, A. Anundskås, O. Olsvik and A. Holmen, *Chem. Eng. Sci.*, 2001, **56**, 1371-1379.
136. A. W. Budiman, S.-H. Song, T.-S. Chang, C.-H. Shin and M.-J. Choi, *Catalysis Surveys from Asia*, 2012, **16**, 183-197.
137. A. Á. M, L. F. Bobadilla, V. Garcilaso, M. A. Centeno and J. A. Odriozola, *Journal of CO2 Utilization*, 2018, **24**, 509-515.
138. C. Crisafulli, S. Scirè, S. Minicò and L. Solarino, *Applied Catalysis A: General*, 2002, **225**, 1-9.
139. B. Steinhauer, M. R. Kasireddy, J. Radnik and A. Martin, *Applied Catalysis A: General*, 2009, **366**, 333-341.
140. M. Ocsachoque, F. Pompeo and G. Gonzalez, *Catalysis Today*, 2011, **172**, 226-231.

141. C. Dai, S. Zhang, A. Zhang, C. Song, C. Shi and X. Guo, *J. Mater. Chem. A*, 2015, **3**, 16461-16468.
142. P. M. Mortensen and I. Dybkjær, *Applied Catalysis A: General*, 2015, **495**, 141-151.
143. M. K. Nikoo and N. A. S. Amin, *Fuel Process. Technol.*, 2011, **92**, 678-691.
144. Y. Wang, L. Yao, S. Wang, D. Mao and C. Hu, *Fuel Process. Technol.*, 2018, **169**, 199-206.
145. J. R. Rostrup-Nielsen, *Catalysis Today*, 1993, **18**, 305-324.
146. J. R. Rostrup-Nielsen, J. Sehested and J. K. Nørskov, in *Advances in Catalysis*, Academic Press, 2002, vol. 47, pp. 65-139.
147. K.-M. Kang, H.-W. Kim, I.-W. Shim and H.-Y. Kwak, *Fuel Process. Technol.*, 2011, **92**, 1236-1243.
148. J. Zhang and F. Li, *Appl. Catal. B-Environ*, 2015, **176-177**, 513-521.
149. S. Das, J. Ashok, Z. Bian, N. Dewangan, M. H. Wai, Y. Du, A. Borgna, K. Hidajat and S. Kawi, *Appl. Catal. B-Environ*, 2018, **230**, 220-236.
150. Z. Li and K. Sibudjing, *ChemCatChem*, 2018, **10**, 2994-3001.
151. T. Wu, W. Cai, P. Zhang, X. Song and L. Gao, *RSC Advances*, 2013, **3**, 23976-23979.
152. M. H. Amin, S. Putla, S. Bee Abd Hamid and S. K. Bhargava, *Applied Catalysis A: General*, 2015, **492**, 160-168.
153. Y. Sun, G. Zhang, J. Liu, Y. Xu and Y. Lv, *International Journal of Hydrogen Energy*, 2020, **45**, 640-649.
154. Y. Wang, J. Peng, C. Zhou, Z.-Y. Lim, C. Wu, S. Ye and W. G. Wang, *International Journal of Hydrogen Energy*, 2014, **39**, 778-787.
155. K. Mette, S. Kühn, A. Tarasov, M. G. Willinger, J. Kröhnert, S. Wrabetz, A. Trunschke, M. Scherzer, F. Girgsdies, H. Düdder, K. Kähler, K. F. Ortega, M. Muhler, R. Schlögl, M. Behrens and T. Lunkenbein, *ACS Catalysis*, 2016, **6**, 7238-7248.
156. A. M. Gaddalla and M. E. Sommer, *Chem. Eng. Sci.*, 1989, **44**, 2825-2829.
157. M. Tang, L. Xu and M. Fan, *Applied Energy*, 2015, **151**, 143-156.
158. T. Mattisson, A. Lyngfelt and P. Cho, *Fuel*, 2001, **80**, 1953-1962.
159. A. Löfberg, J. Guerrero-Caballero, T. Kane, A. Rubbens and L. Jalowiecki-Duhamel, *Appl. Catal. B-Environ*, 2017, **212**, 159-174.
160. S. Bhavsar and G. Veser, *Energy & Fuels*, 2013, **27**, 2073-2084.
161. A. More, S. Bhavsar and G. Veser, *Energy Technology*, 2016, **4**, 1147-1157.
162. M. Najera, R. Solunke, T. Gardner and G. Veser, *Chem. Eng. Res. Des.*, 2011, **89**, 1533-1543.
163. S. Tian, F. Yan, Z. Zhang and J. Jiang, *Science Advances*, 2019, **5**, eaav5077.

164. S. Assabumrungrat, S. Charoenseri, N. Laosiripojana, W. Kiatkittipong and P. Praserttham, *International Journal of Hydrogen Energy*, 2009, **34**, 6211-6220.
165. E. Promaros, S. Assabumrungrat, N. Laosiripojana, P. Praserttham, T. Tagawa and S. Goto, *Korean J. Chem. Eng.*, 2007, **24**, 44-50

2 MATERIALS AND METHODS



2.1 Catalysts synthesis

2.1.1 Impregnation method

Impregnation method consists of the immersion of the solid materials (supports or one active solid component) into the precursor solution containing active component¹⁻⁴. Because of capillary force, the solution can permeate inside the pores on the solid materials, ensuring a good dispersion of active phase on the solid surfaces¹. The method is easy to operate and commonly used in industrial catalysts synthesis.

Two different types of impregnation method can be recognized: wet impregnation which uses excess solution, and incipient wet impregnation in which the volume of precursor solution is equal to the total pore volume of the material to impregnate¹. The wet impregnation can achieve the uniform active phase dispersion, but the loading of the active phase is fixed, equals to the maximum loading of the solid material that can hold. The incipient wet impregnation is superior considering this, since it is feasible to control the active phase loading. Considering this, incipient wet impregnation method was adopted for the Ni-based catalyst synthesis in the thesis.

2.1.2 Mechanical milling method

Mechanical milling method is grinding the precursors with some medias such as balls and grinding rod to obtain desired material, and widely used in nanomaterial synthesis⁵. It is also easy to operate and to scale the synthesis up to tons of product. For brittle ingredients mixing, mechanical milling method is advantageous. The method was applied to OCM catalyst synthesis in the thesis.

2.2 Catalyst characterization tools

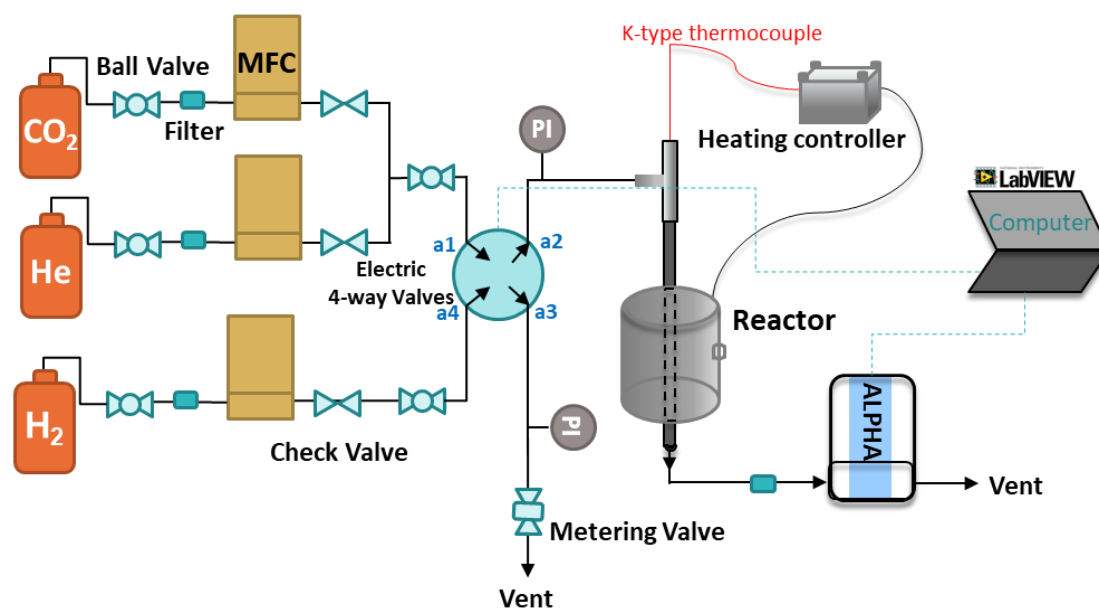
Power X-ray diffraction (PXRD) was performed on D8 Advanced Powder Diffractometer (Bruker) equipped with a vertical 2theta-theta goniometer in transmission configuration, with a $K\alpha_1$ germanium monochromator for Cu radiation ($\lambda=1.5406 \text{ \AA}$), at a scan step of $0.02^\circ \cdot \text{s}^{-1}$ from 10° to 80° .

Brunauer–Emmett–Teller (BET) surface area of catalysts was determined by N_2 physisorption using Autosorb iQ (Quantachrome Instruments).

H₂ temperature programmed reduction (H₂-TPR) and reductive CO₂ temperature programmed desorption in H₂ atmosphere were performed on TPDRO 1100 (Thermo Fisher Scientific) equipped with a TCD detector. Soda lime (CaO+Na₂O) trap was used to adsorb H₂O and CO₂.

2.3 Reaction systems and *operando* measurement setups

2.3.1 CO₂ capture and reduction (CCR) reaction system

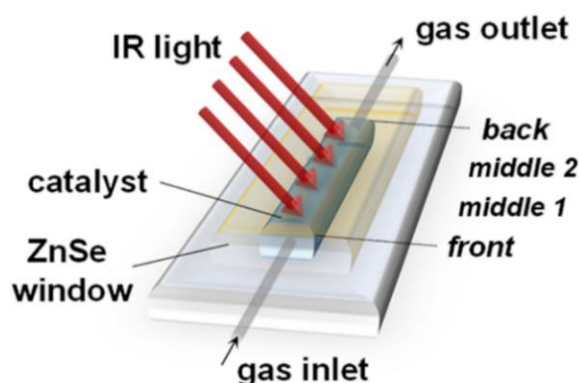


Scheme 2.1 - The overall scheme of CCR setup.

For CCR reaction, CO₂ was diluted in He and the dilution was controlled by two mass flow controllers (MFCs, Bronkhorst). Diluted CO₂ and pure H₂ were alternatively introduced into the reactor via an electric 4-way valve as shown in Scheme 2.1. The effluent after the reactor flew into the ALPHA infrared (IR) detector previously calibrated. The calibration procedure is described in Section 2.4.1. The reactor consisted of a 3/8' stainless steel tube placed in a furnace. To monitor the temperature, a K-type thermocouple was inserted in the quartz tube with the tip in contact with the catalyst bed. The thermocouple was connected to the heating controller. The electric 4-way valve and IR detector were controlled by the computer via a lab-designed LabVIEW program. The reaction operation is described in Section 2.4.3.

2.3.2 CCR Space- and time-resolved *operando* DRIFTS

Space- and time-resolved *operando* DRIFTS was performed using a reaction cell mimicking the action of a fixed-bed plug flow reactor, with a similar design to that reported previously, as shown in Scheme 2.2. The cell was mounted in a Praying Mantis (Harrick) optical accessory (Harrick) fixed in Vertex 70V FTIR spectrometer (Bruker). The composition of the effluent stream was analyzed by mass spectrometer (OmniStar, Pfeiffer Vacuum) and in the gas cell of the ALPHA IR spectrometer (Bruker) in a synchronized manner with the DRIFTS measurements.

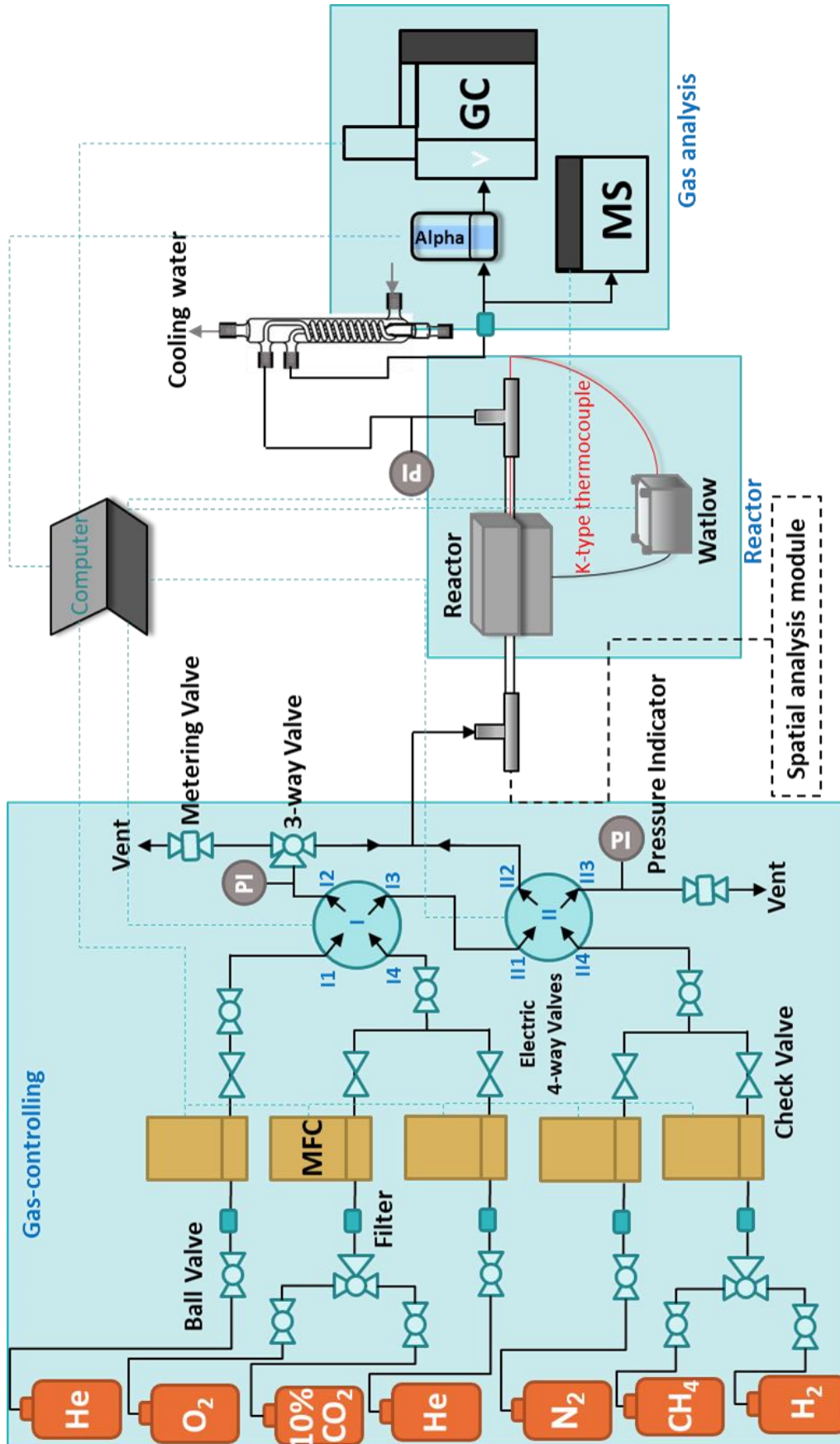


Scheme 2.2 - Space- and time-resolved *operando* DRIFTS.

2.3.3 Oxidative coupling of methane (OCM) and dry reforming of methane (DRM) reaction system

The reaction setup consists of a gas-controlling system, a reactor zone and the on-line gas analysis part as shown in Scheme 2.3 and Figure 2.1. The gas controlling system includes MFCs (Bronkhorst, 0 – 150 bar, 0 – 120 mL/min, the range is calibrated with Helium) and electric-actuated 4-way valves. Different gases (O_2 , He, N_2 and CH_4) firstly flow into the inlets (I1, I4, II1, II4) of the two electric 4-way valves with the flow rate controlled by MFCs. By changing the position (A, B) of the electric 4-way valves, two different inlet-outlet pairs for each valve are achieved, resulting in different gases flowing into the reactor (as shown in Table 2.1). For conducting unsteady-state operation, the 3-way valve after switching valve I is selected to the vent. For steady-state operation, the same 3-way valve is selected to the reactor and the 4-way valves are set at position I-B and II-B. The pressure indicator and metering valve allows monitoring and keeping the pressure of the vent and reactor lines well balanced, in

order to avoid the flow fluctuation in the reactor gas line. A flowmeter is used to calibrate the MFCs with the proper gas before reaction.



Scheme 2.3 - Overall scheme of OCM and DRM reaction system.



Figure 2.1 - Real picture of OCM reaction system.

Table 2.1 - 4-way valve positions and corresponding gas flowing into the reactor

Valve position		Port connection	Gas to reactor
Valve I	Valve II		
A	A	I1 → I2; I4 → I3 II1 → II2; II4 → II3	O ₂ /CO ₂
A	B	I1 → I2; I4 → I3 II1 → II3; II4 → II2	CH ₄ /H ₂
B	A	I1 → I3; I4 → I2 II1 → II2; II4 → II3	Pure He
B	B	I1 → I3; I4 → I2 II1 → II3; II4 → II2	CH ₄ /H ₂

The reactor consists of a lab-designed furnace and a quartz tube (OD: 6 mm, ID: 4 mm). In the furnace, the resistance heating alloy line is densely half coiled on a quartz tube, which contains a steel tube inside to distribute heat homogeneously on the

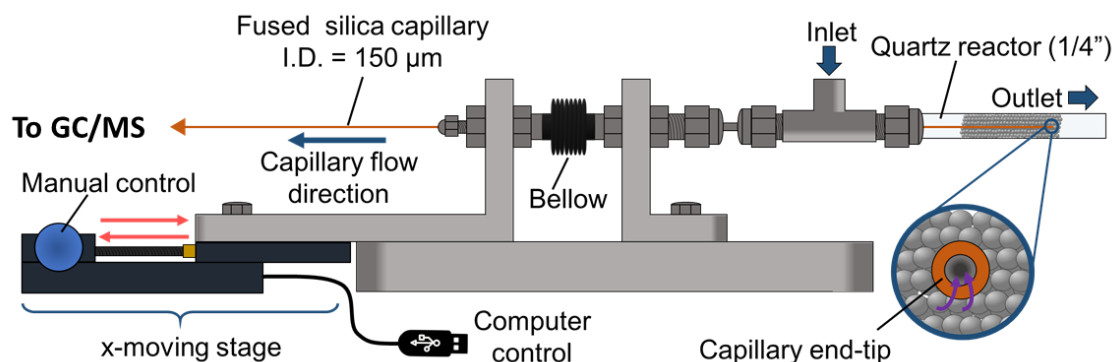
catalyst bed charged in the reactor quartz tube (shown in Figure 2.3). The resistance heating alloy line is connected to a proportional–integral–derivative controller (PID) heating controller (Watlow) with a K-type thermocouple inserted into the quartz reactor tube and its sensitive tip placed at the end of the catalyst bed. At the reactor outlet, a water condenser is used to remove H₂O produced during OCM reaction which is deleterious for the analytic instruments.

The on-line gas analysis part includes several analytic instruments: an ALPHA Fourier-transform infrared spectrometer (ALPHA, Bruker), a mass spectrometer (MS, OmniStar, Pfeiffer Vacuum) and a gas chromatography (GC, Agilent 7890B) with one thermal conductivity detector (TCD) and two flame ionization detectors (FID). Before doing the quantitative analysis, ALPHA and GC are calibrated with calibration mixtures. ALPHA calibration procedure is described in section 2.4.1. ALPHA detector and MS allow the measurement with high time resolution, which is needed for unsteady-state operation. In combination with these techniques, GC allows the quantitative detection of H₂ (IR transparent) and a more accurate distinction of the different carbon-containing species compared to MS in which the ion fragmentation leads to equivocal signal assignment.

2.3.4 Spatial analysis module

The spatial analysis module is shown in Scheme 2.4 and Figure 2.2. It consists of a base platform on which two supports are placed: one is fixed directly to the platform, keeping the tube in position, the other one is connected to the x-moving stage, controlled by computer. It allows precise movement with minimum distance of 100 μm. A tubular channel, connected to the reactor longitudinally, contains the fused silica capillary (OD: 650 μm, ID: 150 μm) used for in-situ gas sampling. The rubber bellow ensures the sealing while the distances between the two stages is changed. One end-tip of the capillary is placed at the end of the catalyst bed, another end-tip is connected to the detector, GC or MS. The capillary is inserted in the tubular channel and the connection ensured by a 1/16 female nut and graphite ferrule. When running the spatial-resolved gas sampling experiment, the gas is sucked from the end-tip inside the reactor and goes to the detector through the capillary. The spatial profile of the composition in the gas phase is obtained then by step movement of the x-moving stage, with the capillary end-tip sliding from the end to the front of the catalyst bed. To be

noticed, when the gas analysis is performed by GC, a vacuum pump (Vacuumbrand) and a metering valve are connected to the outlet of the GC. The combination creates a mild driving force enabling to suck the gas with a flow rate of less than 5 mL/min. For measuring the spatial temperature profile, a K-type thermocouple replaces the capillary inserted into the catalyst bed. The thermocouple is connected to a temperature reader (Watlow).



Scheme 2.4 - Spatial analysis system.

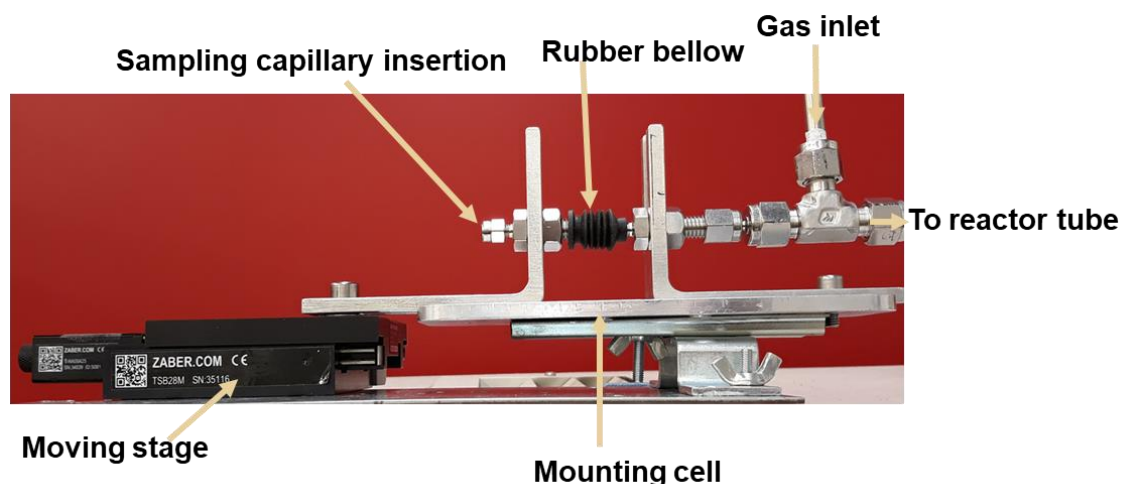
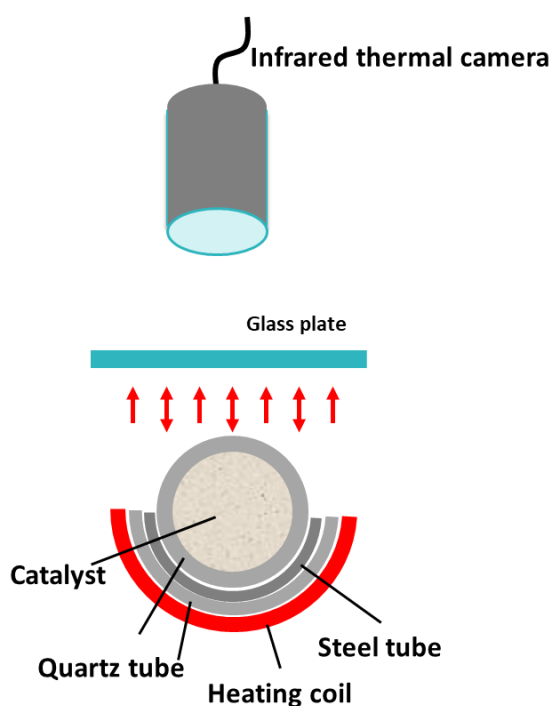


Figure 2.2 - Picture of Spatial analysis module.

2.3.5 Visualization analysis module

The module of visualization analysis refers to a combination of two instrumentations and related techniques. An USB camera and an infrared camera (IR camera, Micro-SWIR™ 320CSX Camera, Sensors Unlimited) are placed on the top of the reactor, as illustrated in Scheme 2.5 and Figure 2.3. In the view of implementing this technique, the reactor setup was modified with the following implementations. The quartz reactor

tube is half coiled with the resistance heating alloy line, avoiding the obstruction of the optical path in the upper part of the reactor. With a glass plate on the top of reactor tube channel in the furnace, the heat is reserved inside the furnace, visible light and short wavelength infrared are able to go out and be detected by the corresponding cameras which are both connected to the computer. The USB camera, correctly placed and focus on the catalyst bed, is able to acquire images and videos, detecting visible changes during reaction. For the infrared camera, the temperature profile is not directly obtained. To gain that, a preliminary calibration step has to be performed (details in section 2.4.2).



Scheme 2.5 - Infrared thermal camera measurement system.

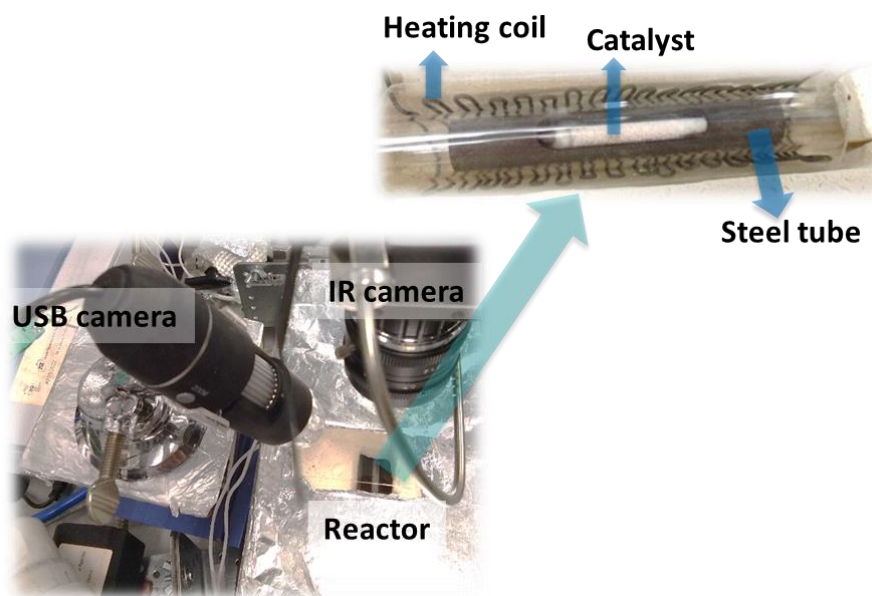


Figure 2.3 - Picture of the visualization system.

2.3.6 Microwave reactor system

Heating by exposure to microwave radiation has been evaluated as an efficient way to enhance the reaction rate in heterogeneous catalysis⁶. Thanks to its ability to heat the solid catalyst selectively, this technique has the potential to suppress CH₄ partial or total oxidation in gas phase during OCM⁷. The system consists of a microwave generator, an aggregator, a cavity with a quartz reactor (OD: 6 mm) inserted inside, an infrared temperature sensor and a computer as shown in Figure 2.4. The solid catalyst, loaded in the quartz reactor, is located in the middle of the cavity. The microwave radiation generated ($2.45 \text{ GHz} \pm 50 \text{ MHz}$) goes through the tuner and reaches the cavity, where it can heat up the catalyst. The tuner can adjust the ratio of the reflected microwave to the input microwave. The temperature of the catalyst is monitored by the IR temperature sensor and the resonance frequency of microwave inside the cavity is measured by the detector. With the feedback of these two parameters, a LabVIEW program allows controlling the catalyst temperature and/or the heating power.

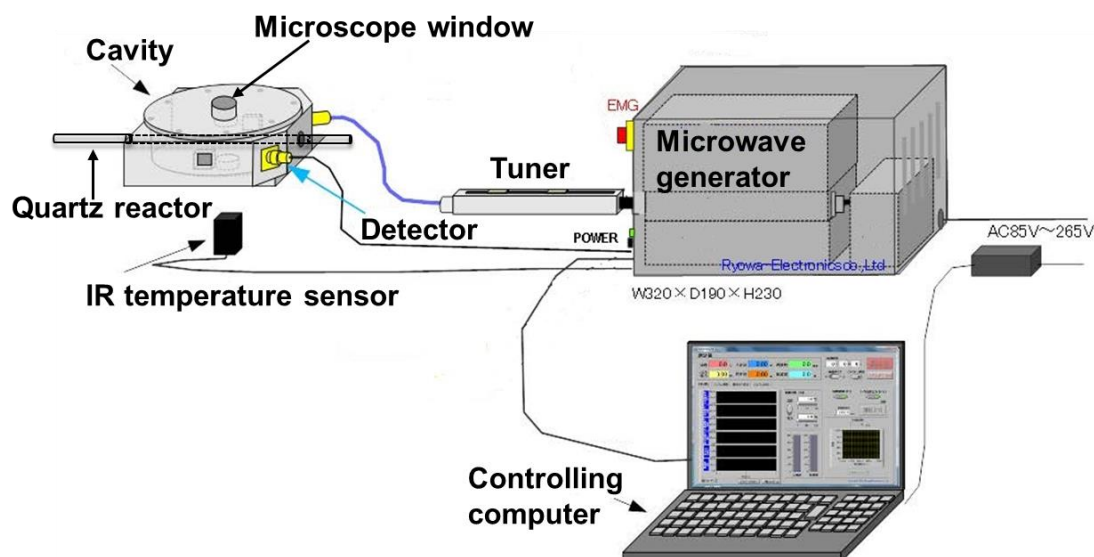


Figure 2.4 - Scheme of microwave heating system.

Thanks to its compact size, the microwave heating system is easily integrated in the OCM and DRM reaction system (Figure 2.1, Scheme 2.3) by simply replacing the furnace with the cavity previously described.

2.4 Methods

2.4.1 Alpha calibration

The ALPHA infrared spectrometer (ALPHA) is an instrument analyzing gas composition via the technique of infrared spectroscopy. Those gas molecules exhibiting dipole moment change for some vibrational modes are 'active' for infrared, and the molecule absorbs the infrared with the same frequency of its vibration. Different gases have different structures, thus their characteristic infrared absorptions happen at different frequencies.

According to Lambert-Beer law, the intensity of this absorption, namely absorbance, is proportional to the optical path length and the molar concentration of the corresponding molecular. In the spectrometer, the optical path length is fixed. Hence, it is possible to determine the amount of different gases by analyzing the absorbance of their characteristic infrared absorption. The data ALPHA acquired is the infrared absorption spectrum of the exhaust flowing into it, like Figure 2.5. The absorption is not at a specific wavenumber (a parameter inversely proportional to frequency) point, but at a range of wavenumber due to the rotation vibration mode of molecules. To

determine the concentration of a target species in the gas flow, a relation between absorbance and concentration is obtained in the calibration step, by acquisition of spectra of known calibration mixtures. Based on this, with a spectrum of unknown gas composition, the gas concentration of each analyte can be calculated by integrating the area of the chosen characteristic absorption peak and taking it into the mathematic relation built during calibration.

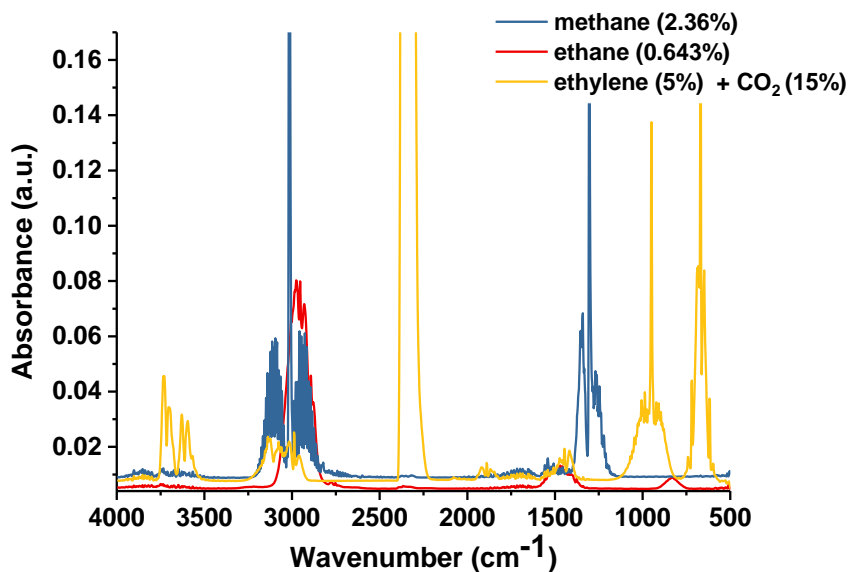


Figure 2.5 - IR absorbance spectra of methane, ethane, ethylene and CO₂.

The main species of interest in the context of this thesis are CO₂, CO, CH₄, C₂H₆, C₂H₄, H₂, He, N₂, H₂O. Among them, H₂, He, N₂ are IR 'inactive' while quantification of H₂O is not performed because of the presence of a water condenser in the outlet line. Figure 2.5 shows some of the IR spectra of the species of interest. To deal with the presence of overlapping regions of the spectra, the calibration has to be performed at frequencies that are specific for each analyte. In addition, regions of the spectra showing saturation of the absorbance when the corresponding species presents in high concentration, have to be avoided, in order to verify the relation between concentration and absorbance. Based on these two principles, we choose 2260 – 2280 cm⁻¹, 2040 – 2060 cm⁻¹, 1200 – 1220 cm⁻¹, 2850 – 2990 cm⁻¹ and 940 – 960 cm⁻¹ for CO₂, CO, CH₄, C₂H₆ and C₂H₄ quantification respectively. To be mentioned, C₂H₆ is a special case since its absorption peaks are highly overlapped with CH₄ and C₂H₄. The wavenumber range we chose for its quantification mainly overlaps with absorption peak of CH₄. For the calibration of C₂H₆, the standard sample should not contain CH₄. For C₂H₆

quantification in OCM reaction results, CH₄ absorption peak is mathematically removed by subtracting the spectrum of pure methane with multiplying a constant factor from the targeted spectrum. The constant factor is obtained by fitting the targeted spectrum to the spectrum of pure methane in the range of 3050 – 3250 cm⁻¹ where methane absorption peak prevails.

In order to complete the calibration, the spectra of different gases with known composition and concentration are acquired. Since the model is linear, at least three different concentration levels are needed for each gas. With the spectra of different calibration gases, we can get the specific areas of chosen wavenumber range for each gas with different concentrations. After that, the mathematic model is built between these two variables for each gas. For CO₂ hydrogenation part, carbon balance was applied to confirm the precision of the models built and the variation is controlled within $\pm 5\%$. For OCM during unsteady-state operation, carbon balance is no more suitable since the conversion is limited, thus GC measurement is applied at some points to crosscheck the quantification result. A specific MATLAB script is developed and optimized for performing the calculation, ensuring a fast analysis and reliable quantification.

2.4.2 IR camera calibration

Every material above 0 K, that possesses thermal energy, can emit electromagnetic radiations^{8, 9}. According to Planck's Law¹⁰, the intensity and the frequency distribution of this radiation is a function of the object temperature. The wavelength at which the maximum emission intensity occurs is inversely proportional to the temperature and is determined by Wien's Law. For a catalyst subjected to high temperatures, as is the case of the reactions here investigated, a thermal radiation in the region of infrared is expected. Considering that quartz is transparent for the spectral region of interest, an infrared camera is a suitable analytic tool to measure the temperature of the catalyst bed.

The IR camera is a device that detects infrared radiation and converts it to digital signal. The digital signal is and saved as the pixel in pictures of observed objects. Here we make use of an IR camera with high sensitivity in the wavelength interval of 0.9 – 1.7 μm . The output pixel in the IR camera picture is scaled intensity of the infrared radiation detected on the surfaces of the object. To convert it to temperature, a calibration is

needed to relate the intensity of the infrared radiation to the temperature of the targeted object.

The targeted object here is the catalyst bed. During the calibration, 2000 pictures of the catalyst bed surface at each temperature were taken with the IR camera. The average pixel value of observed surface of catalyst bed is chose to build the mathematic model with the temperature. As mentioned in section 2.3.3, the heating controller used in the furnace is a PID controller. Figure 2.6a shows the periodic fluctuation of infrared radiation of SiC heated up with the PID heating controller. To make the calibration more accurate, a direct current heating power supply is applied in the furnace, resulting in a more stable infrared radiation (Figure 2.6b). With the average value of the 2000 pictures at each temperature, a linear model can be built as shown in Figure 2.7.

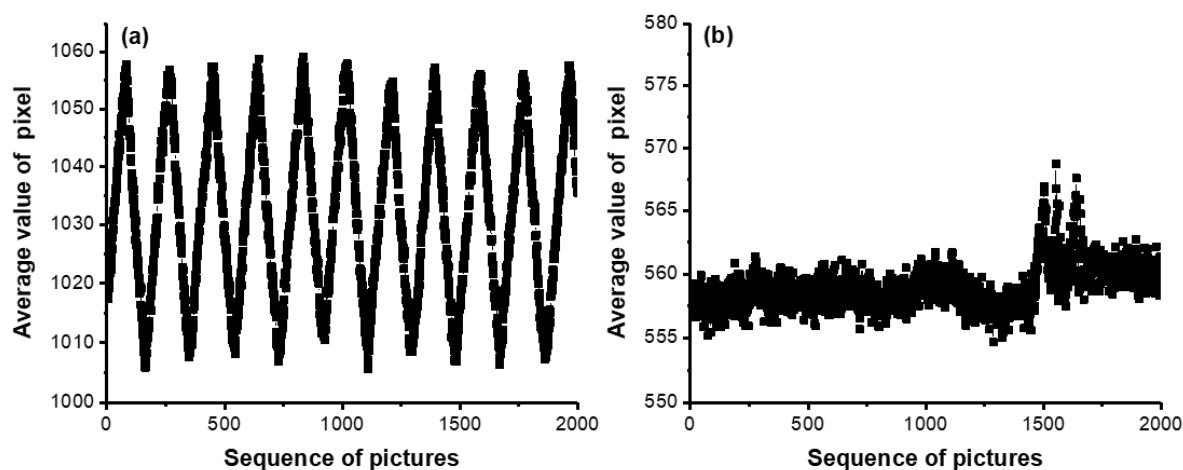


Figure 2.6 - Average value of pixels in the pictures of SiC heated up with different heating method: (a) PID heating controller, 800 °C; (b) Direct current heating power supply, 797.7 °C.

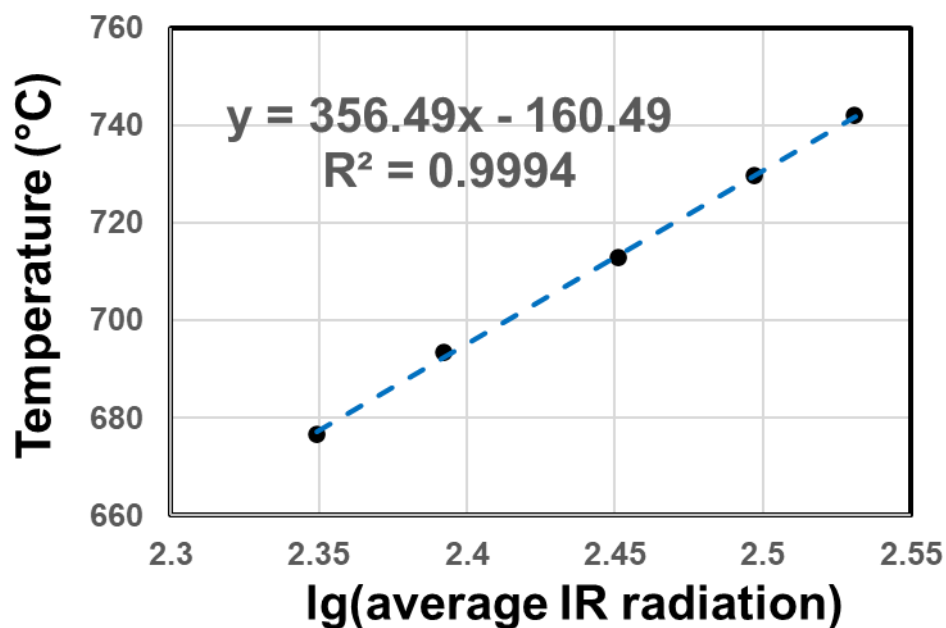


Figure 2.7 - A linear fitting between logarithm of averaged pixel value and the corresponding temperature.

To be noticed, the intensity of IR radiation that the camera detects varies with the distance between the observed object and the camera, the angle between the observed surface and the camera, the focus and exposure of the camera. Besides, different materials have different emissivity of thermal radiation. Considering that, before each measurement, the calibration was performed on the same material with the fixed camera settings and distances. The calculation is performed by proper MATLAB script, making use of the Image processing toolbox.

2.4.3 Reaction operation and data analysis

In this thesis, the reactions were performed in two main operation modes: steady-state operation and unsteady-state operation. The former is a conventional co-feed strategy, with the different gases mixed before reaching the reactor. The latter consists of alternate pulses of different reactants to the reactor: CO₂ and H₂ in CCR case; CH₄, O₂ and/or He in OCM case; CH₄, CO₂ and/or He the case of DRM. A LabVIEW program is made to control the setup described in section 2.3.3. The interface of the LabVIEW program is shown in Figure 2.8. It consists of four sections: 4-way valve control, MFC control, OPUS control and cycle mode control. When the valves are set in 'Manual', steady-state operation is performed by fixing the two valves at B position as mentioned

in section 2.3.3. When the valves are set in 'Auto' state, unsteady-state operation is possible.

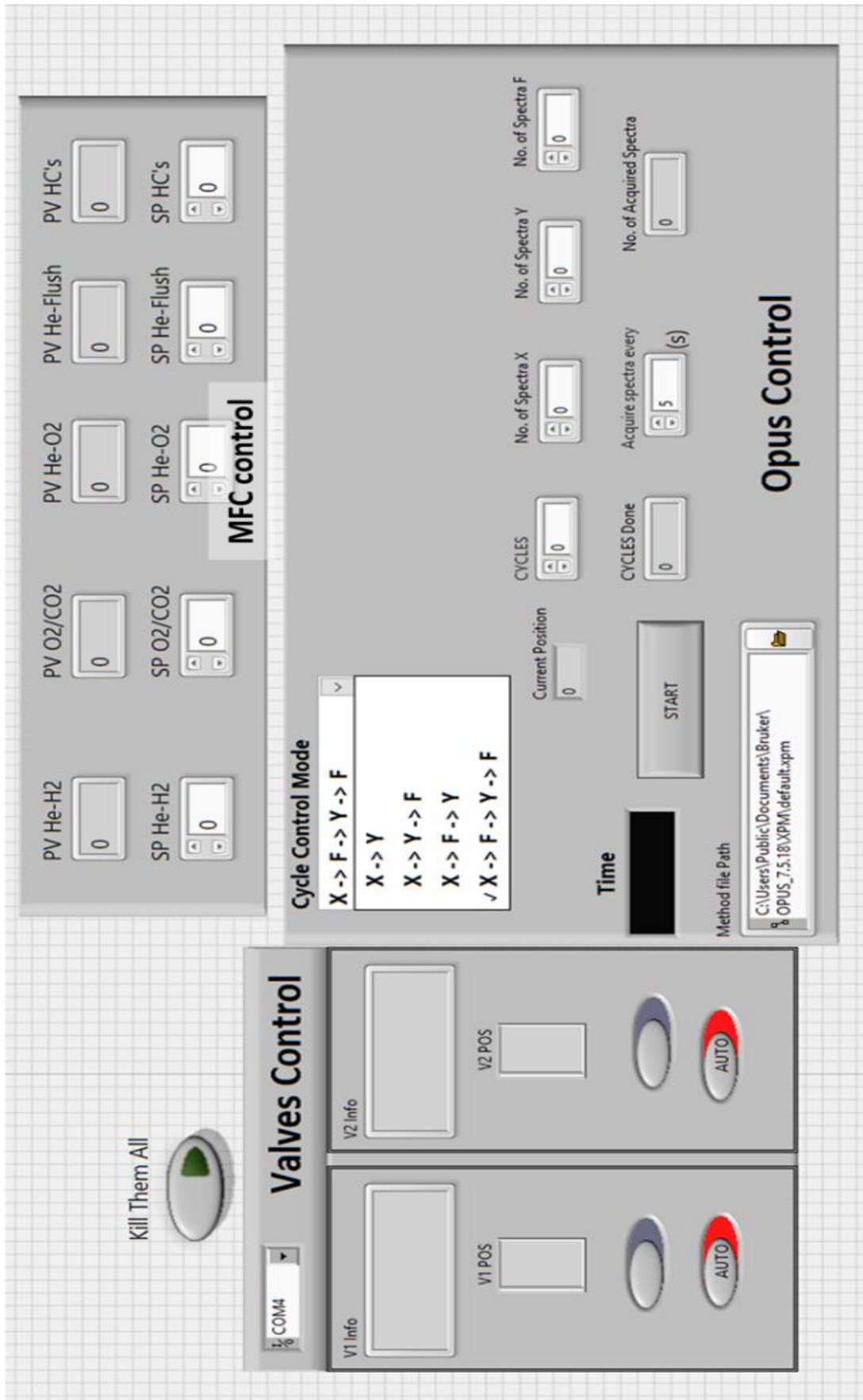


Figure 2.8 - The interface of unsteady-state operation controlling LabVIEW program

Unsteady-state operation has four different modes: $X \rightarrow Y$, $X \rightarrow Y \rightarrow F$, $X \rightarrow F \rightarrow Y$, $X \rightarrow F \rightarrow Y \rightarrow F$ (X: O_2/CO_2 , oxidant phase; Y: CH_4/H_2 , reductant phase; F: pure He, flushing phase). The phase length is controlled by the number of spectra acquired by ALPHA and the interval time between two spectra (interval time > required time for acquiring one spectrum). The fast response of ALPHA (2 – 3 s) ensures the on-line monitoring of each phase. The alternation of pulses is implemented by the combination of the 4-way valves positions as listed in Table 2.1. To improve the signal/noise (S/N) of the detection and make sure the result is reproducible, at least six cycles were conducted for each unsteady-state evaluation. The final profile is the average of cycles from the second to the last, thus discarding any initial non-reproducible behavior of the first cycle.

For CCR, only one 4-way valve is used, so that only one mode, i.e. $CO_2 \rightarrow H_2$, was applied.

2.4.4 Catalytic activity characterization parameters

Catalytic activity is evaluated with the following parameters:

- Re conversion: reactant conversion (CO_2 and H_2 in CCR; CH_4 and O_2 in OCM, CH_4 and CO_2 in DRM);
- P selectivity: product selectivity (CO and CH_4 in CCR; C_2H_6 , C_2H_4 , CO , CO_2 , H_2 and H_2O in OCM, CO in DRM);
- P yield: product yield

These quantities are defined as follows:

$$\text{Re conversion} = \frac{\text{mole of converted Re}}{\text{total mole of Re in the feed}} \times 100\%$$

$$\text{P selectivity} = \frac{\text{mole of needed carbon – containing Re for producing P}}{\text{mole of converted carbon – containing Re}} \times 100\%$$

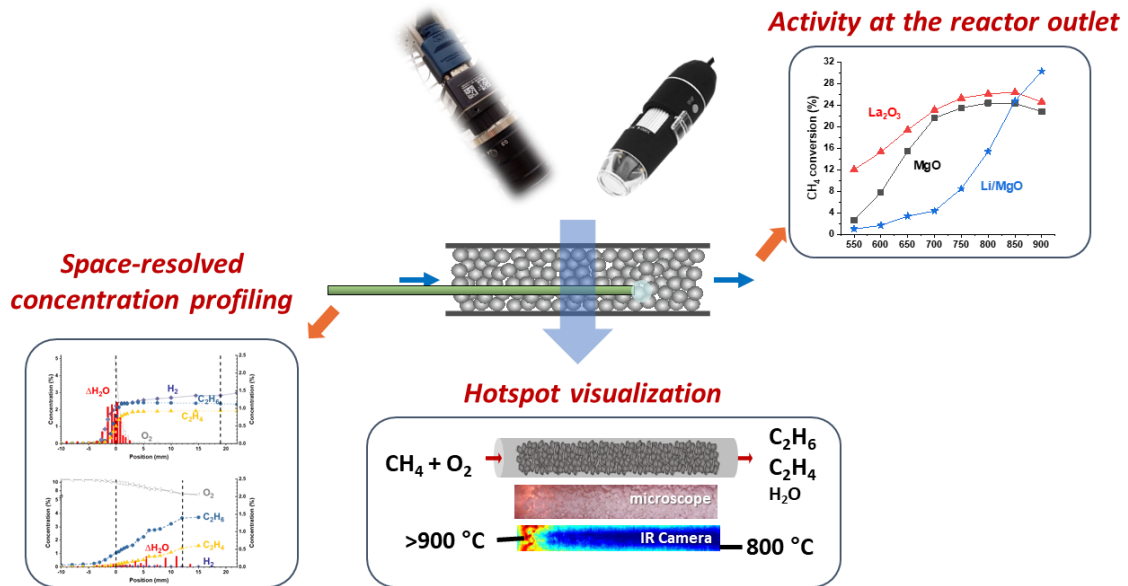
$$\text{P yield} = \frac{\text{mole of needed carbon – containing Re for producing P}}{\text{total mole of carbon – containing Re in the feed}} \times 100\%$$

Bibliography

1. N. Deraz, *J Ind Environ Chem.* 2018; 2 (1): 19, 2018, **21**.
2. C. Perego and P. Villa, *Catalysis Today*, 1997, **34**, 281-305.
3. L. Lloyd, D. Ridler and M. Twigg, *Wolfe, London*, 1989, 283.
4. K. P. de Jong, *Deposition precipitation*, Wiley– VCH Publishers: Weinheim, Germany, 2009.
5. C. C. Koch, *Nanostruct. Mater.*, 1997, **9**, 13-22.
6. D. Stuerge and P. Gaillard, *Tetrahedron*, 1996, **52**, 5505-5510.
7. G. Roussy, E. Marchal, J. M. Thiebaut, A. Kiennemann and G. Maire, *Fuel Process. Technol.*, 1997, **50**, 261-274.
8. M. F. Modest, *Radiative heat transfer*, Academic press, 2013.
9. J. R. Speakman and S. Ward, *ZOOLOGY-JENA*, 1998, **101**, 224-232.
10. R. Siegel, *Thermal radiation heat transfer*, CRC press, 2001.

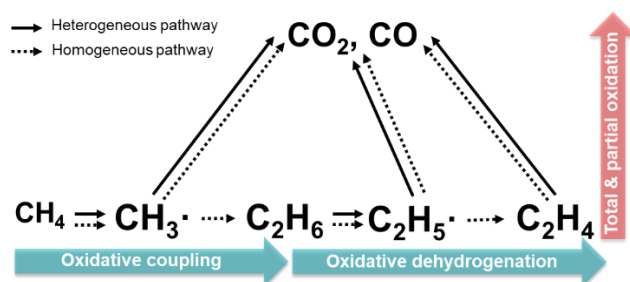
3 OCM IN COFEED MODE

Catalytic oxidative coupling of methane:
heterogeneous or homogeneous reaction?



3.1 Introduction

Converting methane to valuable chemicals is an imperative way to efficiently make use of relatively limited nature gas, comparing to simply burning it to generate heat or electricity. Currently, the commercialized methane transformation is based on an indirect route: CH₄ – CO and H₂ – diverse chemicals. The extra process leads to high demand of energy and cost. Direct methane converting routes is more attractive in a view of economic advantages. Among them, oxidative coupling of methane (OCM), simply upgrading methane to more valuable industrial feedstock -ethylene - in an exothermic environment as illustrated in equation (1), is considered as a ‘dream reaction’ and has attracted intensive attention in last decades¹. In reality, OCM is a complex reaction due to multiple interconnected parallel and series reactions under typical OCM conditions, which arise from the radical intermediate reaction nature of OCM (Scheme 3.1). These homogeneous parallel reaction pathways leads to sacrifice of C₂H₆ and C₂H₄ (C₂) selectivity when increase CH₄ conversion², resulting a low upper bound of C₂ yield and finally restricting OCM commercialization.



Scheme 3.1 Reaction networks in OCM system

To alter the trade-off between C₂ selectivity and CH₄ conversion, catalysts are applied. This increases the complexity of the reaction because of the heterogeneous reaction steps on the catalyst surface, This complexity obstructs the study of the impacting factors and optimizing OCM reaction conditions. The side total & partial oxidation reactions as illustrated in Scheme 3.1 are highly exothermic, making the catalyst bed temperature uncontrollable. Furthermore, huge temperature gradients along the catalyst bed have been witnessed³. These generate a question: is it reliable to evaluate

catalysts with conventional catalytic activity method, i.e. studying the vent composition, since temperature is closely related with methane activation⁴ and oxygen activation⁵. Notwithstanding it is possible to avoid the temperature variation by using customized micro reactor, it is far from the realistic catalyst working condition⁶. To understand the real role of the catalyst, combining traditional methods with advanced spatial analysis tools which offers the detail information of the reaction⁷ is promising as shown in this work.

3.2 Experimental

3.2.1 Catalyst preparation

MgO ($\geq 99\%$ trace metal basis, Sigma Aldrich) and La₂O₃ (99.99%, Alfa Aesar) were used as simple metal oxides catalysts directly without any further treatment. The doped catalysts were prepared via a direct solid mixing method. The simple metal oxides and corresponding dopant metal carbonate salts (SrCO₃ for La₂O₃ and Li₂CO₃ for MgO) were mixed respectively in agate mortars with certain amount deionized water. After that, the slurry was dried in the oven at 80 °C for 12 h, then calcined in the furnace at 800 °C for 4 h.

3.2.2 Catalyst characterization

Power X-ray diffraction (PXRD) was performed on D8 Advanced Powder Diffractometer (Bruker) equipped with a vertical 2theta-theta goniometer in transmission configuration, with a K α_1 germanium monochromator for Cu radiation ($\lambda=1.5406 \text{ \AA}$), at a scan step of 0.02°/s from 10° to 80°.

3.2.3 Catalytic reactions

The reaction setup is the one described in Chapter 2 (Section 2.3.3). 200 mg of catalyst material (pelleted, crushed and sieved to the size of 300-400 μm) was charged into a quartz tube reactor, fixed with quartz wool. To be mentioned, for La₂O₃, the catalyst was pre-oxidized in 50 vol.% O₂ in He (50 mL/min) at 700 °C for 30 min before reaction. The reason to do this is that La₂O₃ is very sensitive to moisture in the air. From the XRD profile (Figure 9.1) we can only find characteristic peaks of La(OH)₃ rather than La₂O₃ in the profile of directly purchased La₂O₃ and it is able to get clean La₂O₃ diffraction patterns simply by oxidizing the sample under the condition mentioned

above. This re-oxidized La_2O_3 can be completely hydrated at room temperature with the sample vial closed.

Then a mixture of 40 vol.% CH_4 (Abelló Linde), 10 vol.% O_2 (Abelló Linde), 13 vol.% N_2 and 37 vol.% He with a total flow rate of 80 mL/min was introduced into the reactor. The reactor temperature was controlled by a Watlow heating control with a thermocouple inserted at the end of catalyst bed. The exhaust was analyzed by a gas chromatography (GC, Agilent 7890B, equipped with two FID and one TCD) after passing through a mini-water-condenser cooled by water circulation. For the experiment studying H_2 formation effect, 1.46 vol.% H_2 was added into the feed and N_2 volume portion goes to 11.54%.

3.2.4 Spatial analysis and visual inspection

Gas spatial analysis tool is the module described in Section 2.3.4 of Chapter 2. For the temperature and catalyst bed visualization, the reactor furnace cover was modified by opening a ca. 3 cm × 1 cm window on it and the window was covered with a glass plate which is transparent to short wave length infrared light and visible light. An USB digital microscope (800 - 1000× magnification) was used to obtain zoom-in images and videos at the level of the catalyst particles. Meanwhile, the infrared camera (Micro-SWIR 320CSX camera, Sensors Unlimited) was settled to take thermal images that can be converted to temperature images after calibration of the infrared camera placing at the same position.

3.3 Results and discussion

To avoid generating puzzles, simple metal oxide, La_2O_3 and MgO , typical active OCM catalysts were studied. The gross catalytic activity of La_2O_3 evaluated with classic method is superior than that of MgO in terms of CH_4 conversion and C_2 yield (Figure 3.1A, C), especially at low temperature range (550 – 650 °C) with remarkable partial oxidation products formation (CO and H_2 , Figure 3.1B, D). We suspect that the superiority of La_2O_3 is related with its preference for unselective partial oxidation reaction. This suspect was confirmed by evaluation of the intrinsic catalytic activity obtained on La_2O_3 when only CH_4 was present in the flow (Figure 3.2A). The transient profiles of CO and H_2 signals show high coherency, confirming the existence of a partial oxidation route, with lattice oxygen providing high selectivity towards this route.

The observable higher C₂ formation with MgO comparing to La₂O₃ under this unsteady state operation gives the opposite conclusion about the catalytic activity: MgO is intrinsically more inclined to OCM than La₂O₃. The total and partial oxidation reactions are strongly suppressed when only lattice oxygen presents as oxidant, indicated by the limited CO formation and barely produced CO₂, which agrees with other transient experiments^{8, 9}. This verifies that the heat effect on the dominant catalytic activity coming from these highly exothermic reactions is negligible here. Therefore, for the intrinsic OCM catalytic activity, MgO is superior than La₂O₃. In another word, the superiority of La₂O₃ in presence of O₂ is not coming from the intrinsic OCM catalytic activity but related with other reactions in the system.

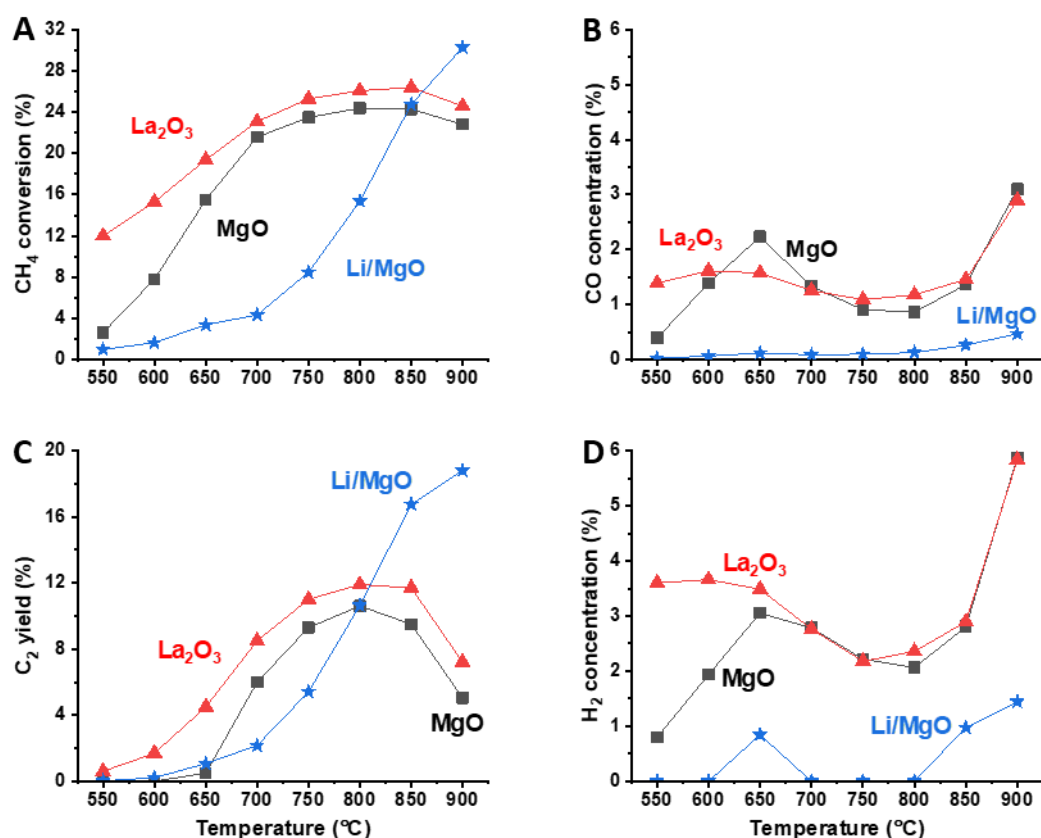


Figure 3.1 Catalytic performance evolution of MgO (black), La₂O₃ (red) and 5 wt.% lithium doped MgO (Li/MgO, blue) in terms of CH₄ conversion (A), CO concentration (B), C₂ yield (C) and H₂ concentration (D) during OCM under steady state operation (CH₄/O₂ = 4, 80 mL/min, He and N₂ diluted, N₂ also plays as inner standard for gas chromatography analysis) at different temperatures.

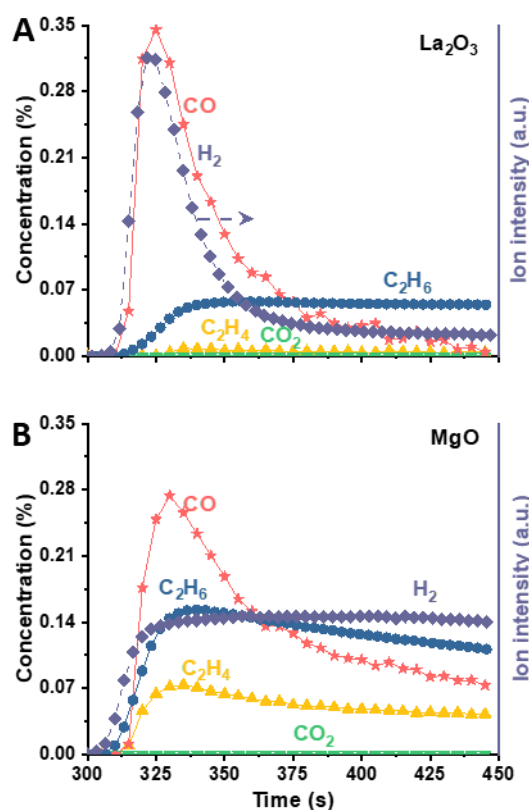


Figure 3.2 Concentration of C_2H_6 , C_2H_4 , CO_2 and CO and ion intensity of H_2 ($m/z = 2$) in methane phase during OCM under unsteady state operation on La_2O_3 (A) and MgO (B) at $900\text{ }^\circ\text{C}$. C_2H_4 , CO_2 and CO concentration is quantified based on infrared spectra and C_2H_6 concentration is quantified with mass spectrometer data which is calibrated via simultaneous gas chromatography result, both are the average value of last three cycles.

To be addressed, lattice oxygen of the catalysts can be only activated at very high temperature (traces of partial oxidation products at $700\text{ }^\circ\text{C}$ and OCM products only at $900\text{ }^\circ\text{C}$) for unsteady state operation. Interestingly, the co-feed catalytic performance gets close for the two catalysts when temperature reaches $700\text{ }^\circ\text{C}$ where O_2 is almost fully consumed and CH_4 total and partial oxidation products reach similar level (Figure 3.1 and 9.2). In this case, theoretically the gross heat effect from the highly exothermic oxidation reactions is getting equivalent for the two catalysts. To study this heat effect in reality, the USB camera and infrared camera have been applied. They visually demonstrate that the distinguishable hotspot (Figure 3.3A, B) only presents in the front of catalyst bed, inferring the reaction gradients along the catalyst bed. Further spatial temperature measurement (Figure 3.3C) reveals that the temperature rise starts before

the catalyst bed, and there is difference between the hotspots of the two catalysts: the hot zone in La_2O_3 is in the more front position of catalyst bed than that in MgO , which suggests that reactions happen more intensively in front of La_2O_3 .

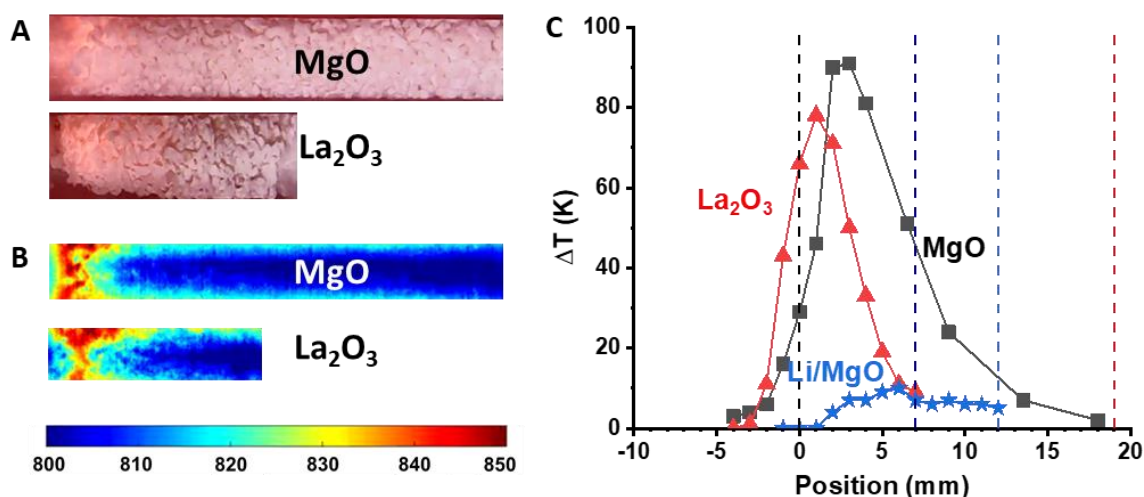


Figure 3.3 Visualization and quantification of hotspot formed during OCM under steady state operation on MgO and La_2O_3 respectively at 800 °C: A, images of catalyst beds obtained by general USB camera; B, images of catalyst beds acquired via infrared camera; C, spatial temperature rise (ΔT) profile, the temperature rise is calculated by subtracting the temperature measured with 10 vol.% O_2 in N_2 at 800 °C from the temperature measured during OCM under steady state operation (same feed as used in Figure 3.1) at 800 °C at respective positions on corresponding catalysts.

The reaction gradients suggested by catalyst bed temperature profile are confirmed in the spatial gas concentration profile (Figure 3.4A, B). In agreement with other spatial gas analysis, products are mainly produced in the front of catalyst bed^{7, 10, 11}. Rapid O_2 consuming happens within 2 mm for MgO but 1 mm less for La_2O_3 in the front of catalyst bed, which means the rest of catalyst bed does no positive effect on the final catalytic performance and can be detrimental with gas phase O_2 presence considering the decaying of C_2H_6 or C_2H_4 concentration after the initial peak value. As an evidence, the slightly better catalytic activity of MgO in much less amount (40 mg, comparing to 200 mg) when temperature is up to 700 °C (Figure 9.3) confirms that only small portion of catalyst in the front functions in the reaction system. Impressively, products appear even before the feed reaches catalyst bed, which is more conspicuous for La_2O_3 at 700 °C and gets distinct when temperature is lifted up to 800 °C for MgO (Figure 9.4A,

B). This phenomenon is observed for the first time here. One plausible explanation is that it is simply the back diffusion of products. However, the addition of SiC in the front of the catalyst bed does not lead to substantial reduction or elimination of the phenomenon (Figure 9.5). Furthermore, O₂ depletion occurs less deep in the catalyst bed and larger amount of unselective oxidation products are formed, which are symptoms of gas phase reaction dominated reaction system. Considering the radical mediated reaction nature of OCM, it is reasonable to deduce that homogeneous reactions prevail on these two simple metal oxides especially at high temperature range (≥ 700 °C). Radicals formed on the front catalyst surface initiate the gas phase reactions and it explodes to the catalyst-free zone because the relatively inert quartz wool or SiC in front does not quench or further reacts with these radicals. In this way, high temperature is needed to generate enough initiator radicals rapidly to keep the homogeneous reaction zone. That is why this phenomenon can become distinct as temperature increases (Figure 4A and Figure 9.4A) and the catalytic activity reaches maximum once homogeneous reactions are fully decisive. The C₂ yield decay passing the maximum point is caused by the C₂ reforming reactions according to spatial analysis of OCM on MgO at 850 °C (Figure 9.6).

Astonishingly, La₂O₃ can have almost all products prompt formation in catalyst-free zone even at 700 °C. Among these products, H₂ concentration rise shows up earlier than other products for both catalysts. According to Maxwell distribution of speeds, the lighter molecular diffuse faster, which explains that H₂ back diffuse further away from the catalyst bed. At 0 mm, La₂O₃ gives 3.6 vol.% H₂, almost double of that (1.9 vol.%) given by MgO. Higher concentration gives larger diffusion driving force, enabling H₂ back diffusing further in front of La₂O₃. 'Hot' H₂ and O₂ react forming H₂O and it is confirmed by spatial H₂O formation profile calculated via oxygen balance which match with H₂ concentration rise. This oxidation reaction is also highly exothermic and can heat up the surrounding gases. This benefits C₂ formation which requires higher activation energy comparing to unselective oxidation reactions. Another rational deduction is that hydroxyl radicals are generated from water vapour heated up by the oxidation reactions. Hydroxyl radicals mediated OCM was reported to be more selective to C₂ formation via introducing H₂O into the feed¹². This explains the higher selectivity of La₂O₃. The positive effect of H₂ is later confirmed by adding 1.4 vol.% H₂ into OCM feed with SiC or La₂O₃ or MgO as catalyst (Figure 9.7). By placing a small

portion of La_2O_3 in front of MgO , we also confirm the significant enhancement of catalytic performance contributed by front La_2O_3 (Figure 9.8).

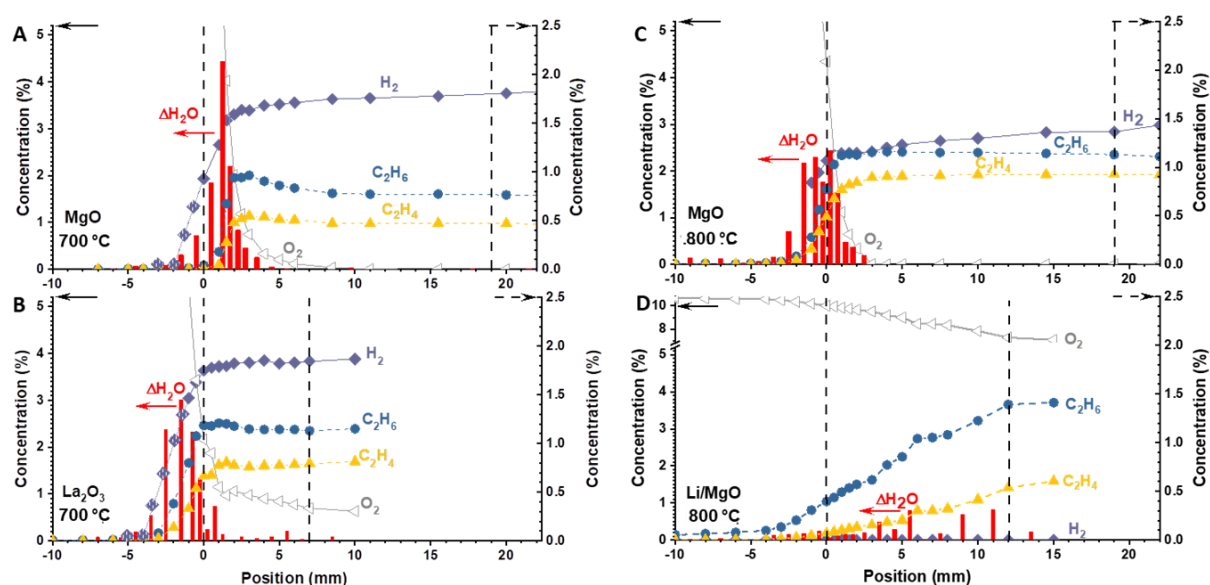


Figure 3.4 Spatial concentration profiles of O_2 , C_2H_6 , C_2H_4 , H_2 and formed water between two data points ($\Delta\text{H}_2\text{O}$) measured on MgO (A), La_2O_3 (B) and Li/MgO (C) during OCM under steady state operation (same feed as used in Figure 3.1 and 3.3) at $700\text{ }^\circ\text{C}$ for (A), (B) and $800\text{ }^\circ\text{C}$ for (C), (D). $\Delta\text{H}_2\text{O}$ is the difference value between H_2O amount at one position and H_2O amount at previous front neighbour position, H_2O amount is calculated based oxygen balance.

Through these discussions, the two simple metal oxides used here behave more as ‘trigger’ rather than catalyst role and only a small portion does the positive contribution during OCM when temperature is up to $700\text{ }^\circ\text{C}$. The prevailing homogeneous reactions limit the final C_2 yield. Is it possible to make the catalyst decisive in controlling C_2 yield?

As an effort, dopants are added into these two metal oxide. For Li doped MgO (Li/MgO), the superior C_2 selectivity has been reported in many works¹³⁻¹⁵. Here, we carefully compare the behaviours of pure MgO and Li/MgO under OCM conditions. As shown in Figure 3.1, the activity pattern is totally different from that of simple metal oxides: the evolution of CH_4 conversion and C_2 yield follows exactly same trend of simple rise with temperature increasing, and unselective oxidation reactions are strongly suppressed especially partial oxidation (Figure 9.2). These imply the real catalyst role of Li/MgO . The spatial gas concentration profile of OCM on Li/MgO at $800\text{ }^\circ\text{C}$ (Figure 3.4C) further verifies it with demonstrating a continuous C_2 formation all along the catalyst bed with

scarce H₂ production. The water formation is also limited comparing to the pure simple oxides. As a consequence, hotspot is not observed during OCM on Li/MgO (Figure 3.3). Strontium doped La₂O₃ (Sr/La₂O₃) also exhibits suppression of unselective oxidation reactions and homogeneous reaction in catalyst-free zone although the extent is much less (Figure 9.9 and Figure 9.4C). It is easy to understand that the reactions happen in different way here: from homogeneous reactions dominated way to heterogeneous reactions dominated way, which allows the catalyst achieve its function of altering the trade-off of CH₄ conversion and C₂ selectivity in OCM in the absence of catalyst. As shown in Figure 9.10A, C₂ selectivity and O₂ conversion grow up along the catalyst bed for Li/MgO but reach a stable value in the front rapidly for MgO. Furthermore, the relatively lower C₂H₄/C₂H₆ ratio of Li/MgO (Figure 9.10B) reveal its intrinsic selectivity to coupling of methane and less selectivity to consecutive oxidative dehydrogenation of C₂H₆ (ODH). This is another proof of detailed reaction mechanism change.

3.4 Conclusion

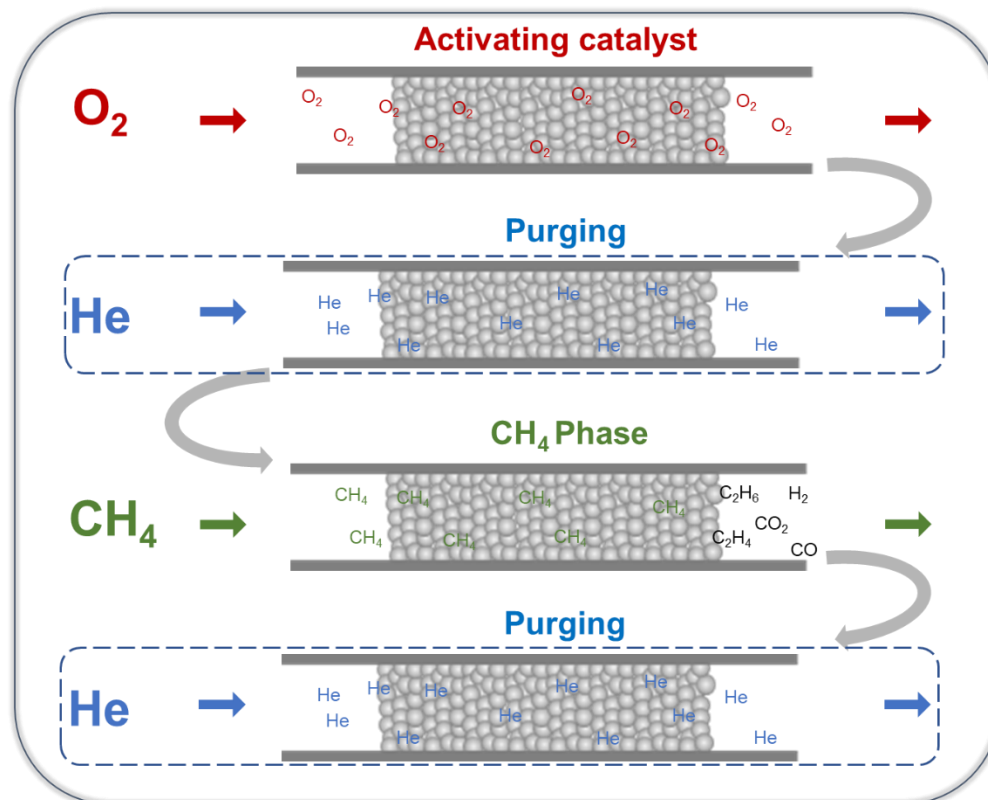
Different behaviours of simple metal oxides and doped ones points out different roles that they play in OCM reaction. Two types of reaction mechanism, homogeneous dominated reactions or heterogeneous dominated reactions, have been proposed. These findings confirm that single conventional evaluation method of catalytic activity is not always suitable in OCM reaction and diverse technologies are needed for acquiring comprehensive information in OCM system. Besides, how the dopant changes the reaction mechanism asks for more work. The mysteries may point the direction to efficient C₂ yield increase.

Bibliography

1. U. Zavyalova, M. Holena, R. Schlögl and M. Baerns, *ChemCatChem*, 2011, **3**, 1935-1947.
2. G. S. Lane and E. E. Wolf, *J. Catal.*, 1988, **113**, 144-163.
3. A. Aseem, G. G. Jeba, M. T. Conato, J. D. Rimer and M. P. Harold, *Chem. Eng. J.*, 2018, **331**, 132-143.
4. K. Otsuka and K. Jinno, *Inorg. Chim. Acta*, 1986, **121**, 237-241.
5. P. W. Wang, G. F. Zhao, Y. Wang and Y. Lu, *Science Advances*, 2017, **3**, E130180.
6. Z. Liu, J. P. Ho Li, E. Vovk, Y. Zhu, S. Li, S. Wang, A. P. van Bavel and Y. Yang, *ACS Catalysis*, 2018, **8**, 11761-11772.
7. B. Zohour, D. Noon and S. Senkan, *ChemCatChem*, 2013, **5**, 2809-2812.
8. V. Fleischer, P. Littlewood, S. Parishan and R. Schomäcker, *Chem. Eng. J.*, 2016, **306**, 646-654.
9. B. Benjamin, F. Vinzenz, A. Sebastian, G. H. Miguel, U. Atsushi, H. Peter and S. Reinhard, *Catalysis Today*, 2014, **228**, 212-218.
10. B. Zohour, D. Noon and S. Senkan, *ChemCatChem*, 2014, **6**, 2815-2820.
11. C. Karakaya, H. Zhu, B. Zohour, S. Senkan and R. J. Kee, *ChemCatChem*, 2017, **9**, 4538-4551.
12. K. Takanabe and E. Iglesia, *Angew. Chem. Int. Ed.*, 2008, **47**, 7689-7693.
13. A. Hirofumi, Y. Hiroyuki, N. Takashi, S. Takeshi, I. Seiichiro, K. Masataka, H. Sadao, T. Tsunehiro and Y. Satohiro, *The Journal of Physical Chemistry B*, 2000, **104**, 10133-10143.
14. J. A. Roos, S. J. Korf, R. H. J. Veehof, J. G. van Ommen and J. R. H. Ross, *Applied Catalysis*, 1989, **52**, 131-145.
15. C. Mirodatos and G. A. Martin, 1988.

4 OCM UNDER UNSTEADY STATE OPERATION

Studying intrinsic activity of catalysts during OCM via unsteady state operation



4.1 Introduction

The utilization of methane, the main constituent in natural and shale gas, in a high-value added way, is crucial for mitigating the environment and energy issues triggered by the huge consumption of crude oil. One efficient way to make use of methane is oxidative coupling of methane (OCM), which directly converts methane to ethylene, the raw material for plastics.

As generally accepted, methyl radical is firstly formed after the cleavage of C-H bond on the active sites, then released to the gas phase, coupled to form ethane¹⁻³. C-H bond breaking in ethane on the active sites leads to ethyl radical formation which further forms ethene in the gas phase⁴. The methyl radical and ethyl radical can also react with gaseous O₂ or reacts with oxygen species on the catalyst surface, leading to CO and CO₂ (CO_x) formation⁵⁻⁸.

To avoid the overoxidation of hydrocarbons by gaseous O₂, the chemical looping strategy was considered for OCM reaction. The strategy was firstly used for lifting up the energy efficiency in combustion process, which alternatively introduces fuel gas and O₂ into the reactor using metal oxides as reaction intermediates. Therefore, the active oxygen species on the metal oxides has to be able to remain in the inert feed without gaseous O₂. In catalytic OCM, lattice oxygen, weakly adsorbed oxygen, strongly adsorbed oxygen and oxygen vacancies on the catalyst surface are reported as the active sites for methane activation⁹⁻¹⁵. This makes it possible to operate chemical looping of OCM (CLOCM). Several groups have already successfully operated CLOCM using Mg₆MnO₈ and Na₂WO₄/Mn/SiO₂^{14, 16}. However, the active oxygen species can also oxidise methyl and ethyl radicals causing unselective products formation. The reactivity of the active oxygen species towards methyl and ethyl radicals has not been discussed in the reported CLOCM yet.

OCM under unsteady state operation

To study the activity and selectivity of different active oxygen species, an unsteady state operation with different modes was designed and applied herein to OCM based on two simple metal oxides, MgO and La₂O₃. O₂-containing feed, methane-containing feed (and pure He) were alternatively introduced into the reactor, creating different evolution pattern of gaseous O₂ while methane was activated on the catalyst. The behaviour of the catalyst during methane-containing feed at different modes of the unsteady-state operation was studied.

4.2 Experimental

4.2.1 Catalyst preparation

The preparation of the catalysts and the reaction system are exactly as described in Chapter 3.

4.2.2 Catalytic reactions

During unsteady state operation, O₂-containing feed, pure He and pure CH₄ are alternatively fed into the reactor via two 4-way valves. When O₂-containing feed is introduced into the reactor, the period of this flow is called catalyst activation phase (abbr. as X phase). Similarly, pure He flow is called purging phase (abbr. F phase) and pure CH₄ is called reaction phase (abbr. as Y phase). The abbreviations are defined based on the description of the unsteady state operation in Chapter 2. O₂-containing feed is 25 vol.% O₂ in He. During the reaction, all the feed was introduced into the reactor with the flow rate at 50 mL/min. CO, CO₂ and C₂H₄ in the outlet gas are tracked by ALPHA infrared spectrometer (Bruker).

The unsteady state operation in this Chapter involves three modes: periodic switching between X and Y phase (named as XY); periodic switching from X to F phase, then to Y phase (named as XFY), periodic switching from X to Y phase, then to F phase (named as XYF). If it is not mentioned specifically, each phase

OCM under unsteady state operation

lasted 150 s.

XFY was conducted at 850 °C to study the lifetime of active species by changing the length of F phase in the range from 0 s to 150 s. To study the coke behavior during Y phase, XYF was performed at different temperatures (650 °C, 700 °C, 750 °C, 800 °C, 850 °C) with the length of Y phase at three values (50 s, 150 s, 250 s). For the coke quantification, total amount of CO and CO₂ produced in X phase was integrated, which was originated from the re-oxidization of the coke formed in Y phase. At the same time, the catalyst bed was monitored by a camera through a glass window on the top of the reactor as shown in Chapter 2.

4.3 Results and discussion

An unsteady state operation of periodically flowing 25 vol.% O₂ (X phase) and pure CH₄ (Y phase) into the reactor was firstly conducted at different temperatures based on MgO and La₂O₃. Figure 4.1 displays C₂H₄ and CO concentration evolution during Y phase at different temperatures using MgO as the catalyst. When the flow is switched from O₂-containing feed to CH₄, the concentration of C₂H₄ increases rapidly to a peak value, then decays with time goes. The former corresponds to the filling of CH₄ into the reactor, while the latter is related to the depletion of gaseous O₂ in the reactor, namely less oxygen supply for reactivating the active sites after CH₄ activation on these sites and the desorption of weakly adsorbed oxygen species. The peak value of C₂H₄ concentration distinctly rises, while the decay slows down with the level-off value rising when the reaction temperature is up to 800 °C. These point out that the oxygen species towards the formation and releasing of methyl and ethyl radical is highly temperature-dependent, and 800 °C is the critical temperature for the activation of this active oxygen species.

OCM under unsteady state operation

For CO concentration profile, a totally different trend is observed: the peak value of CO concentration shows independent from the temperature change; a shoulder appears on the curve of CO concentration after the first peak value when the temperature reaches 800 °C. The former certainly proves that there are two types of oxygen species for the radical generation: one easily releases methyl and ethyl radical, favoring C₂H₄ formation; another one strongly adsorbs methyl and ethyl radical, leading to CO formation. The shoulder on the curve of CO concentration implies the activation of new type of active sites favoring CO formation at 800 °C. This type of active sites probably also contributes to the rise of level-off value of CO concentration starting at the same temperature.

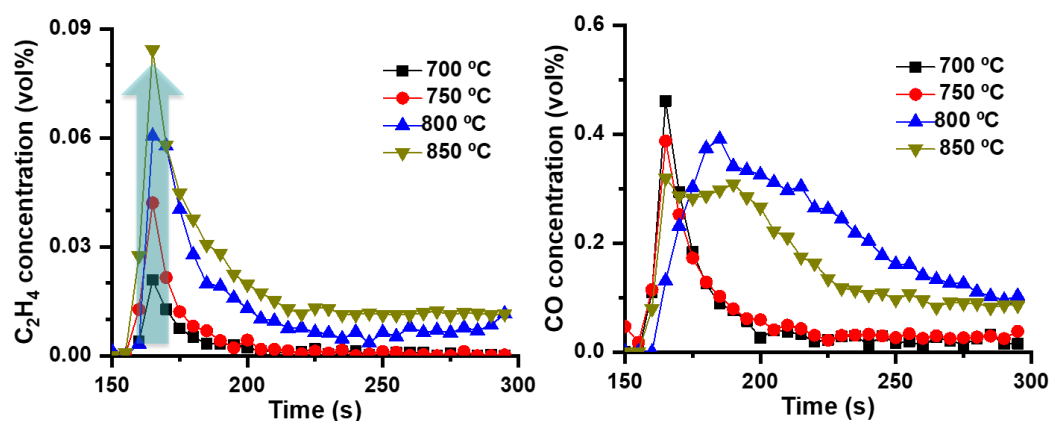


Figure 4.1 C₂H₄ and CO concentration in Y phase during OCM under XY mode on MgO at different temperatures.

As shown in Figure 4.2, similar trend of C₂H₄ concentration is found on La₂O₃ with higher peak value at low temperature range (≤ 750 °C) and less directional change of the level-off value on the decaying curve comparing the corresponding ones on MgO, which means the active oxygen species for C₂H₄ formation on La₂O₃ is also temperature-dependent, and its activity is higher than that on MgO at low temperature range (≤ 750 °C). For the evolution of CO concentration, the peak value also shows temperature dependence, especially

OCM under unsteady state operation

from 700 °C to 800 °C, which is different from the case of MgO. These suggests that there is only one type of active oxygen species on La₂O₃ probably.

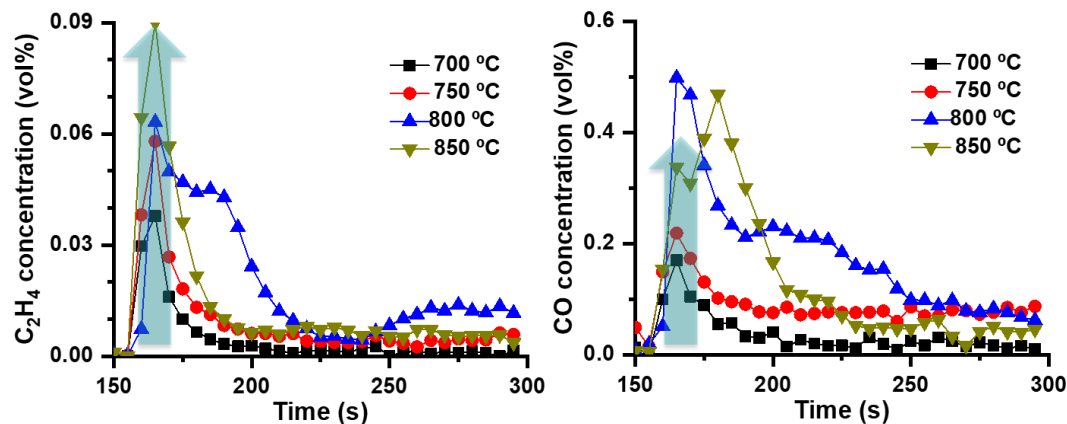


Figure 4.2 C₂H₄ and CO concentration in Y phase during OCM under XY mode on La₂O₃ at different temperatures.

To further evaluate the stability of all the active oxygen species, an XFY mode, adding a He flushing phase (F phase) with different length (0 s, 5 s, 10 s, 20 s, 50 s, 150 s) before switching from O₂-containing feed to CH₄, was applied to the two simple metal oxides at 850 °C, at which point all the active sites are activated based on the above results.

Figure 4.3 exhibits both C₂H₄ and CO concentration profile in F and Y phase obtained with MgO. The initial peak value of C₂H₄ concentration drops sharply with extending the length of F phase within 20 s, then stays almost stable at the level-off value in XY mode at 850 °C. Differently, the initial peak value of CO concentration shows little change while the shoulder on the curve gradually disappears with varying the length of F phase. This confirms that the oxygen species towards C₂H₄ and CO formation are different. As the available gaseous O₂ is neglect in the reactor when the length of F phase is 150 s, and the weakly adsorbed oxygen species hardly survive that long at 850 °C, it can be deduced that the active site is lattice oxygen or strongly adsorbed oxygen. Due to the

OCM under unsteady state operation

supplying cut of strongly adsorbed oxygen, the concentration of corresponding product should decrease along Y phase, which meets the profile of CO concentration. Therefore, strongly adsorbed oxygen has stronger interaction with formed methyl and ethyl radicals than lattice oxygen, contributing CO formation at the beginning of Y phase.

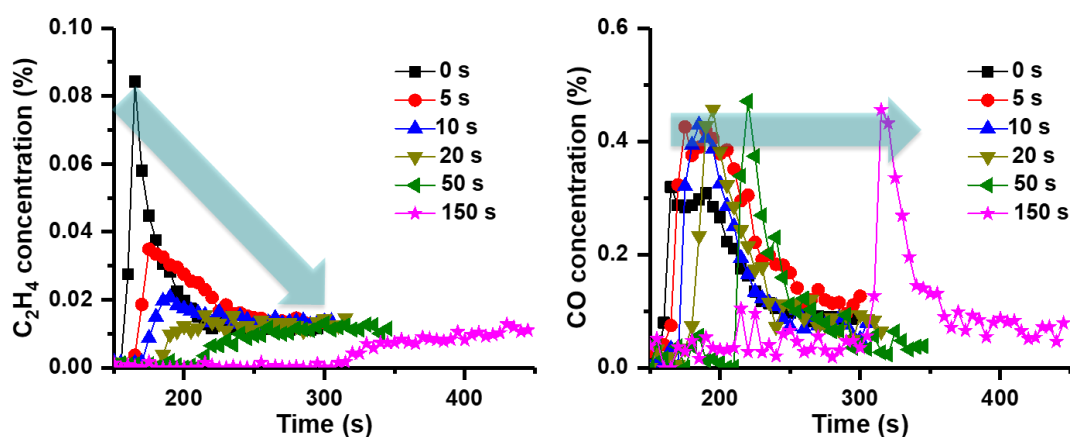


Figure 4.3 C₂H₄ and CO concentration in Y phase during OCM under XFY mode on MgO at 850 °C with the length of F phase varying from 0 s to 150 s.

The catalytic performance of La₂O₃ under XFY mode is shown in Figure 4.4. The peak value of C₂H₄ concentration drops rapidly to almost zero within 20 s of F phase. However, CO concentration behaves differently: the peak value increases firstly in 5 s of F phase, then gradually decreases to 0.4 vol% with the length of F prolonging. The fast dropping of C₂H₄ concentration and the maintained CO formation suggest that the active oxygen species on La₂O₃ have good activity to dissociate C-H bond in CH₄, but have strong ability to adsorb methyl and ethyl radical, resulting in higher CO selectivity.

OCM under unsteady state operation

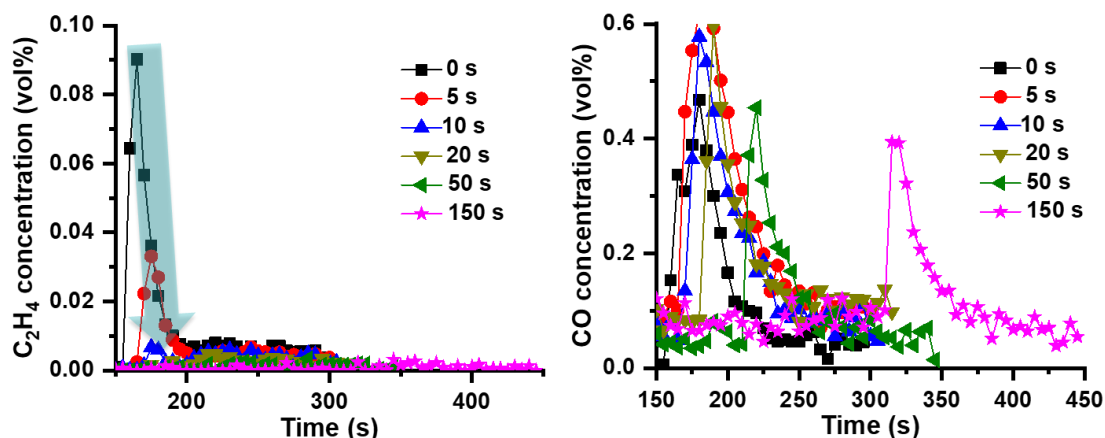


Figure 4.4 C₂H₄ and CO concentration in Y phase during OCM under XYF mode on La₂O₃ at 850 °C with the length of F phase varying from 0 s to 150 s.

Coke formation during Y phase was studied with the unsteady state operation of XYF mode. Figure 4.5 displays the amount of coke formed at different temperatures with the length of Y phase at 50 s, 150 s and 250 s on MgO and La₂O₃. For the two catalysts, the coke increases with extending the length of Y phase. This increase is gradually enhanced with the rise of the temperature for La₂O₃. While it follows similar trend until 800 °C when the increase is largely enhanced for MgO. This confirms that only one temperature-dependent active oxygen species contributes to CH₄ activation on La₂O₃, while a new type of active sites, lattice oxygen, is activated at 800 °C on MgO. The higher amount of coke at low temperature (≤ 750 °C) formed on La₂O₃ is in accordance with the higher activity of La₂O₃ towards CH₄ activation comparing to that of MgO.

OCM under unsteady state operation

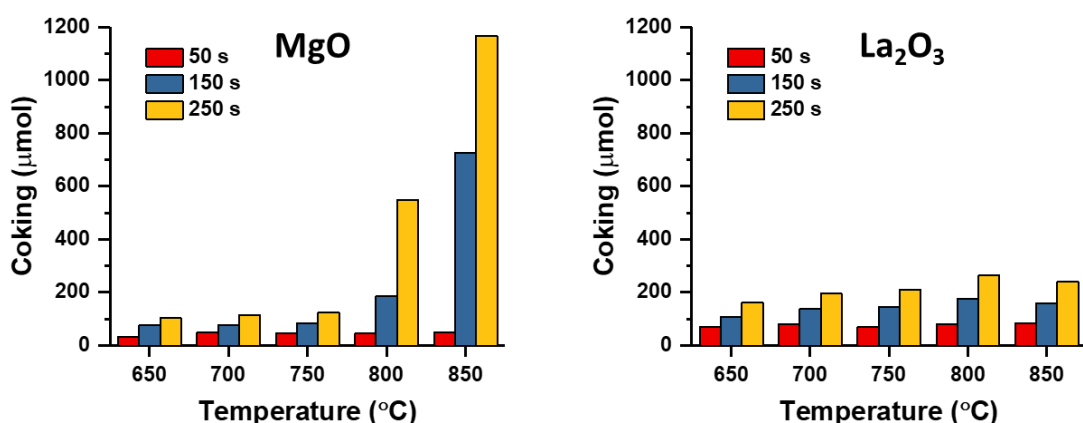


Figure 4.5 Coke amount with CH₄ exposure at different time (50 s, 150 s, 250 s) on La₂O₃ and MgO at different temperatures.

During the coke study, the catalyst bed was monitored with an USB camera. Interestingly, the visible coke (the dark area) starts to appear at the front of catalyst bed of MgO, but at the end of catalyst bed of La₂O₃ in Y phase as shown in Figure 4.6. Since La₂O₃ has stronger basicity than MgO¹⁷, the coke on MgO is mostly polymerized and cracked hydrocarbons with richer hydrogen than that on La₂O₃¹⁸. This is in line with the darker colour of the coke on La₂O₃, also reflects the strong ability of active oxygen species to cleave C-H bond on La₂O₃. However, to explain the different appearing position of the coke on the two catalysts beds, further studying is needed.

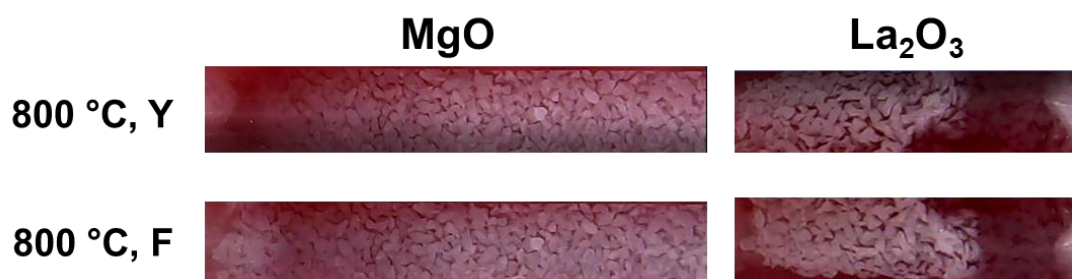


Figure 4.6 Photographs of catalyst bed of MgO and La₂O₃ at the end of Y phase during XYF with 250 s Y phase at 750 °C, 800 °C, and at the end of F phase

OCM under unsteady state operation

(150 s) in the same mode at 800 °C. The pictures were taking during the measurement of the coke amount. The gas flow is from the left to the right.

Besides, the visible coke on the catalyst bed can be partly removed in F phase when pure He was flowing in the reactor (Figure 4.6). This phenomenon is more distinct on MgO than on La₂O₃. Since the active oxygen species on the surface must be consumed for the coke formation where the catalyst bed is covered by the visible coke, the removal of the visible coke can be only attributed to the lattice oxygen in the bulk or sub surface. This demonstrates the mobility of the lattice oxygen in the two metal oxides, and the mobility of lattice oxygen in MgO is higher than that in La₂O₃.

4.4 Conclusion

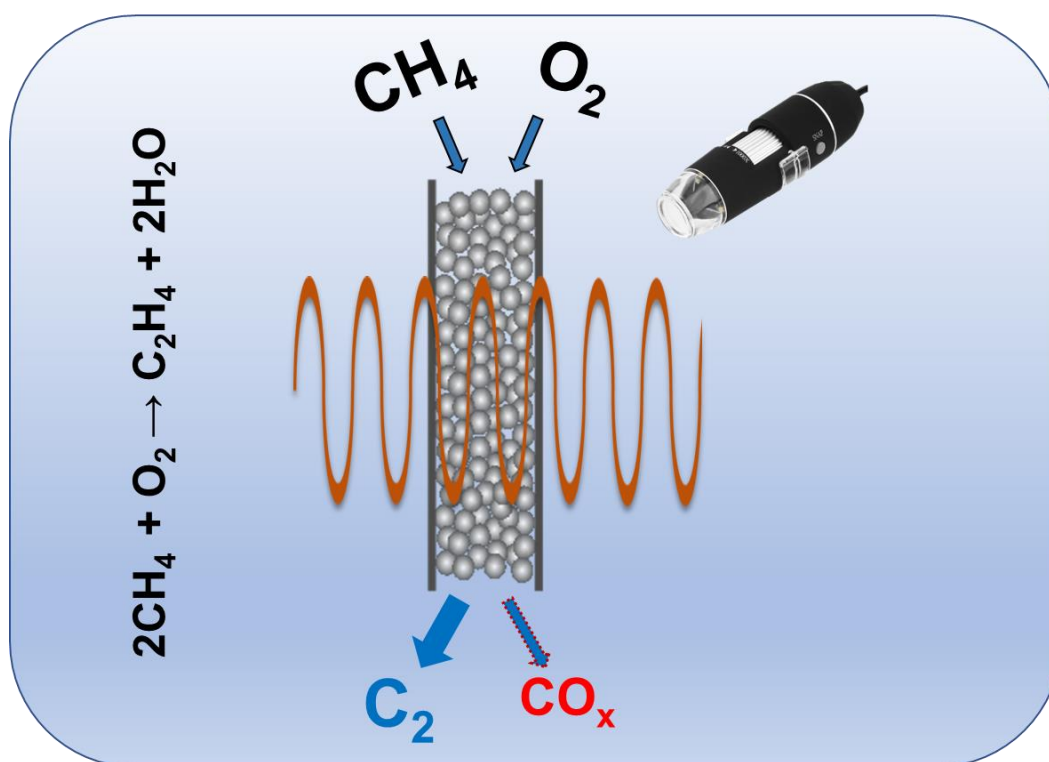
In this work, unsteady-state operation with different modes has been developed to identify and qualify the active sites on MgO and La₂O₃. Strongly adsorbed oxygen and lattice oxygen species are assigned to the active sites for CH₄ activation on MgO. The former can adsorb produced methyl and ethyl radical strongly, favouring CO formation. The latter shows good selectivity to C₂H₄ and is mainly activated at high temperature (≥ 800 °C). For La₂O₃, only one type of active oxygen species is detected, which has strong activity towards CH₄ activation but leads to mainly CO formation without the presence of gaseous O₂. In conclusion, MgO shows higher potential in chemical looping of oxidative coupling of methane.

Bibliography

1. P. F. Nelson, C. A. Lukey and N. W. Cant, *J. Phys. Chem-us*, 1988, **92**, 6176-6179.
2. P. F. Nelson, C. A. Lukey and N. W. Cant, *J. Catal.*, 1989, **120**, 216-230.
3. K. D. Campbell, E. Morales and J. H. Lunsford, *J. Am. Chem. Soc.*, 1987, **109**, 7900-7901.
4. E. Heracleous and A. A. Lemonidou, *Applied Catalysis A: General*, 2004, **269**, 123-135.
5. S. Lacombe, C. Geantet and C. Mirodatos, *Journal of Catalysis*, 1995, **151**, 439-452.
6. S. Lacombe, Z. Durjanova, L. Mleczko and C. Mirodatos, *Chemical Engineering & Technology*, 1995, **18**, 216-223.
7. C. K. Westbrook and F. Dryer, *Chemical Kinetic Modeling of Hydrocarbon Combustion*, 1984.
8. J. C. Mackie, *Catalysis Reviews*, 1991, **33**, 169-240.
9. E. P. J. Mallens, J. H. B. J. Hoebink and G. B. Marin, *J. Catal.*, 1996, **160**, 222-234.
10. K. P. Peil, J. G. Goodwin and G. Marcelin, *J. Catal.*, 1991, **131**, 143-155.
11. H. Borchert and M. Baerns, *J. Catal.*, 1997, **168**, 315-320.
12. I. Kim, G. Lee, H. B. Na, J.-M. Ha and J. C. Jung, *Molecular Catalysis*, 2017, **435**, 13-23.
13. V. Fleischer, R. Steuer, S. Parishan and R. Schomäcker, *J. Catal.*, 2016, **341**, 91-103.
14. Z. Cheng, D. S. Baser, S. G. Nadgouda, L. Qin, J. A. Fan and L.-S. Fan, *ACS Energy Letters*, 2018, **3**, 1730-1736.
15. B. Beck, V. Fleischer, S. Arndt, M. G. Hevia, A. Urakawa, P. Hugo and R. Schomäcker, *Catalysis Today*, 2014, **228**, 212-218.
16. V. Fleischer, P. Littlewood, S. Parishan and R. Schomäcker, *Chem. Eng. J.*, 2016, **306**, 646-654.
17. Q. Li, W. Zhang, N. Zhao, W. Wei and Y. Sun, *Catalysis Today*, 2006, **115**, 111-116.
18. O. Muraza and A. Galadima, *International Journal of Energy Research*, 2015, **39**, 1196-1216.

5 MICROWAVE-ASSISTED OXIDATIVE COUPLING OF METHANE

The effect of heating methods on oxidative coupling of methane reaction



5.1 Introduction

Oxidative coupling of methane (OCM) reaction has been considered as a promising route to functionalize methane, the predominant component in natural gas and/or shale gas¹. The desired product of OCM, ethylene, is the precursor for producing a wide range of chemical products, such as plastics, ethylene oxide and ethylbenzene²⁻⁵. In consequence, this route enables the relatively abundant natural gas and/or shale gas to become an alternative feedstock for the modern chemical industry which currently relies mainly on crude oil¹.

Despite the huge attention researchers paid to OCM, its industrial application has not been implemented yet, due to the limited C₂ (ethane and ethylene) yield (less than 30%). This is limited by the reaction mechanism of OCM. As introduced in Chapter 1.2.2, ethylene formation in catalytic OCM proceeds in four steps: methyl radical generation on the catalyst surface (1), methyl radical coupling forming ethane in the gaseous phase (2), ethyl radical generation on the catalyst surface (3), ethylene formation from ethyl radical in the gaseous phase (4). Methyl and ethyl radicals can also react with gaseous O₂, producing CO and/or CO₂ decreasing C₂ products selectivity⁶⁻¹⁰. The high temperature of the gas phase exacerbates the unwanted CO and CO₂ formation reactions in the gas phase. One way to target this issue is to use microwave heating to replace the conventional furnace heating¹¹. The former can selectively heat up the solid catalyst rather than heat both the catalyst and the gas feeds like the latter. This is proved to be effective for reducing further oxidation of C₂ products in the gas phase¹¹. The study of applying microwave to catalytic dry reforming of methane also elucidates the reduction of secondary gas-phase reactions via microwave heating¹². At the same time, microwave heating is considered as an efficient method to shift the equilibrium to the desired products for some heterogeneous catalytic reactions¹³.

In previous reports, microwave-assisted reactor systems are commonly clumsy^{12, 14}, and unpractical for conducting flexible investigations such as implementing *operando* techniques. Herein, we customized a compact microwave system, which is open to incorporate with some analytic techniques such as microscopy. The microwave system was successfully integrated to our OCM reaction system. The study of the

Microwave-assisted oxidative coupling of methane

effect of microwave heating on OCM was performed with this microwave-assisted reactor system, using the catalysts reported in Chapter 3: MgO, Li/MgO and La₂O₃.

5.2 Experimental

For the reaction conducted using the furnace reactor, the preparation of the catalysts and the reaction system are exactly as described in Chapter 3. Herein, only the specific conditions for the reaction performed with microwave reactor are presented.

5.2.1 Catalyst preparation

MgO-SiC (1:1) and La₂O₃-SiC (2:1) were prepared by simply mixing MgO ($\geq 99\%$ trace metal basis, Sigma Aldrich) and La₂O₃ (99.99%, Alfa Aesar), respectively, with SiC (0.125 mm, Cats Import, Hoogvliet). The catalysts were pelleted, crushed and sieved to the size of 300-400 μm . Li-doped magnesium oxide (Li/MgO) was prepared as described in Chapter 3.

5.2.2 Catalytic reactions

The reaction setup uses the same gas controlling and on-line gas analysis components as those reported in Chapter 3. The difference is that a microwave cavity is adopted for heating up the quartz reactor, as shown in Figure 5.1. An USB camera is placed on the top of the cavity, monitoring the catalyst bed in situ through an open window. The temperature of the catalyst bed is controlled with the aid of an infrared temperature sensor through another open window at the side of the cavity.

Microwave-assisted oxidative coupling of methane

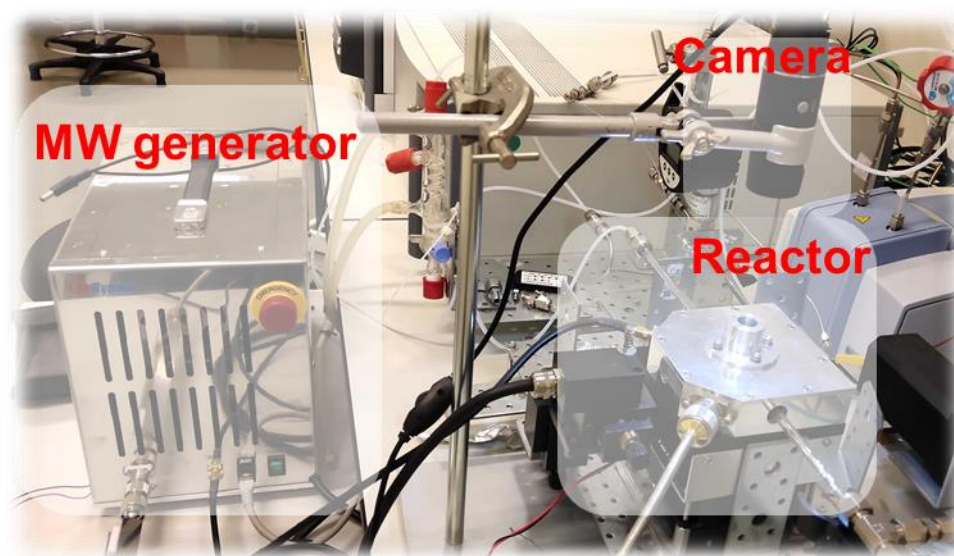


Figure 5.1 - Microwave reactor system

The sieved catalyst material was loaded into a quartz tube fixed with quartz wool. The length of the catalyst bed was fixed at 5 mm (100 mg for SiC, 56 mg for MgO-SiC and 59 mg for La₂O₃-SiC) and placed at the center of the microwave cavity. Then a mixture of 40% CH₄ (Abelló Linde), 10% O₂ (Abelló Linde), 13% N₂ and 37% He with a total flow rate of 80 mL/min was introduced into the reactor. The catalyst bed was heated up to the desired temperature. The outlet feed was analyzed by gas chromatography (GC, Agilent 7890B, equipped with two FID and one TCD) after passing through a mini water condenser cooled by water circulation.

5.3 Results and discussion

To apply microwave heating to assisting catalytic OCM reaction, the microwave generator and cavity were customized with a portable size, a light cooling jacket attached to the bottom of the cavity and an open window on the top of the cavity. The customized features allow its easy integration into the existing reactor system. and do not hinder the implementation of *operando* characterization techniques such as *operando* microscopy and spectroscopy.

5.3.1 Activation of customized microwave reactor for OCM reaction

To test the heating efficiency of our compact microwave reactor system, SiC was used since it exhibits microwave absorption. The experiment has shown that SiC can be heated up to 900 °C within 2 min with less than 100 W power input. The temperature

Microwave-assisted oxidative coupling of methane

drops rapidly once applied power is stopped. This proves the high heating efficiency of the microwave cavity.

Comparing the catalytic behaviour of SiC during OCM reaction using the microwave reactor (MW) and the furnace reactor (FN) shown in Figure 5.2, both CH₄ conversion and C₂ yield are significantly enhanced at 850 °C and 900 °C, as well as C₂H₄/C₂H₆ ratio. This is in accordance with previous observations that microwave heating improves OCM activity^{11, 15}. Since SiC is considered as an inert material for OCM reaction, the enhancement of OCM activity can be only ascribed to the unique feature of microwave heating: the catalyst is hotter than the reactor wall, resulting in quenching of the formed products, inhibiting their further oxidation, which is also mentioned in previous report¹⁶.

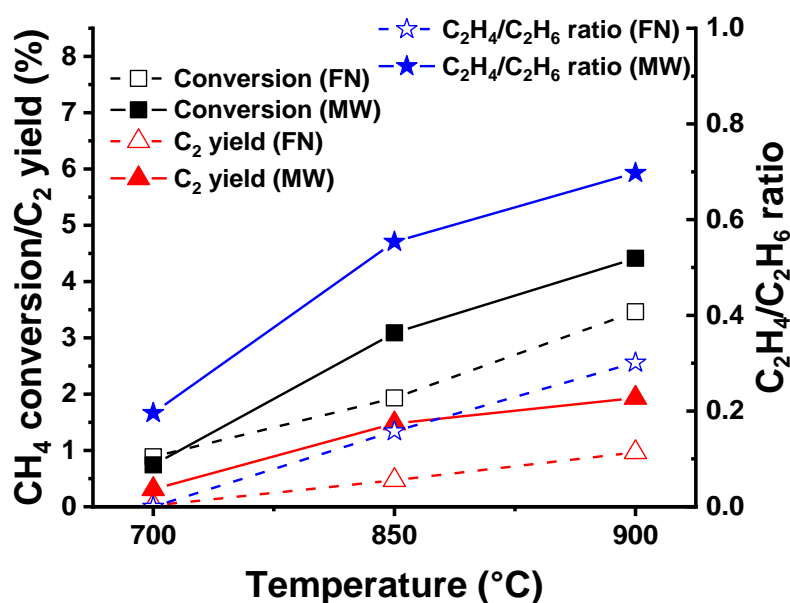


Figure 5.2 - CH₄ conversion, C₂ yield and C₂H₄/C₂H₆ ratio during OCM on SiC with furnace reactor (open symbols) and microwave reactor (solid symbols) at 700 °C, 850 °C and 900 °C.

5.3.2 The effect of microwave heating on MgO-based catalysts for OCM reaction

How does microwave heating affect the catalytic OCM behaviour with an active catalyst present? To answer this question, the simple metal oxide, MgO, having been studied in our previous work, was tested first. Due to the microwave inertness of the material, MgO powder was mixed with SiC in a weight ratio of 1:1, named as MgO-SiC, which can be heated up to maximum 550 °C. Within the investigated temperature range, both CH₄ conversion and C₂ selectivity increases with temperature rise (Figure 5.3). According to the results obtained with the furnace reactor in Chapter 3, increasing temperature can promote both CH₄ conversion and C₂ selectivity. In comparison, microwave heating notably lowers down the reaction temperature and lifts up C₂ selectivity for achieving similar CH₄ conversion. This proves that microwave heating improves the activity of MgO towards OCM and the improvement is not equivalent to the effect of simply increasing the reaction temperature.

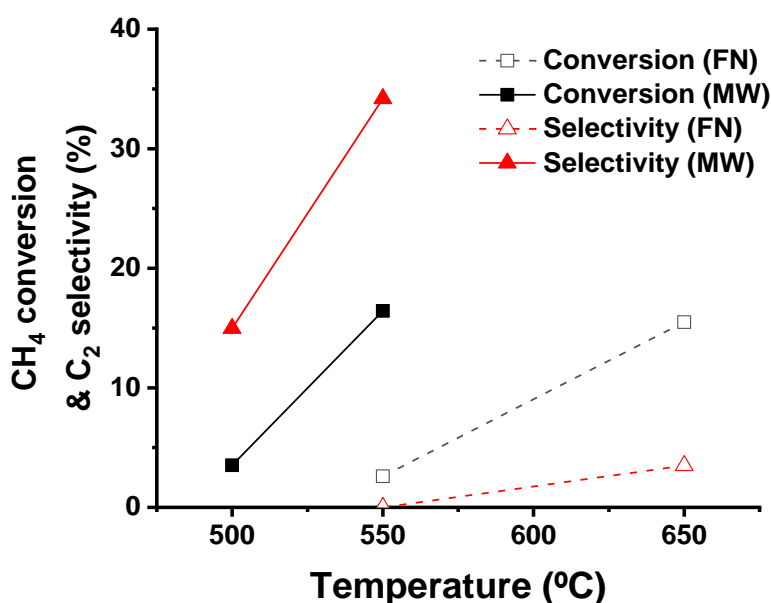


Figure 5.3 - CH₄ conversion, C₂ yield and C₂H₄/C₂H₆ ratio during OCM with furnace heating (FN, open symbols) and microwave heating (MW, solid symbols) for the reactor at different temperatures on MgO-based catalyst; MgO and MgO-SiC were used for furnace reactor and microwave reactor respectively.

Microwave-assisted oxidative coupling of methane

A lower temperature required for equivalent CH₄ conversion in the furnace reactor and the microwave reactor was also observed for Li-doped MgO (Li/MgO, Figure 5.4), which is active for microwave heating. The difference from MgO-SiC is that C₂ selectivity decreases at higher CH₄ conversion with temperature rise. This is also opposite to the C₂ selectivity trend using the furnace reactor, indicating the specific microwave effect on Li/MgO during OCM.

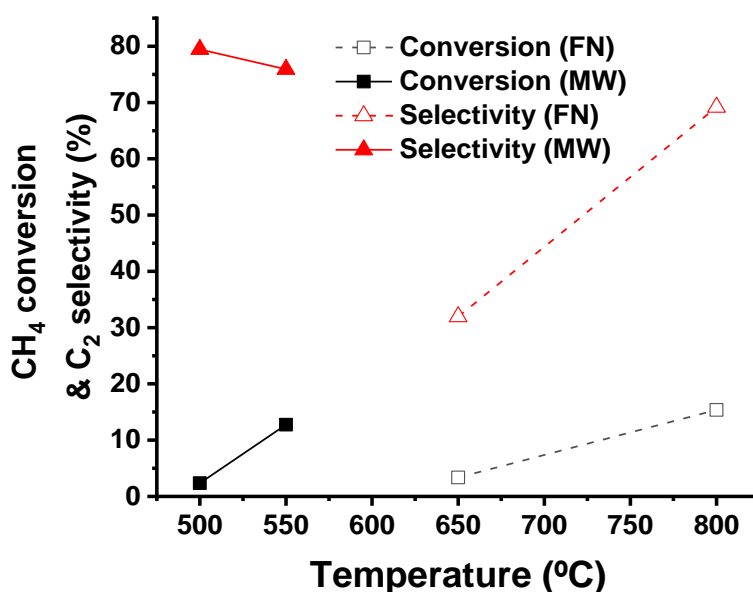


Figure 5.4 - CH₄ conversion and C₂ yield during OCM on Li/MgO with furnace reactor (solid symbols) and microwave reactor (open symbols) at different temperatures.

Comparing the photographs of Li/MgO catalyst bed before and after OCM reaction at 550 °C (the red colour is the focusing light from the infrared temperature sensor), it is found that Li/MgO looks melted during OCM and the ‘melted’ catalyst even corrodes the wall of the quartz reactor tube (Figure 5.5). This phenomenon starts to happen when the reaction temperature reaches 800 °C in the furnace reactor. Chen et al. pointed out that there is a huge temperature gradient in the catalyst bed when using microwave heating, a ‘hot spot’ can be generated on point defects or a weak surface bond whose temperature is much higher than the normalized catalyst bed temperature indicated by the equipped temperature sensor¹⁷. A similar conclusion is reported by another group¹³. Hence, the unique catalytic behaviour of Li/MgO under microwave heating is attributed to the nonuniform thermal effect. To study that, a precise spatial temperature analysis tool suitable for microwave heating is of high importance.

Microwave-assisted oxidative coupling of methane

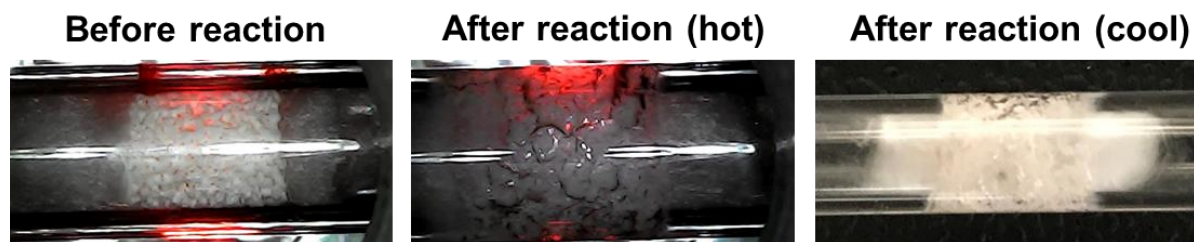


Figure 5.5 Pictures of Li/MgO catalyst bed before OCM reaction (left), just stopping OCM reaction at 550 °C (middle) which is still hot, and after the spent catalyst cooling down to ambient temperature (right). The gas flow is from the left to the right of the reactor tube..

5.3.3 The effect of microwave heating on La₂O₃-based catalysts for OCM reaction

La₂O₃ was also tested under OCM condition in microwave reactor. Similar to MgO, it is mixed with SiC (named as La₂O₃-SiC), but in a weight ratio of 2:1, to make the catalyst sensitive to microwaves, which enables the catalyst to reach 800 °C in the microwave reactor. Figure 5.6 compares the catalytic performance of the La₂O₃-based catalyst in the microwave reactor and the furnace reactor in the range of 500 °C to 800 °C. Microwave heating shows distinct advantages in low temperature range (< 700 °C) giving much higher CH₄ conversion and C₂ yield compared to those obtained with the furnace reactor. It is also found that C₂ yield is higher with the microwave reactor than with the furnace reactor at equivalent CH₄ conversion. Therefore, the preference towards C₂ product formation when microwave heating is used for OCM reaction in this temperature range is also proved on La₂O₃-based catalyst. This is originated from the selective heating for the catalyst which inhibits further oxidation of hydrocarbons in the gas phase.

However, in the high temperature range (≥ 700 °C), CO and H₂ formation increases rapidly in the microwave reactor, competing for O₂ with OCM reaction, resulting in the loss of CH₄ conversion and especially C₂ yield for the La₂O₃-based catalyst. As discussed in Chapter 3, the CO and H₂ formation coming from partial oxidation of CH₄ in low temperature range (< 700 °C) in the furnace reactor is superiority of La₂O₃ compared to MgO, since the exothermic partial oxidation contributes to hotspot formation at the front of the catalyst bed, finally enhancing OCM reaction. Obviously,

Microwave-assisted oxidative coupling of methane

the preference for CO and H₂ formation in the microwave reactor in the high temperature range is the unfavourable case, which is detrimental to OCM. In the photograph of the catalyst bed taken during OCM reaction at 750 °C with microwave heating (Figure 5.7), the formation of a hotspot is also observed, but it appears in the middle of the catalyst bed rather than at the front of catalyst bed, as observed in the case of furnace heating. Furthermore, heavy coking was also observed in the middle of the catalyst bed after OCM reaction (Figure 5.7). Since CH₄ decomposition is endothermic and favoured at high temperature conditions, it confirms that the temperature of the middle part of the catalyst is higher than its surrounding parts. Dry reforming or steam reforming of hydrocarbons producing CO and H₂ is also favoured in the high temperature region. This explains the extremely high CO and H₂ formation with the microwave reactor. These endothermic side reactions decrease the advantage of microwave heating for OCM reaction in the high temperature range in terms of CH₄ conversion and C₂ yield.

Microwave-assisted oxidative coupling of methane

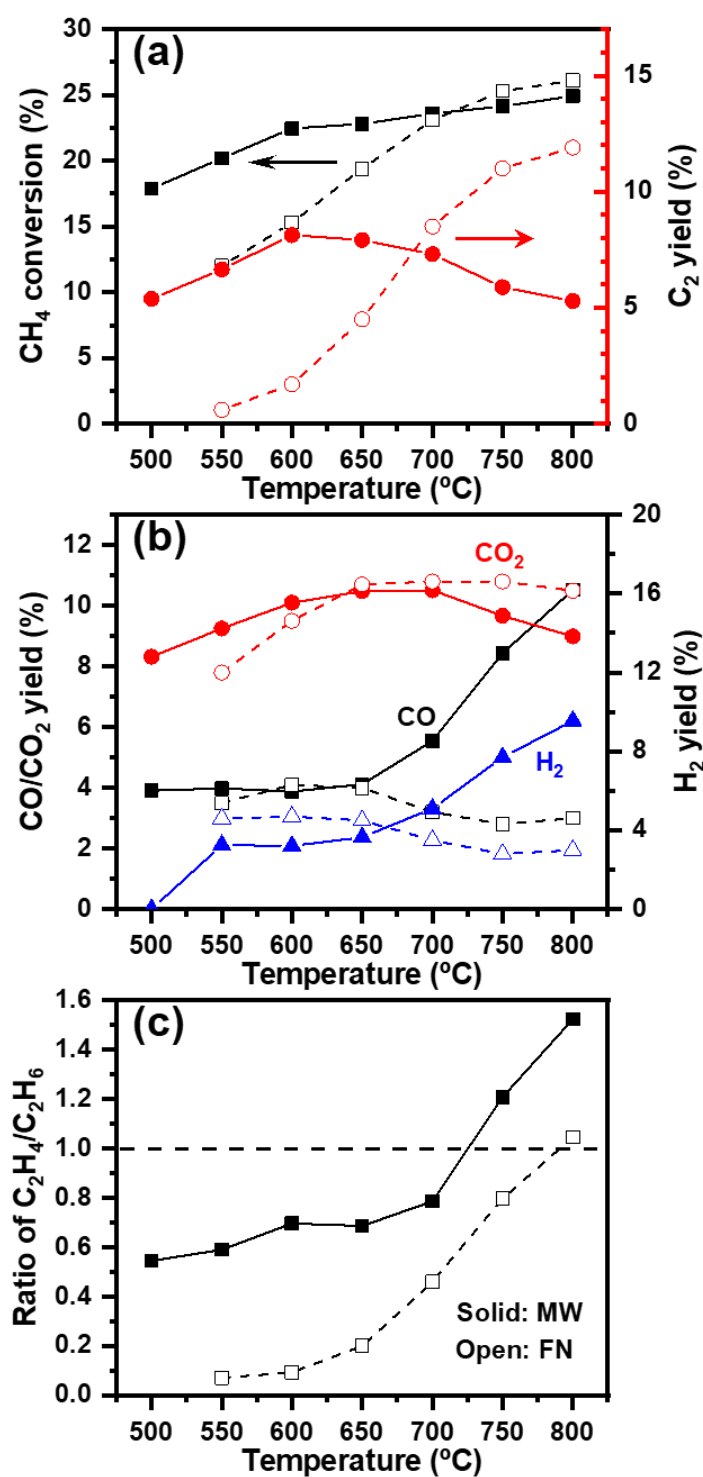


Figure 5.6 - CH₄ conversion, C₂ yield and C₂H₄/C₂H₆ ratio during OCM with furnace heating (solid symbols) and microwave heating (open symbols) for the reactor at different temperatures on La₂O₃ based catalyst; La₂O₃ and La₂O₃-SiC were used for furnace reactor and microwave reactor respectively.

Microwave-assisted oxidative coupling of methane

For the whole investigated temperature range, a higher C_2H_4/C_2H_6 ratio is obtained in the microwave reactor compared to the furnace reactor (Figure 5.6c), indicating that microwave heating favours C_2H_6 dehydrogenation. C_2H_6 dehydrogenation requires higher activation energy comparing to C_2H_6 formation¹⁸. Hence, high temperature favours C_2H_4 formation, which is also confirmed by the increase of the C_2H_4/C_2H_6 ratio with temperature rise. Hence, the hotspots inside the catalyst bed caused by microwave heating can contribute to the high C_2H_4/C_2H_6 ratio. Besides, C_2H_4 formation requires two radical generation steps (methyl radical and ethyl radical generation), which are mainly initialized on the catalyst surface, according to the reaction mechanism of OCM. From this point of view, the selective heating of catalyst also promotes C_2H_4 formation. Another explanation is that microwave heating leads to an effective 'quenching' of formed C_2H_4 , preventing its further oxidation in the gas phase, finally resulting in high C_2H_4/C_2H_6 ratio⁵.



Figure 5.7 Pictures of La_2O_3 -SiC catalyst bed before OCM reaction (left), during OCM reaction at 750 °C (middle), and after OCM reaction (right). The gas flow is from the left to the right of the reactor tube.

5.4 Conclusion

A portable and flexible microwave reactor was customized and successfully applied to OCM reaction. The effects of microwave heating on catalytic OCM reaction were studied using MgO-based and La_2O_3 -based catalysts. Due to the properties of material, the maximum temperature that the MgO-based catalyst could reach in microwave reactor was 550 °C and the maximum temperature the La_2O_3 -based catalyst could reach was 800 °C.

By comparing the catalytic performance of these catalysts using the microwave reactor and the conventional furnace reactor, the advantage of microwave heating on C_2 product selectivity was witnessed for all the investigated catalysts, at temperatures

Microwave-assisted oxidative coupling of methane

lower than 700 °C. This advantage is related to the selective heating of the catalysts by microwaves, which suppresses further oxidation of hydrocarbons in the gas phase, more than the thermal effect of the hotspot caused by the nonuniform microwave heating, originating from the nonuniformity of the catalyst material. However, microwave heating loses its superiority in the high temperature range (above 700 °C) for the La₂O₃-based catalyst, due to unfavourable endothermic reactions taking place in the hotspot zone in the middle part of the catalyst bed. In the whole studied temperature range, the C₂H₄/C₂H₆ ratio is promoted by microwave heating. This promotion can be related to the thermal effect of the hotspot, the radical-involving reaction mechanism of C₂H₄ formation or the 'quenching' effect on formed C₂H₄, due to the selective heating of the catalyst by microwave.

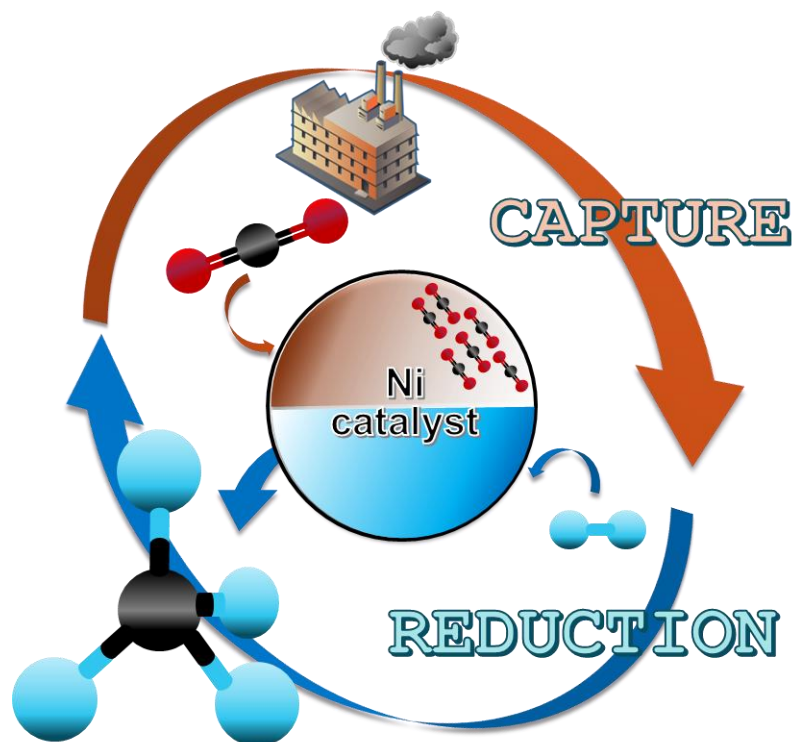
In conclusion, microwave heating is a potential solution for increasing C₂ product yield in OCM reaction. To make use of this advantage, one possible solution is to develop novel catalysts that are active both to microwave heating and OCM, enabling more efficient heating of the catalyst. Development of suitable spatial temperature analysis techniques for gas phase and solid phase under microwave conditions is also important for further unravelling the mechanism of the influence of microwave heating on catalytic OCM.

Bibliography

1. Y. Gambo, A. A. Jalil, S. Triwahyono and A. A. Abdulrasheed, *Journal of Industrial and Engineering Chemistry*, 2018, **59**, 218-229.
2. H. Soo, P.-Y. Chou and M. M. Bhasin, *Journal*, 1992.
3. D. K. Kim, *Journal*, 1999.
4. T. Xie, K. B. McAuley, J. C. C. Hsu and D. W. Bacon, *Industrial & Engineering Chemistry Research*, 1994, **33**, 449-479.
5. V. A. Bolotov, V. V. Chesnokov, Y. Y. Tanashev and V. N. Parmon, *Chemical Engineering and Processing - Process Intensification*, 2018, **129**, 103-108.
6. P. F. Nelson, C. A. Lukey and N. W. Cant, *J. Phys. Chem-us*, 1988, **92**, 6176-6179.
7. P. F. Nelson, C. A. Lukey and N. W. Cant, *J. Catal.*, 1989, **120**, 216-230.
8. K. D. Campbell, E. Morales and J. H. Lunsford, *J. Am. Chem. Soc.*, 1987, **109**, 7900-7901.
9. E. Heracleous and A. A. Lemonidou, *Applied Catalysis A: General*, 2004, **269**, 123-135.
10. L. Luo, R. You, Y. Liu, J. Yang, Y. Zhu, W. Wen, Y. Pan, F. Qi and W. Huang, *ACS Catalysis*, 2019, **9**, 2514-2520.
11. G. Roussy, J. M. Thiebaut, M. Souiri, E. Marchal, A. Kiennemann and G. Maire, *Catalysis Today*, 1994, **21**, 349-355.
12. L. S. Gangurde, G. S. J. Sturm, M. J. Valero-Romero, R. Mallada, J. Santamaria, A. I. Stankiewicz and G. D. Stefanidis, *Chemical Engineering and Processing - Process Intensification*, 2018, **127**, 178-190.
13. X. Zhang and D. O. Hayward, *Inorg. Chim. Acta*, 2006, **359**, 3421-3433.
14. I. Julian, C. M. Pedersen, K. Achkasov, J. L. Hueso, H. L. Hellstern, H. Silva, R. Mallada, Z. J. Davis and J. Santamaria, *Catalysts*, 2019, **9**, 867.
15. W. Cho, Y. Baek, S.-K. Moon and Y. C. Kim, *Catalysis Today*, 2002, **74**, 207-223.
16. G. Roussy, E. Marchal, J. M. Thiebaut, A. Kiennemann and G. Maire, *Fuel Process. Technol.*, 1997, **50**, 261-274.
17. C. Chen, P. Hong, S. Dai and J. Kan, *J. Chem. Soc., Faraday Trans.*, 1995, **91**, 1179-1180.
18. K. Otsuka, K. Jinno and A. Morikawa, *J. Catal.*, 1986, **100**, 353-359.

6 CO₂ HYDROGENATION

Continuous CO₂ capture and reduction in one process: CO₂ methanation by unpromoted and promoted Ni/ZrO₂



6.1 Introduction

Fossil fuel, the main energy source of industry and modern human life, is a two-edged sword, bringing unparalleled convenience as well as enormous CO₂ emission. The latter is considered as the culprit for global warming and climate change. Current global strategies to tackle this problem are aligned along two directions: (i) carbon capture and storage (CCS), i.e. capture CO₂ and store it in the deep underground and (ii) carbon capture and utilization (CCU), i.e. capture CO₂ and utilize it, with particularly promising paths by converting it to other useful chemicals such as methanol and methane to close the carbon cycle¹⁻⁵. Despite the global efforts, risks and difficulties are known with the two approaches. Recent studies show that while CCS can store theoretically a vast amount of CO₂, there is a risk of releasing CO₂ back to the atmosphere⁶. Furthermore, for both CCS and CCU the common denominator is the CO₂ capture process, which is known to be costly and energy intensive⁷ since the industrial effluent for CO₂ capture contains low concentration CO₂ (3-13 vol%) with various other gases.

Based on this background, we recently developed a process combining CO₂ capture and catalytic reduction steps, so-called CO₂ capture and reduction (CCR) process. CCR is operated under isothermal, unsteady-state condition to induce the bifunctionality of catalyst. In the capture phase, CO₂ is chemically stored over catalyst and before/upon saturation the gas atmosphere is switched to reducing one like hydrogen (i.e. reduction phase) to convert the stored CO₂ into a targeted product. In our first studies, a catalyst containing Cu as the main active reduction sites and K as CO₂ capture sites was developed and CCR was demonstrated with >99% CO₂ capture efficiency with diluted CO₂ effluent streams even in the presence of oxygen and water and with high conversion efficiency to CO (in practice to syngas due to the presence of unconverted hydrogen) via reverse water-gas shift reaction (RWGS)^{8,9}.

Among CO₂ hydrogenation reactions, CO₂ methanation has recently attracted considerable interests as a path for CO₂ utilization as well as renewable energy storage¹⁰⁻¹². The major advantage of methane is that its transport infrastructure through pipelines is globally well established because it is the major component of the natural gas. This renders the molecule uniquely attractive for rapid and large-scale

implementation of synthetic natural gas synthesis, as often discussed in the context of the power-to-gas scenario.

Hence, in this work our efforts were directed to investigate the potential of the isothermal CCR approach for methanation reaction, particularly to understand the important components for efficient CO₂ capture and formation of methane. Among active metal components for CO₂ methanation, nickel was chosen for its widely recognized activity and its high natural abundance, whereas ZrO₂ was chosen as the support material for its good synergetic function in the reaction when used in conjunction with Ni. Besides K was added as promotor since it was found effective for CO₂ capture in our previous study, the use of La was also investigated for its distinct function to capture CO₂ under CCR conditions. Furthermore, the reaction mechanism and the roles of each components on the active surface species formed over the catalysts were studied in depth by *operando* space- and time-resolved diffuse reflectance infrared Fourier transform spectroscopy (DRIFTS).

6.2 Experimental

6.2.1 Materials and catalyst preparation

Nickel nitrate hexahydrate (>98%, Alfa Aesar), potassium carbonate (>99%, Acros), lanthanum nitrate hexahydrate (>99.9%, Alfa Aesar), zirconium oxide (Alfa Aesar, 90 m²/g) were used as received. All catalyst materials were synthesized by the incipient wetness impregnation method. Ni/ZrO₂ (15/85 wt%, NZ) and Ni-La/ZrO₂ (15/5/80 wt%, NLZ) were prepared by (co)impregnating the aqueous solution of the corresponding nitrate salts onto ZrO₂ (Alfa Aesar, 90 m²/g). For Ni-K/ZrO₂ (15/5/80 wt%, NKZ), firstly nickel nitrate was impregnated on ZrO₂, dried overnight at 80 °C and then calcined at 500 °C for 5 h. Subsequently, the aqueous solution of K₂CO₃ was impregnated on Ni/ZrO₂. After the impregnation step, all samples were dried overnight at 80 °C and then calcined at 500 °C for 5 h.

6.2.2 Catalyst characterization

Power X-ray diffraction (PXRD) was performed on D8 Advanced Powder Diffractometer (Bruker) equipped with a vertical 2theta-theta goniometer in transmission configuration, with a K α_1 germanium monochromator for Cu radiation ($\lambda=1.5406$ Å), at a scan step of 0.02°/s from 10° to 80°.

H₂ temperature programmed reduction (H₂-TPR) was performed on TPDRO 1100 (Thermo Fisher Scientific) equipped with a TCD detector. 50 mg of catalyst material was pretreated at 300 °C for 30 min under N₂ flow (30 mL/min) and the sample was cooled to 30 °C under N₂. Then the gas atmosphere was changed to 5 vol% H₂ in N₂ at 30 mL/min. The sample temperature was raised from 30 to 800 °C at the ramp rate of 10 °C/min and H₂ consumption was monitored by the TCD detector. Soda lime (CaO+Na₂O) trap was used to adsorb mainly H₂O and CO₂.

Reductive CO₂ temperature programmed desorption in H₂ atmosphere (termed as “CO₂-TPD with H₂”) was conducted on TPDRO 1100. 20 mg of catalyst material was placed in the quartz tube, reduced at 450 °C for 2 h, then degassed in He for 30 min at 50 °C, followed by CO₂ (4 vol% in He) saturation for 1 h and He flushing for 30 min at same temperature. Subsequently, reductive CO₂-TPD with H₂ was performed in H₂ (5 vol% in N₂ at 20 mL/min) by ramping from 50 to 700 °C at the rate of 10 °C/min. The composition of the effluent gas during the ramping was identified by online mass spectrometer (Omnistar, Pfeiffer Vacuum).

6.2.3 Catalytic reaction

Catalysts were first pelleted, crushed and sieved to the size of 200-300 μm. 1 g of a catalyst material was charged into a stainless steel tube reactor, fixed with quartz wool and pre-reduced in pure H₂ (50 mL/min) at 450 °C for 1 h before reaction. Then the reactor was cooled down to the desired reaction temperature (250, 300, 350 or 450 °C) in He and the catalyst was evaluated under a CCR condition. During the CO₂ capture phase 4.7 vol% CO₂ (>99.9998%, Abelló Linde) in He and during the reduction phase pure H₂ (>99.999%, Abelló Linde), both at 50 mL/min for ca. 5 min for each phase, was alternately passed through the reactor at the ambient pressure. The flow sequence was controlled by a computer-controlled switching valve which was synchronized with the gas detection. Time-resolved quantitative gas analysis of CO₂, CO and CH₄ was performed using the transmission IR spectroscopy through the gas cell mounted in ALPHA FT-IR spectrometer (Bruker), giving a time-resolution of ca. 2.5 s. To improve the S/N of the detection, six CCR cycles were evaluated for each catalyst at a specific experimental condition and the concentration profiles were averaged into one CCR cycle after making sure that the profiles are reproducible.

6.2.4 Space- and time-resolved DRIFTS

Space- and time-resolved *operando* DRIFTS was performed using a reaction cell mimicking the action of a fixed-bed plug flow reactor, with a similar design to that reported previously¹³. The cell was mounted in a Praying Mantis (Harrick) optical accessory (Harrick) fixed in Vertex 70V FTIR spectrometer (Bruker). 200 mg catalyst sieved in 75–150 μm particle size was charged into the channel on the cell (2 x 2 mm² cross section) to form a catalyst bed with ca. 10 mm length and also fixed by quartz wool. Prior to DRIFTS measurement, catalyst was pre-reduced under pure H₂ with at 10 ml/min at 350 °C for 2 h. The catalyst was treated under a CCR condition at 350 °C with repeated CCR cycles (5 vol% CO₂ in He vs. pure H₂ at 10 mL/min) for ca. 12-15 h to activate and stabilize the catalyst for CCR. Then the catalyst was cooled down to a desired temperature (250, 300 or 350 °C) to perform DRIFTS under the CCR condition (each phase of ca. 200 s). 55 spectra were collected per phase at 4 cm⁻¹ resolution with a liquid N₂ cooled MCT detector at four positions along the axial direction of the catalyst bed (we call, Front, Middle 1, Middle 2 and Back). Each measurement was performed for 9 CCR cycles at each position of the catalyst bed and the last 7 or 8 cycles were averaged into one cycle for the detailed analysis. The composition of the effluent stream was analyzed by mass spectrometer (OmniStar, Pfeiffer Vacuum) and in the gas cell of the ALPHA IR spectrometer (Bruker) in a synchronized manner with the DRIFTS measurements.

6.3 Results and discussion

For the sake of more straightforward discussions on the catalyst structure-activity relationships, firstly catalytic performance is described, followed by *ex situ* and *in situ/operando* characterization of the catalysts and reactive surface species.

6.3.1 CCR performance of unpromoted and K- or La-promoted Ni/ZrO₂ catalysts

In this study, sufficiently long CO₂ capture and reduction periods were used to compare the performance of the catalyst materials investigated. In practice by shortening the periods, one can optimize the CCR process by avoiding the release of CO₂ and the waste of H₂, respectively⁸. It is important to match the duration of CO₂

capture and reduction periods for process intensification using a two-reactor system⁸. The aim of this work is to understand the roles of promoters in CCR and thus no process optimization was attempted.

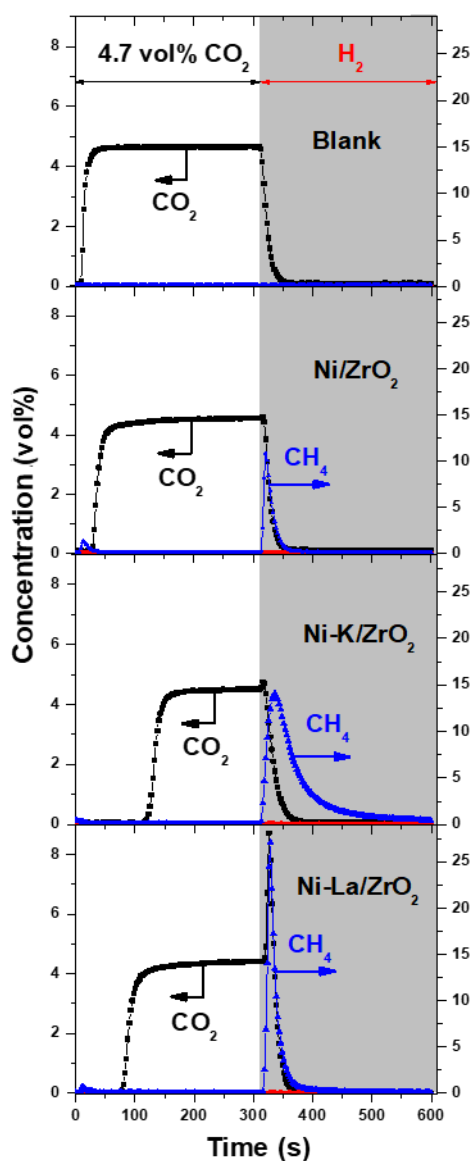


Figure 6.1 - Effluent concentration profiles of CO₂ (black) and reduction products, CH₄ (blue) and CO (red) during CO₂ capture (white area, 4.7vol% CO₂ in He, 50 mL min⁻¹) and reduction (grey area, pure H₂, 50 mL min⁻¹) processes over the three Ni-based catalysts at 350 °C and atmospheric pressure. Blank test was performed at room temperature without charging the reactor with catalyst.

Figure 6.1 shows representative CO₂, CH₄ and CO concentration profiles during CCR for Ni/ZrO₂ (NZ), Ni-K/ZrO₂ (NKZ) and Ni-La/ZrO₂ (NLZ) at 350 °C. For comparison the concentration profiles for the empty reactor at room temperature (Figure 6.1, top

panel, Blank) are also shown. At 350 °C mainly CH₄ was formed as the product and little CO was detected for all catalysts examined. The CH₄ selectivity (the rest is CO selectivity) was 89, 98, 99% for NZ, NKZ and NLZ, respectively. For comparison, we performed CO₂ hydrogenation under steady-state conditions (4 vol% CO₂ and 50% H₂ in He at 100 mL/min at atmospheric pressure) using the same catalysts (Supporting Information, Table 6.1). The major difference between the catalytic performance under steady- and unsteady- state operation is the function of K where selectivity to CO was notably increased under steady-state conditions (43 and 24% CO selectivity at 250 and 350 °C, respectively), while this was not the case under unsteady-state conditions where high selectivity (>90%) to CH₄ was achieved for NKZ. The steady-state activity is in agreement with the previous findings where potassium enhances CO selectivity of Ni catalysts by lowering the activation energy for CO formation^{14, 15}, indicating that the catalytic properties can be largely altered and distinct reactivity can arise by unsteady-state operation.

Table 6.1 - Catalytic performance of Ni/ZrO₂, Ni-K/ZrO₂ and Ni-La/ZrO₂ for steady-state CO₂ hydrogenation (4 vol% CO₂ and 50% H₂ in He at 100 mL/min at atmospheric pressure)

Catalyst (wt%)	CO ₂ conversion/%			CH ₄ selectivity/%		
	250 °C	350 °C	450 °C	250 °C	350 °C	450 °C
NZ(15/85)	13	86	99	100	99	99
NKZ(15/5/80)	12	50	86	57	76	95
NLZ(15/5/80)	58	100	97	95	100	98

Most strikingly, prominent effects of the K and La promoters on the dynamic CO₂ capture and reduction processes were evidenced. When K was used as promoter, the CO₂ capture efficiency (i.e. how much CO₂ was captured on the catalyst during the whole capture phase) was drastically increased from 11% (NZ) to 44% (NKZ) as evident from the full CO₂ capture for ca. 30 s for NZ and for ca. 120 s for NKZ. On the other hand, the La promoter was not as effective as K, and the CO₂ capture efficiency of NLZ was 32% (ca. 80 s full capture). In all cases, the increase in CO₂ concentration after saturation is rapid and steep. This concentration profile indicates highly active

and efficient CO₂ capture of these materials and this is one of the most important characteristics to be a CCR catalyst.

Very large differences were observed for CH₄ formation during the reduction phase. Due to the differences in the amount of captured CO₂, consequently the amount of CH₄ produced during the reduction phase was increased by 4-fold and 2-fold for NKZ and NLZ, respectively, in comparison to NZ. Also, the durations after CH₄ formation until 1 vol% CH₄ concentration was reached were comparable for NZ (ca. 40 s) and NLZ (ca. 60 s), whereas that for NKZ was significantly longer (170 s) as evident from the tailing concentration profile observed for NKZ (Figure 6.1). As mentioned earlier, the duration of the reduction time with respect to CO₂ capture duration is of paramount importance for process intensification. When two CCR reactors are used for continuous CO₂ capture by switching between the function of the two reactors, the durations for CO₂ capture and reduction should be matching. In case of NKZ, the reduction time is remarkably longer by ca. 50 s than full CO₂ capture duration under the condition evaluated. This means that the capture phase should be switched to the reduction phase much before full utilization of CO₂ capture capacity. In this regard, NLZ performs more suitably for CCR under the duration of ca. 60 s capture and reduction periods where the catalyst's capture capacity is more efficiently exploited and the duration is sufficient for regeneration for the subsequent CO₂ capture. This shorter reduction period implies also more efficient use of H₂ by minimizing the release of unreacted H₂ in the effluent. Nevertheless, it should be noted that the CO₂ capture capacity and reduction duration vary significantly by the reaction conditions such as temperature and space velocity and they should be optimized for a promising catalyst for practical applications.

Another important observation was the release of unreacted CO₂ during the reduction phase (Figure 6.1). The larger amount of CO₂ release for NLZ is evident from Figure 6.1. The amounts of unreacted, released CO₂ in the reduction phase with respect to those captured (the amount of CO₂ present in the effluent stream of the blank case was subtracted) were 14% (NZ), 7% (NKZ) and 21% (NLZ). This means that about 80% of captured CO₂ was converted to CH₄ and the rest was released as CO₂ for NLZ. The coverage of hydrogen atoms over Ni is known to restrain CO₂ adsorption¹⁶ and the differences may stem from unique interactions between hydrogen and CO₂ with Ni for the three catalysts. However, *operando* DRIFTS studies to be presented later

indicate the differences of CO₂ release among the three catalysts likely reflect the material-dependent mechanism of CO₂ capture over the catalyst surfaces.

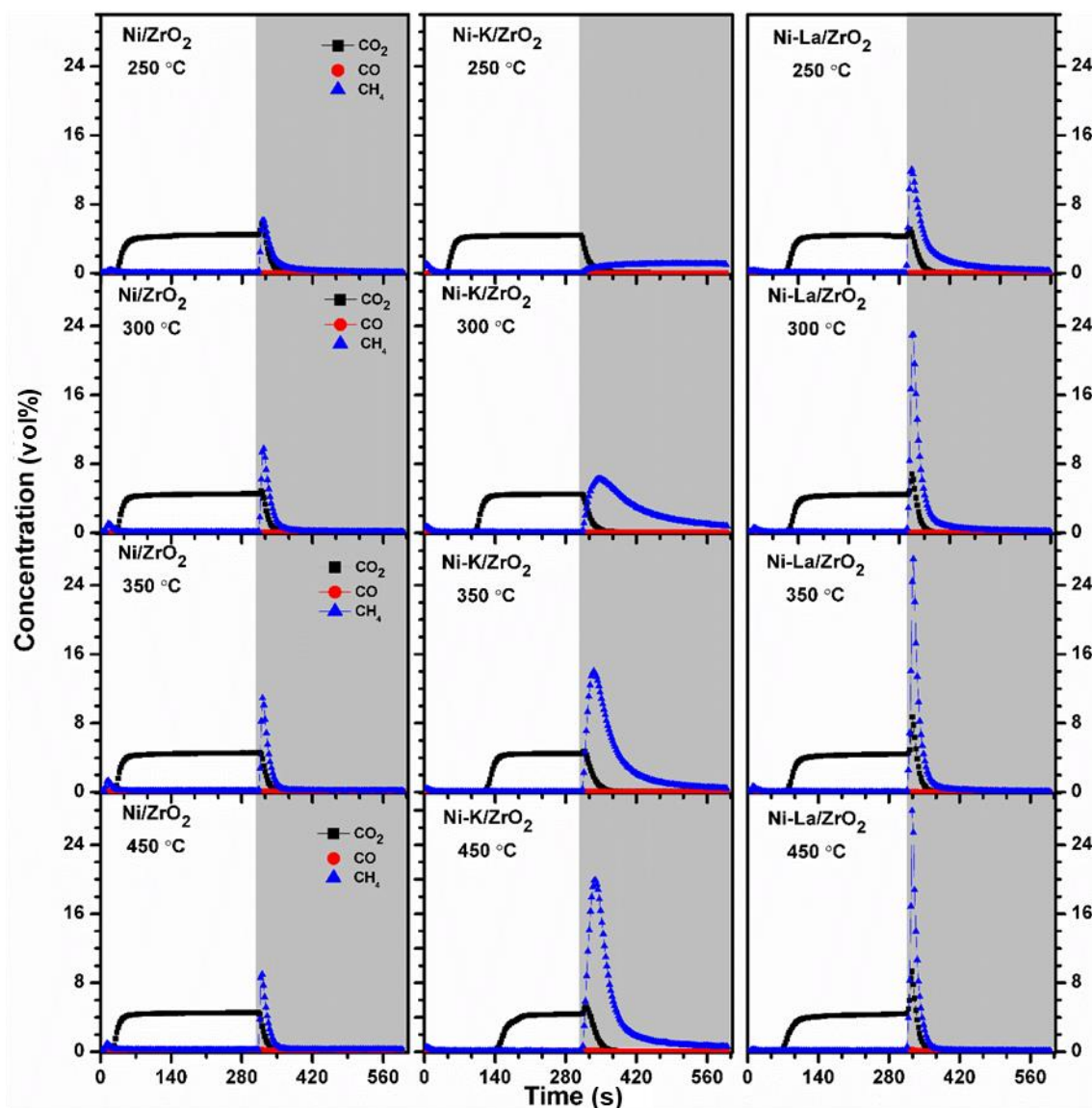


Figure 6.2 - Concentration profiles of CO₂ and reduction products (CH₄ and CO) during CO₂ capture (white area, 4.7 vol% CO₂ in He, 50 mL min⁻¹) and reduction (grey area, pure H₂, 50 mL min⁻¹) processes over the three Ni-based catalysts at different temperatures and atmospheric pressure.

Furthermore, the CCR performance of the three catalysts was evaluated in the range of 250-450 °C and the results are summarized in Figure 6.3 (the CCR profiles are presented in Figure 6.2). As mentioned earlier, the values are highly condition-dependent; therefore they are for indicative and comparative purposes only. NZ displayed the poorest catalytic performance among the three with lowest CO₂

conversion and a significant decrease of CH₄ selectivity from 96 to 73% as the temperature was increased from 250 to 450 °C, while the CO₂ conversion remained almost constant at 20%. Upon K-promotion (NKZ), both CO₂ conversion as well as CH₄ selectivity have improved drastically. Remarkably the selectivity to CH₄ was >95% in the temperature range, while CO₂ conversion was highly temperature dependent as the function of K for CO₂ capture is greatly enhanced up to ca. 60% at 450 °C (Figure 6.3). NLZ, on the other hand, presented also high CH₄ selectivity (>90%), notably with almost constant CO₂ conversion (ca. 35%) in the temperature range. The latter seems decreased slightly at higher temperatures (Figure 6.3) and this is attributed to the enhanced release of unreacted CO₂ during the reduction phase at higher temperatures (Figure 6.2). Depending on the determining factor of a process (e.g. CO₂ capture capacity, faster reduction duration and operation temperature), one can choose more suitable catalyst composition; NKZ for high temperature operation while NLZ for low or varying temperature operation.

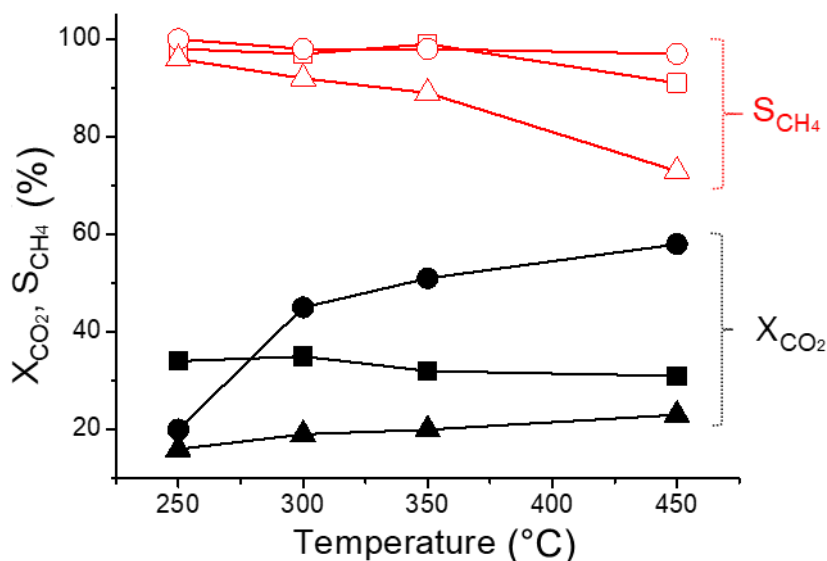


Figure 6.3 - CO₂ conversion and CH₄ selectivity for Ni/ZrO₂ (triangle), Ni-K/ZrO₂ (circle) and Ni-La/ZrO₂ (square) at different temperatures under the CCR operation (4.7% CO₂ in He vs. H₂ at 50 mL/min).

6.3.2 Catalyst characterization

The structure of the three catalysts before (labelled as fresh) and after the CCR (labelled as spent) was studied by X-ray diffraction (Figure 6.4). Most reflections present in the XRD patterns belong to monoclinic ZrO₂ (JCPDS: 00-036-0420). The only difference engendered by the reaction is that nickel oxide (JCPDS: 00-047-1049) in the fresh catalysts is reduced to the metallic form (JCPDS: 01-087-0712). This is reasonable since the reaction was stopped after reduction phase. La and K, which are expected to exist as La₂O₃ and K₂CO₃, respectively, based on synthesis condition were not detectable by XRD. Considering the rather high loading of the two components (5 wt%), the results indicate high dispersion of these species as nanocrystallites or in amorphous phase, which may be responsible for the prominent promoter effects observed in CCR.

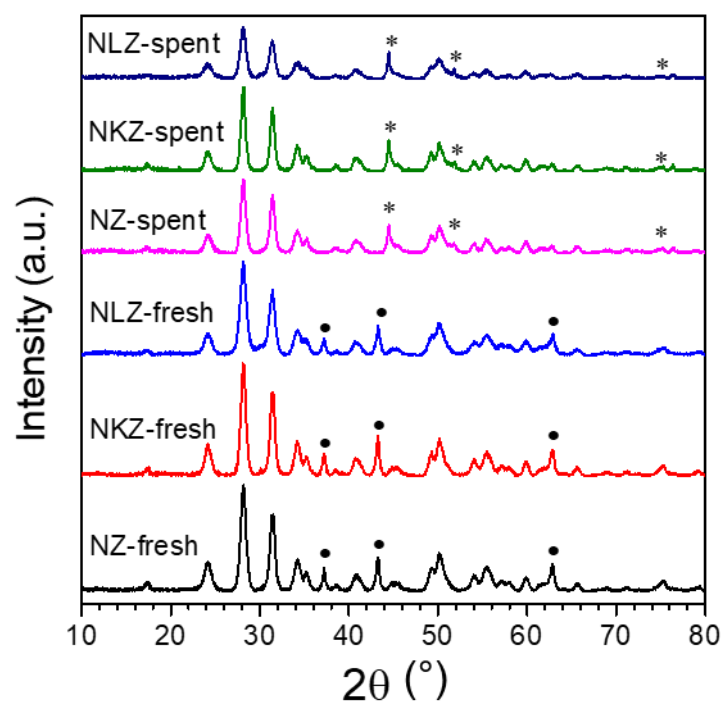


Figure 6.4 - XRD patterns of Ni/ZrO₂ (NZ), Ni-K/ZrO₂ (NKZ) and Ni-La/ZrO₂ (NLZ) before (“fresh”) and after (“spent”) the CCR. (•) nickel (II) oxide and (*) metallic nickel.

Figure 6.5 shows the H₂-TPR results of the three catalysts. For all materials, an agglomerated broad reduction peak starting at ca. 300 °C with characteristic peak shapes and completion temperature of reduction was observed. The reducibility of Ni is similar for NZ and NKZ, with some differences in the presence of high temperature

peaks for NKZ. The reduction profile of NLZ is markedly different from those of the other two catalysts, exhibiting a sharp peak at ca. 350 °C. According to literatures, the reduction peak at low temperature is related to relatively free NiO which has higher reducibility while the one at high temperature is assigned to reduction of complex NiO_x species due to the metal-support interactions^{17, 18}. Based on this interpretation, we can conclude that the metal-support interactions between Ni and ZrO₂ are similar for NZ and NKZ, whereas they can be largely altered by the La-promotion, leading to enhanced reducibility of NiO. The excellent catalytic activity of NLZ at low temperature may be due to the high reducibility of Ni, thus attaining high conversion efficiency of captured CO₂ and high selectivity to CH₄.

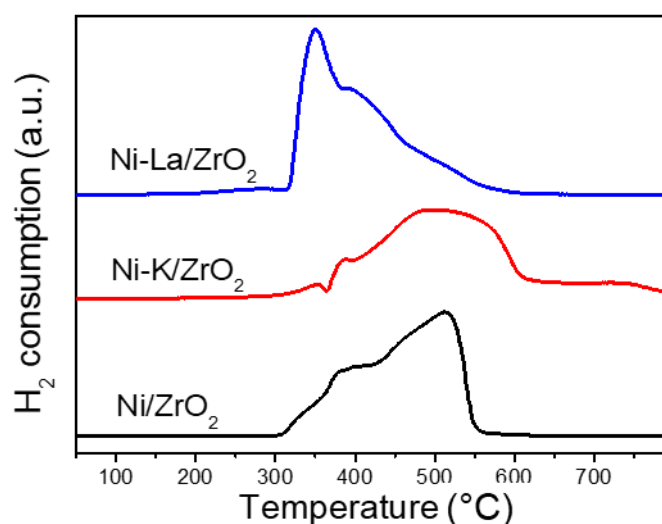


Figure 6.5 - H₂-TPR profiles of Ni/ZrO₂, Ni-K/ZrO₂ and Ni-La/ZrO₂.

To understand better the temperature-dependent catalytic activity and CCR properties of the catalysts, reactive (reductive) CO₂-TPD in the presence of 5 vol% H₂ was performed with simultaneous analysis of released gaseous products by mass spectrometry (MS). Figure 6.6 (top panel) shows the TCD signal of the temperature-programmed experiments. All catalysts presented three main peaks with largely different desorption/formation characteristics, and the MS profiles (Figure 6.6, lower three panels) clarifies the origin of the peaks.

Interestingly the first peak observed for all catalysts is due to an uptake of H₂ taking place at ca. 100-150 °C without H₂O formation (not shown). In case of NLZ and NKZ, these peaks are overlapped with another broad one due to CO₂ desorption as

supported by the MS profiles. This CO₂ desorption was not observed for NZ and this originates from the presence of the K/La promoter.

At slightly above 200 °C, NZ and more prominently NLZ showed another peak due to CH₄ formation. In contrast, for NKZ the formation of CH₄ was observed starting at 300 °C in a wider temperature range, indicating the higher stability of the surface species formed by CO₂ capture on NKZ. The sharpness of the CH₄ peak of NLZ compared to NKZ is in accordance with the faster reduction time observed in CCR (Figure 6.1). It is worth pointing out that the CH₄ peak was observed at lower temperature for NLZ compared to NZ, which is in accordance with the H₂-TPR results, showing the higher reducibility of NLZ than NZ. Besides, there is another peak due to CH₄ formation at even higher temperature (>500 °C) for all catalysts. The amount of CH₄ formed at this high temperature was minor compared to the former one. Surprisingly, there was a formation of CO observed only for NKZ. Only small portion of CH₄ formed for NZ and NLZ, but a large amount of CO formed for NKZ starting its formation at 550 °C and ending at 800 °C. This is likely due to a highly stable potassium carbonate species, which was reduced to CO by H₂. This result indicates that some portion of K components may be present as stable carbonates and do not participate in the reaction during CCR and that NKZ likely exhibits much lower CH₄ selectivity at >500 °C due to more favorable CO formation. The results are in full accordance with the high temperature dependence of the CCR performance of NKZ and the independence and low temperature CCR activity of NLZ.

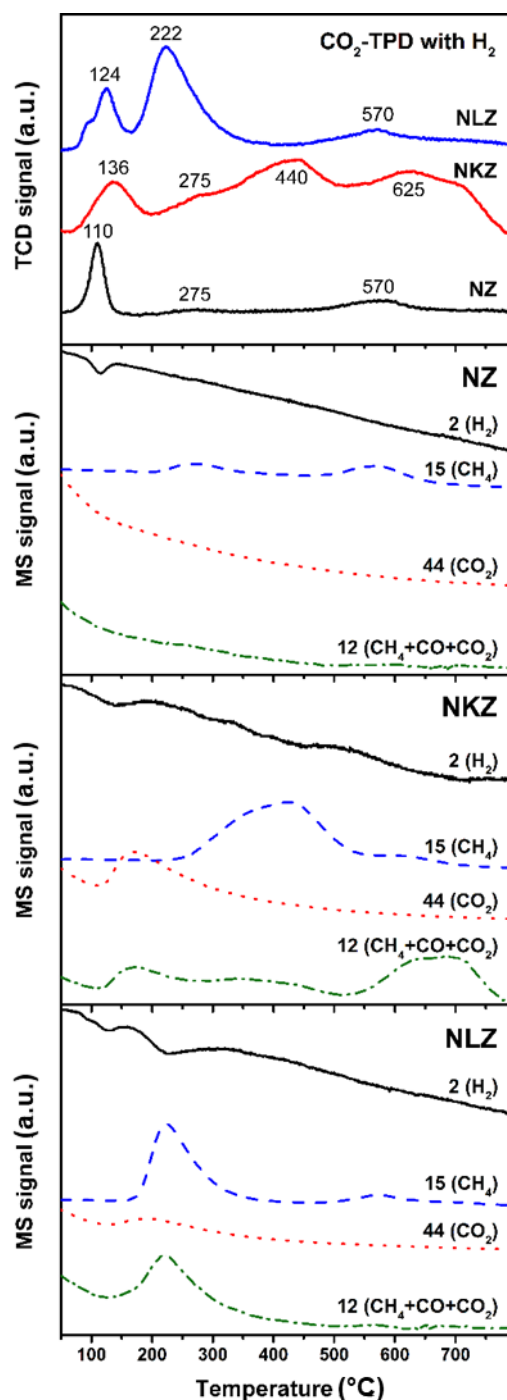


Figure 6.6 - (top panel) Reactive (reductive) CO₂-TPD profiles with H₂ of Ni/ZrO₂, Ni-K/ZrO₂ and Ni-La/ZrO₂. (lower three panels) The MS signals observed during the CO₂-TPD with H₂. The number and formula in brackets represent the mass to charge ratio (m/z) and the corresponding plausible chemicals.

6.3.3 Space- and time-resolved operando DRIFTS

With the convincing observations and evidences of the promoter effects, we further investigated the effects of the promoters on the formation and evolution of surface

species along the axial direction of the catalyst bed by DRIFTS. Time-resolved DRIFTS spectra were measured at equally-spaced 4 positions (we call them Front, Middle 1, Middle 2 and Back) along the catalyst bed. It should be noted that the last spectrum of the reduction phase, where the catalyst surface is likely the cleanest during a CCR cycle was taken as the internal background to calculate the DRIFT spectra. In other words, if there are surface species stably present during CCR, e.g. stable potassium carbonate as indicated before, the spectral feature will not appear and only those responding to the CCR unsteady-state condition and responsible for CCR chemistry appear in the spectra.

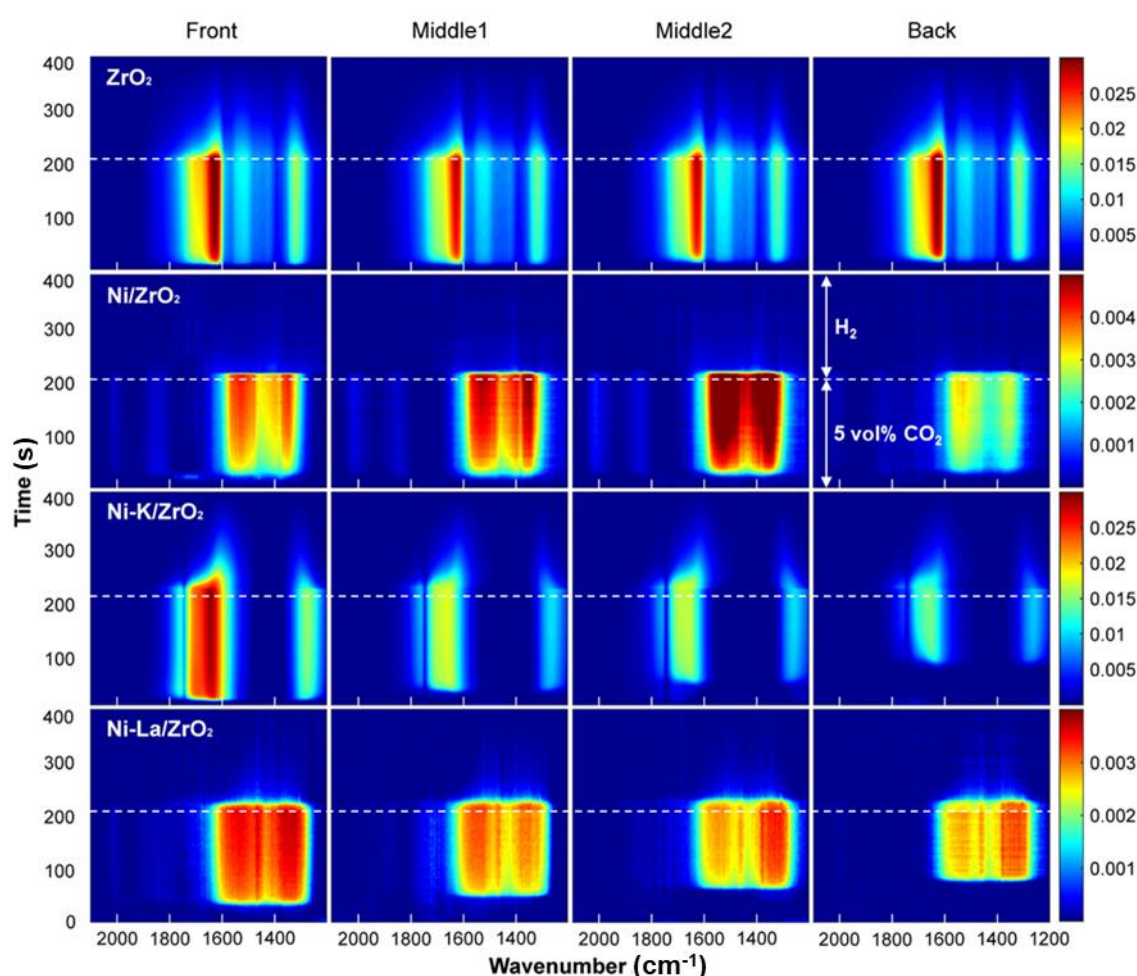


Figure 6.7 - Space- and time-resolved *operando* DRIFT spectra of ZrO₂, Ni/ZrO₂, Ni-K/ZrO₂ and Ni-La/ZrO₂ at 350 °C under the CCR condition (5 vol% CO₂ in He vs. pure H₂, both at 10 mL/min). The last spectrum of the CCR cycle was taken as the background. The scale is shown in absorbance unit.

Figure 6.7 shows the evolution of surface species during CCR for the three catalysts and also for ZrO₂ which was also evaluated as a comparative reference. For the ZrO₂ support, the main bands observed during the capture phase were at 1320, 1420, 1522 and 1629, which can be assigned to bicarbonate and carbonate species formed over ZrO₂¹⁹. After impregnating Ni on the support (i.e. NZ), the spectral features changed completely; these bands disappeared and the bands of formate species (1351 and 1521 cm⁻¹) and weakly bound carbonate species (1400 cm⁻¹) appeared in the capture phase^{19,20}. The La-promoted catalyst (NLZ) exhibited the similar spectral features to those of NZ with some band broadening likely caused by the strong interaction between Ni and La which impacts on the reducibility of Ni (Figure 6.5). It is interesting to note some signatures of adsorbed CO species on Ni (linear one at 2013 cm⁻¹ and bridged one at 1850 cm⁻¹) for NZ and NLZ^{21,22}. This indicates that the Ni surface is reduced and exposed during the CCR. In contrast, K-promotion (NKZ) totally changed the type of surface species formed during the capture phase with the formation of the bands possibly assigned to formyl species (1760 cm⁻¹) and bidentate carbonate (1277 and 1657 cm⁻¹)^{23,24}. The former is generally considered as a plausible intermediate for CO₂ methanation²³. This is a strong evidence that the function of K and La promoters are chemically and completely different in capturing CO₂ on the catalyst surface.

There are two important observations one can make based on the space-resolved approach. The first one is the travelling of the so-called CO₂-capture front, i.e. a gradual movement of position towards the back position where CO₂ capture (surface species formation) starts, which is more clearly visible for NKZ and NLZ (CO₂ concentration profiles extracted from DRIFTS data are shown in Figure 6.8). On the other hand, such CO₂ capture front is not clearly visible for ZrO₂ and NZ, indicating less aggressive CO₂ capture. The second important observation is the spatial gradient of the amount of surface species formed upon CO₂ capture as indicated by the value of absorbance (i.e. color in Figure 6.7) along the catalyst bed. For ZrO₂, the amount of surface species is homogeneously distributed over the catalyst bed, while a very large concentration gradient of surface species was observed for NZ and NKZ and to a lesser extent for NLZ. It is important to notice that most of the CO₂ capture processes take place near the front position of the catalyst for NKZ, whereas NLZ captures CO₂

throughout the catalyst bed with much less concentration gradient of the surface species.

In the reduction phase, the formed surface species are consumed completely, forming CH₄ and releasing CO₂, depending on the catalyst. The action of reductive surface species transformation is also very distinct for the two contrasting catalysts, NKZ and NLZ. In case of NKZ, the transformation starts at all positions but very slowly by gradually consuming surface species for CH₄ formation. On the other hand, the reduction process of NLZ is a fast process with a drastic decrease in the concentration of the surface species, forming a slight but firm reduction front (reducing the surface species step-by-step towards the back position). This reduction profile is ideal for CCR process since most of the H₂ is consumed for the transformation and thus H₂ utilization efficiency is high.

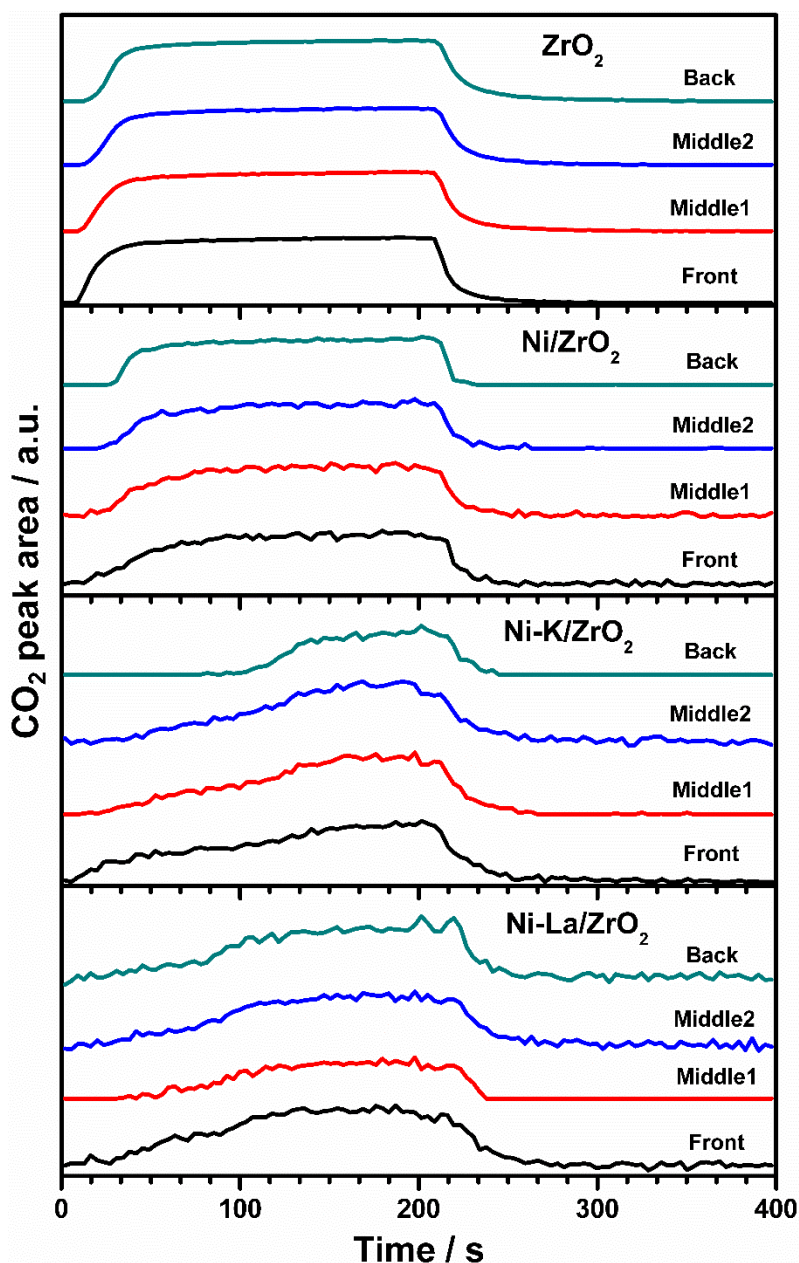


Figure 6.8 - Temporal evolution of the band area of gas phase CO₂ extracted from space- and time-resolved DRIFT spectra acquired at 350 °C at the four positions.

6.4 Conclusions

CO₂ methanation by Ni-based catalysts using the isothermal unsteady-state operation enabling CO₂ capture and conversion steps in one process, i.e. CO₂ capture and reduction (CCR) approach, was investigated. The roles of two promoters, K and La, to Ni/ZrO₂ in CO₂ capture as well as CO₂ conversion to methane were studied and their functions were elucidated by H₂-TPR, reductive CO₂-TPD in H₂ atmosphere and space- and time-resolved *operando* DRIFTS. First, all Ni-based catalysts are highly

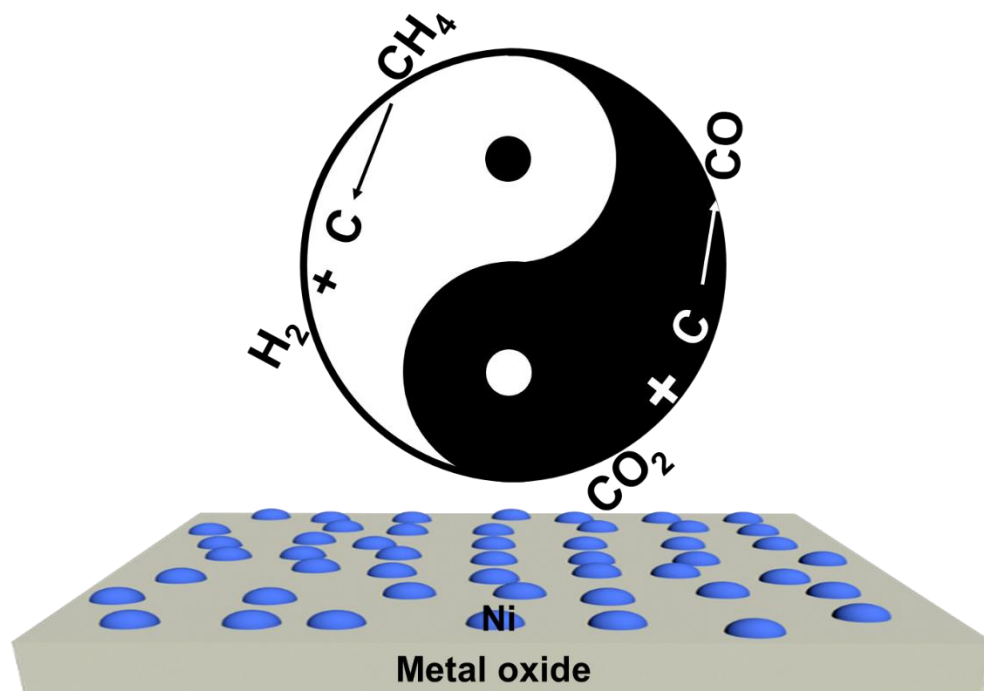
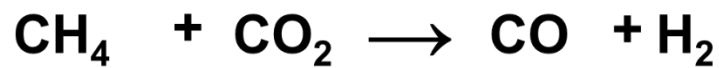
selective in CH₄ formation. The K-promotion is more effective in enhancing CO₂ capture capacity, but the capacity and consequently the CCR performance deteriorates at low temperature. In contrast, the La-promotion affords to enhance CO₂ capture capacity moderately and importantly to convert the captured CO₂ very rapidly to CH₄ with high H₂ utilization efficiency as evidenced by space- and time-resolved DRIFTS. The TPR and TPD studies show that the La-promoter improves reducibility of Ni without changing the reaction mechanism from that of Ni/ZrO₂ by forming active formate intermediate species for CH₄ production. On the other hand, the K-promotion altered the reaction mechanism completely where formyl species cooperated with bidentate carbonates are the active surface species which are more difficult to be reduced by H₂ to CH₄. This study firmly shows the possibility to achieve high CO₂ conversion and high CH₄ selectivity at low temperature (e.g. 250 °C) using Ni-La/ZrO₂ and at increased capacity using Ni-K/ZrO₂ only at high temperature (efficiently at >350 °C) by the CCR approach. The K-promoted catalyst binds CO₂ strongly and is advantageous in avoiding the release of unreacted CO₂ during the reduction phase. This work shows clearly the distinct advantages of the two promoters to the Ni catalyst in CCR operation and is expected to open further discussions and technical evaluation of CCR process in comparison to the conventional, two-step CO₂ capture and conversion approach.

Bibliography

1. J. Gibbins and H. Chalmers, *Energ. Policy*, 2008, **36**, 4317-4322.
2. J. T. Litynski, S. M. Klara, H. G. McIlvried and R. D. Srivastava, *Environ. Int.*, 2006, **32**, 128-144.
3. C. Song, *Catal. Today*, 2006, **115**, 2-32.
4. P. J. Lunde and F. L. Kester, *Ind. Eng. Chem. Proc. DD*, 1974, **13**, 27-33.
5. A. Álvarez, A. Bansode, A. Urakawa, A. V. Bavykina, T. A. Wezendonk, M. Makkee, J. Gascon and F. Kapteijn, *Chem. Rev.*, 2017, **117**, 9804-9838.
6. M. Lenzen, *Crit. Rev. Env. Sci. Tec.*, 2011, **41**, 2169-2185.
7. R. Snieder and T. Young, *GSA Today*, 2009, **19**, 36-37.
8. L. F. Bobadilla, J. M. Riesco-García, G. Penelás-Pérez and A. Urakawa, *J. CO₂ Util.*, 2016, **14**, 106-111.
9. T. Hyakutake, W. van Beek and A. Urakawa, *J. Mater. Chem. A*, 2016, **4**, 6878-6885.
10. W. Wei and G. Jinlong, *Frontiers of Chemical Science and Engineering*, 2011, **5**, 2-10.
11. C. Mebrahtu, S. Abate, S. Perathoner, S. Chen and G. Centi, *Catal. Today*, 2017, DOI: <https://doi.org/10.1016/j.cattod.2017.08.060>, In Press.
12. F. Wang, S. He, H. Chen, B. Wang, L. Zheng, M. Wei, D. G. Evans and X. Duan, *J. Am. Chem. Soc.*, 2016, **138**, 6298-6305.
13. A. Urakawa, N. Maeda and A. Baiker, *Angew. Chem.*, 2008, **120**, 9396-9399.
14. M. T. Duignan, E. Grunwald and S. Speiser, *J. Phys. Chem-us*, 1983, **87**, 4387-4394.
15. T. K. Campbell and J. L. Falconer, *Applied Catalysis*, 1989, **50**, 189-197.
16. J. Wambach, G. Illing and H. J. Freund, *Chem. Phys. Lett.*, 1991, **184**, 239-244.
17. H.-S. Roh, K.-W. Jun, W.-S. Dong, J.-S. Chang, S.-E. Park and Y.-I. Joe, *Journal of Molecular Catalysis A: Chemical*, 2002, **181**, 137-142.
18. S. Li, C. Zhang, Z. Huang, G. Wu and J. Gong, *Chem Commun (Camb)*, 2013, **49**, 4226-4228.
19. H. Takano, Y. Kirihata, K. Izumiya, N. Kumagai, H. Habazaki and K. Hashimoto, *Applied Surface Science*, 2016, **388**, 653-663.
20. N. M. Gupta, V. S. Kamble, V. B. Kartha, R. M. Iyer, K. R. Thampi and M. Gratzel, *J. Catal.*, 1994, **146**, 173-184.
21. H. Muroyama, Y. Tsuda, T. Asakoshi, H. Masitah, T. Okanishi, T. Matsui and K. Eguchi, *J. Catal.*, 2016, **343**, 178-184.
22. S.-i. Fujita, M. Nakamura, T. Doi and N. Takezawa, *Applied Catalysis A: General*, 1993, **104**, 87-100.
23. C. Schild, A. Wokaun and A. Baiker, *J Mol. Catal.*, 1991, **69**, 347-357.
24. F. Solymosi and H. Knozinger, *J. Catal.*, 1990, **122**, 166-177.

7 DRY REFORMING OF METHANE

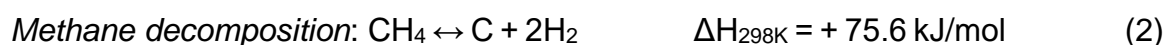
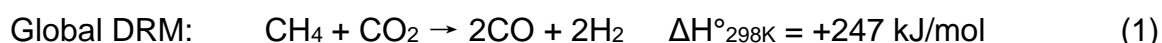
Enabling CO_2 and CH_4 converted independently via chemical looping dry reforming of methane



7.1 Introduction

As the greenhouse gases, both CO₂ and CH₄ functionalization are meaningful for mitigating the global warming. Meantime, CO₂ functionalization turns the ‘waste’ to valuable chemicals such as CO and CH₃OH^{1, 2}, and CH₄ functionalization can make use of the relative abundant natural gas more efficiently rather than simply burning it to generate heat or electricity. Thus, to functionalize CO₂ and CH₄ has great significance from the view of both environment and economics.

Dry reforming of methane (DRM), as shown in equation (1) is the reaction can convert both CO₂ and CH₄ into syngas, i.e. CO and H₂, which are widely used in the modern chemical industrial, such as Fischer–Tropsch (FT) synthesis. Moreover, CO/H₂ ratio in the products of DRM is lower than that from currently industrialized steam reforming of methane (SRM) process³, which is more favourable for long-chain hydrocarbon synthesis in FT process⁴⁻⁶. As generally accepted, the reaction mechanism of catalytic DRM can be depicted in two steps: methane decomposition (eq. 2) and carbon gasification (eq. 3)⁷. Both steps are endothermic. Hence, the reaction is normally conducted at high temperature (above 700 °C)^{8, 9}. Coke is hardly avoided under this condition and its accumulation commonly causes the catalyst deactivation¹⁰⁻¹⁴. This is one of the main reasons that limit the industrial application of DRM.



Targeting this problem, a new concept was brought up to make use of the coke formation by splitting DRM into two independent reactions based on its reaction mechanism. This is chemical looping dry reforming of methane (CLDR): alternatively flowing CO₂-containing gas and CH₄ containing gas into the reactor^{15, 16}. Products formed in CLDR is naturally separated, which is favourable for the applications that need pure CO or pure H₂. CLDR has been successfully implemented with SiO₂ supported Ni catalyst, and the catalytic performance was studied in terms of CO₂ and CH₄ conversion. It showed that the full CO₂ and CH₄ conversion was not reached yet¹⁶.

To improve the catalytic performance, the knowledge about how methane decomposition and carbon gasification behaves in the independent steps is needed. Hence, we aim at exploring how the catalyst affects the two independent steps herein. Ni-based catalyst is used in this work due to its low cost and excellent activity towards DRM. SiO₂, ZrO₂ and Al₂O₃ have been studied as the support materials. The influence of Fe, K and La as promoters on methane decomposition and carbon gasification is deeply discussed as well as the temperature.

7.2 Experimental

7.2.1 Materials and catalyst preparation

Nickel nitrate hexahydrate (>98%, Alfa Aesar), potassium carbonate (>99%, Acros), lanthanum nitrate hexahydrate (>99.9%, Alfa Aesar), iron (III) nitrate nonahydrate (\geq 98%, Sigma Aldrich), zirconium oxide (Alfa Aesar, 90 m²/g), alumina (Alfa Aesar, gamma phase, 1/8 pellet) and silica (Alfa Aesar, 261 m²/kg) were used as received. All catalyst materials were synthesized by the incipient wetness impregnation method. Ni/SiO₂ (15/85 wt%, NS), Ni/Al₂O₃ (15/85 wt%, NA), Ni/ZrO₂ (15/85 wt%, NZ), Ni-Fe/ZrO₂ (15/5/80 wt%, NFZ) and Ni-La/ZrO₂ (15/5/80 wt%, NLZ) were prepared by (co)impregnating the aqueous solution of the corresponding nitrate salts onto SiO₂, Al₂O₃ or ZrO₂. For Ni-K/ZrO₂ (15/5/80 wt%, NKZ), firstly nickel nitrate was impregnated on ZrO₂, dried overnight at 80 °C and then calcined at 500 °C for 5 h. Subsequently, the aqueous solution of K₂CO₃ was impregnated on Ni/ZrO₂. After the impregnation step, all samples were dried overnight at 80 °C and then calcined at 500 °C for 5 h.

7.2.2 Catalyst characterization

Power X-ray diffraction (PXRD) was performed on D8 Advanced Powder Diffractometer (Bruker) equipped with a vertical 2theta-theta goniometer in transmission configuration, with a K α_1 germanium monochromator for Cu radiation ($\lambda=1.5406$ Å), at a scan step of 0.02°/s from 10° to 80°.

7.2.3 Catalytic reaction

Catalysts were first pelleted, crushed and sieved to the size of 200-300 μm . 200 mg of certain catalyst was charged into a quartz tube reactor, fixed with quartz wool and pre-reduced in pure H₂ (50 mL/min) at 450 °C for 30 min before reaction. Then the

reactor was heated up to the desired reaction temperature (450, 550, 650, 750 or 800 °C) in He and the catalyst was evaluated under a CLDR reaction condition. CO₂-containing flow (10.6 vol% in He), pure He, CH₄-containing gas (11.2 vol% in N₂) and pure He were alternatively introduced into the reactor with all flow rates at 50 mL/min at the ambient pressure, and they are named as CO₂ phase, flushing phase, CH₄ phase and flushing phase respectively. As described in Chapter 2, the flow sequence was XFYP mode (CO₂ – He - CH₄ - He), and it was controlled by two computer-controlled switching valves which were synchronized with the gas detection using the transmission IR spectroscopy through the gas cell mounted in ALPHA FT-IR spectrometer (Bruker). The gas detection gives a time-resolution of 5 s for quantitative gas analysis of CO₂, CO and CH₄. To improve the S/N of the detection, six XFYP cycles were evaluated for each catalyst at a specific experimental condition and the concentration profiles were averaged into one XFYP cycle after making sure that the profiles are reproducible. Figure 7.1 shows the averaged concentration profile of CO₂, CH₄ and CO in the blank test conducted at ambient temperature without catalyst. The concentration of these three gases was integrated separately for the calculation of CO₂/CH₄ conversion and ratio of converted CO₂ to converted CH₄. Besides, H₂ evolution was monitored by mass spectrometer, confirming that H₂ was only produced in CH₄ phase (profiles not shown in the chapter)

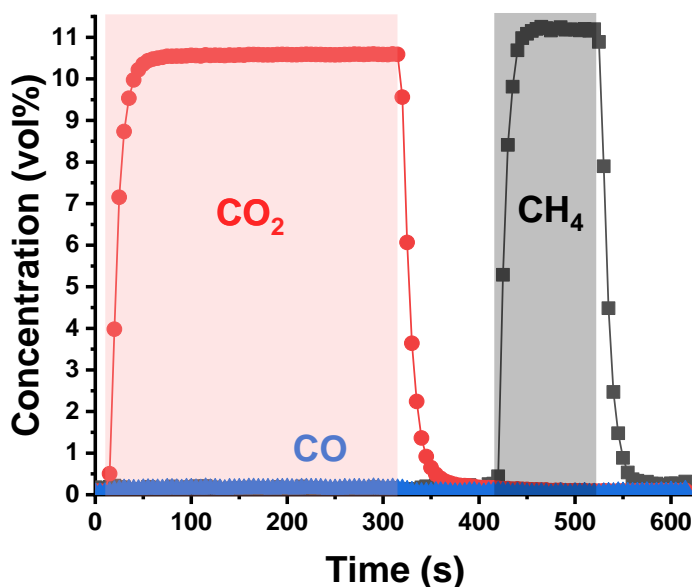


Figure 7.1 - Averaged concentration profile of CO₂ (red), CH₄ (black) and CO (blue) in one cycle of CLDR during blank test at room temperature without catalyst: CO₂ phase is in pink area (10.6 vol% CO₂ in He, 50 mL min⁻¹), CH₄ phase is in grey area (11.2 vol% in N₂, 50 mL/min) and flushing phase is in white area (pure He, 50 mL/min).

7.3 Results and discussion

Ni-based catalyst supported by different metal oxides and with different promoters were firstly characterized by PXRD. As shown in Figure 7.2, only the patterns of NiO and corresponding supports, SiO₂, γ -Al₂O₃ and monoclinic ZrO₂, emerge in the profiles. The promoters, Fe, K and La are not detectable by PXRD, even though the loading of these components is 5 wt%, indicating that these species are well distributed nanocrystals or present in amorphous phase.

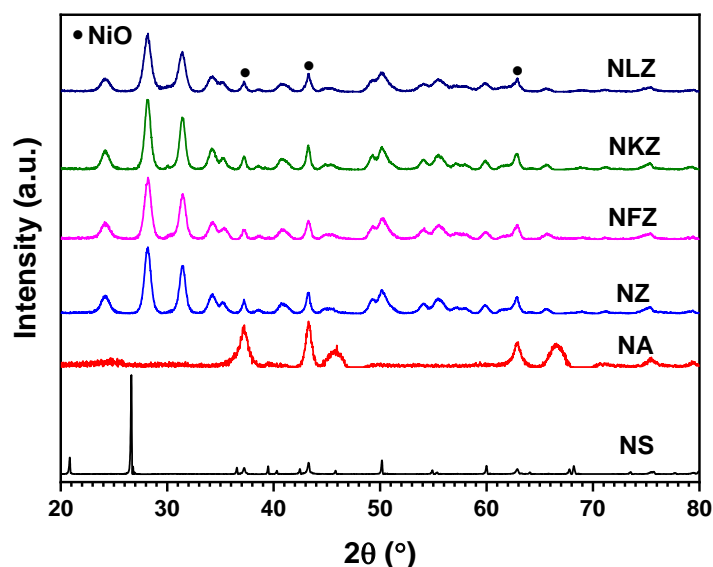


Figure 7.2 - XRD profiles of catalysts adopted in the chapter.

7.3.1 The effect of different support materials

Firstly, SiO_2 , ZrO_2 and Al_2O_3 as support materials have been studied for CLDR. Figure 7.3 displays the CO_2/CH_4 conversion and ratio of converted CO_2 to converted CH_4 on the corresponding Ni-based catalysts during CLDR at 550 °C and 650 °C. The last descriptor describes the reactivity of CO_2 reducing coke formed via CH_4 decomposition: ideally, when the value reaches 1, it represents full conversion of the coke. Generally, the value of three descriptors increase with temperature rise and the values of the last descriptor are all below 1, which verifies the positive effect of temperature on CLDR, and it is more difficult to convert CO_2 than CH_4 . This is related with the positive enthalpy of the two step reactions (methane decomposition and carbon gasification) in CLDR and the relative higher enthalpy of carbon gasification. ZrO_2 and Al_2O_3 supported catalysts display similar catalytic activity, and they give higher CO_2 conversion at both temperatures and higher CH_4 conversion at 650 °C comparing to SiO_2 supported catalyst. Therefore, the three support materials follow the sequence in terms of their catalytic performance during CLDR: $\text{ZrO}_2 \approx \text{Al}_2\text{O}_3 > \text{SiO}_2$. Considering the slightly higher ratio of converted CO_2 to CH_4 on ZrO_2 supported catalyst, ZrO_2 is used as the support in the following studying in the chapter.

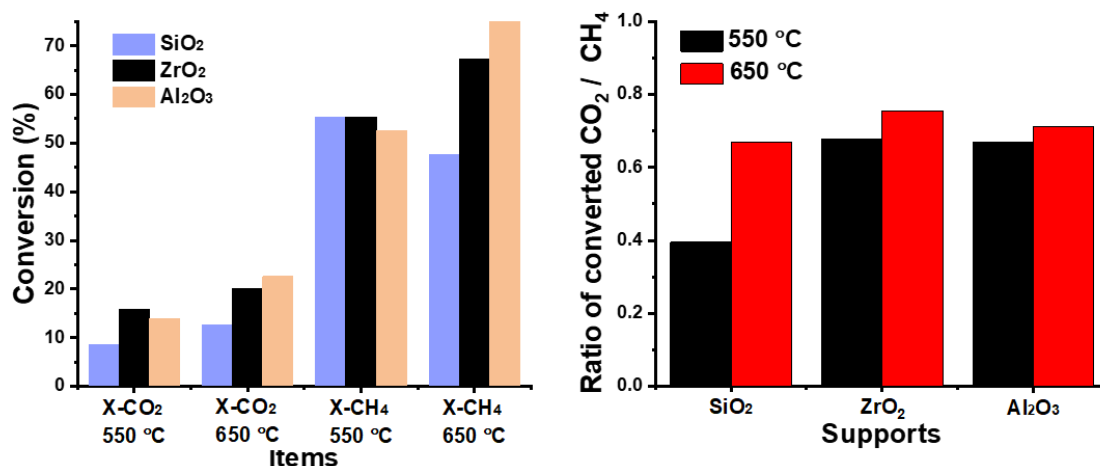


Figure 7.3 - CO₂, CH₄ conversion (left) and ratio of converted CO₂ to converted CH₄ with SiO₂, ZrO₂ and Al₂O₃ supported Ni catalysts during CLDR at 550 °C and 650 °C.

7.3.2 Temperature effect on CO₂ conversion and CH₄ decomposition

ZrO₂ supported Ni catalysts have been studied at different temperatures. Corresponding concentration profiles of CO₂, CO and CH₄ during CLDR are shown in Figure 7.4. The pink and the grey background marks CO₂ phase and CH₄ phase respectively, and the white area is He flushing phase which avoids the co-existence of gaseous CO₂ and CH₄, making sure CH₄ decomposition and carbon gasification occur independently.

Looking into the grey area, CH₄ is immediately detected when the flow switches from flushing phase to CH₄ phase at the temperature from 450 °C to 650 °C, but CH₄ detection is delayed for ca. 50 s when the temperature reaches 750 °C (Figure 7.4a, b, c, d). It means that CH₄ conversion changes from taking place on the whole catalyst bed to occurring gradually along the catalyst bed from the beginning of CH₄ phase. This tells a drastic improvement on the kinetics of CH₄ conversion once lifting up the temperature to 750 °C. The level-off values of CH₄ concentration are all lower than that in the feed (11.2 vol%) and decays significantly from 450 °C to 750 °C, also demonstrating the efficient enhancement of CH₄ conversion by increasing temperature. Further arising temperature from 750 °C to 800 °C does little help on CH₄ conversion (Figure 7.4d, e). To be noticed, there are some CO and CO₂ formation (concentration peak value \approx 1.3 vol%) at the beginning of CH₄ phase since 650 °C. This CH₄ overoxidation is detrimental to catalytic performance of CLDR. As reported in the

literature, absorbed oxygen species are favourable for DRM reaction¹⁷. Thus, the overoxidation of CH₄ here is probably attributed to the highly oxidative lattice oxygen sites generated in CO₂ phase such as oxidised Ni.

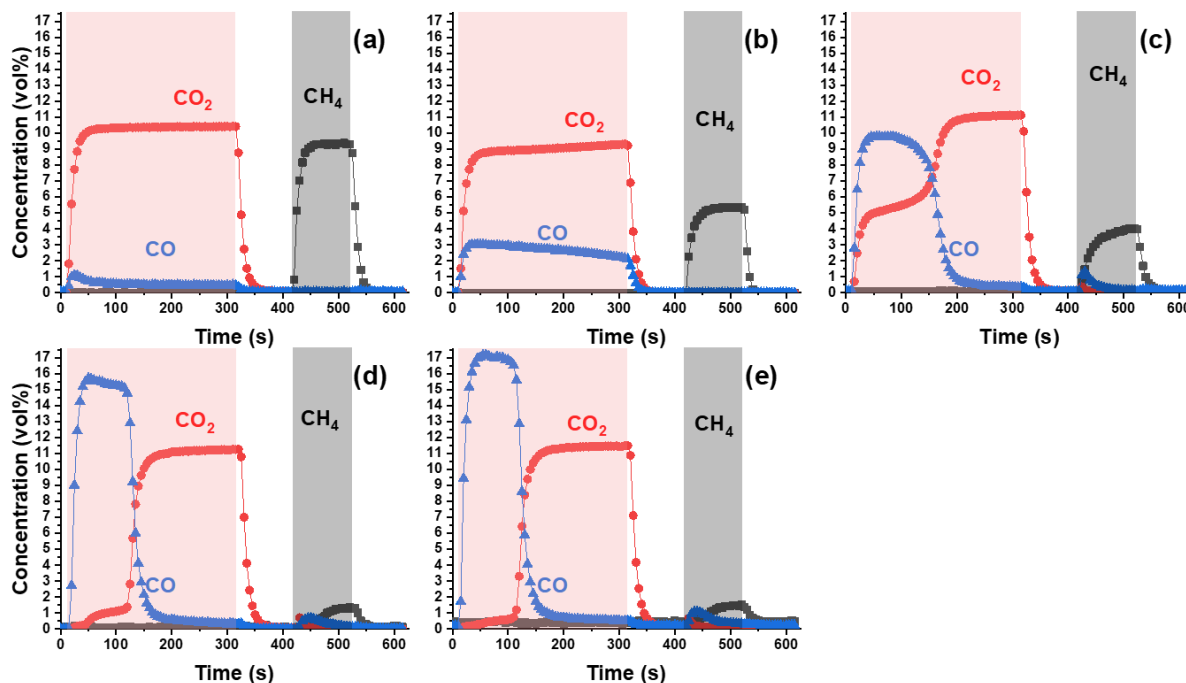


Figure 7.4 - Averaged concentration profiles of CO₂ (red), CH₄ (black) and CO (blue) in one cycle of CLDR on Ni/ZrO₂ at 450 °C (a), 550 °C (b), 650 °C (c), 750 °C (d) and 800 °C (e): CO₂ phase is in pink area (10.6 vol% CO₂ in He, 50 mL/min), CH₄ phase is in grey area (11.2 vol% in N₂, 50 mL/min) and flushing phase is in white area (pure He, 50 mL/min).

In the pink area (CO₂ phase), CO formation is well synchronised with CO₂ conversion as shown in Figure 7.4. At 450 °C and 550 °C, CO concentration rapidly rises to a peak value then slowly decays with time goes in the remaining CO₂ phase. At 650 °C, CO concentration peaks at higher value (9.8 vol%) comparing that at 550 °C and drops sharply to almost zero after 120 s where carbon formed via CH₄ decomposition is almost fully re-oxidised to CO. However, CO₂ (ca. 5 vol%) still exists during the high CO concentration plateau. These demonstrates the slow kinetics of CO₂ conversion and the positive effect of temperature on CO₂ conversion. Similar to CH₄ conversion, delayed CO₂ detection in CO₂ phase is desired as it represents the full conversion of CO₂. However, this full conversion of CO₂ in the pink area emerges until the temperature reaches 750 °C exactly where a period of CH₄ full conversion happens as shown in Figure 7.4. The difference is that, this full CO₂ conversion can be

lengthened by increasing the temperature from 750 °C to 800 °C, showing higher temperature dependency of CO₂ conversion than CH₄ conversion, which is in accordance with the higher difficulty of CO₂ conversion shown in the studying of support effect.

7.3.3 The effect of different promoters (Fe, K, La)

To improve the catalytic activity of Ni/ZrO₂ for CLDR, three promoters, Fe, K and La, have been doped into the catalyst and studied under CLDR condition at different temperatures. Figure 7.5 exhibits CO₂/CH₄ conversion and ratio of converted CO₂ to converted CH₄ during CLDR on ZrO₂ supported Ni catalyst with / without promoters.

It is clear that potassium addition lowers down CO₂ and CH₄ conversion markedly, which is opposite to its effect in co-feed DRM process¹⁸. As reported, adding K can improve the catalyst stability via reducing coke formation, which answers for the lower CH₄ conversion that is mainly originated from CH₄ decomposing to coke in CLDR process. And the less available coke finally results lower CO₂ conversion. This explanation is verified by the highest peak value of CH₄ concentration in CH₄ phase and similar peak value of CO concentration in CO₂ phase for K-promoted catalyst among the profiles for the four catalysts shown in Figure 7.6. In terms of the ratio of converted CO₂ to converted CH₄, NKZ also shows lower value generally, i.e. it is less capable to remove coke in CO₂ phase, indicating its damage on the activity of carbon gasification reaction. Therefore, K addition restrains both the activity of CH₄ decomposition and carbon gasification.

Iron addition does little change on both CO₂ and CH₄ conversion at the temperature from 450 °C to 650 °C, but shows negative effect at 750 °C and 800 °C. Differently, the ratio of converted CO₂ to CH₄ on NFZ is higher than that on NZ at the whole studied temperature range and it goes even above 1 at 750 °C. From the concentration profile of CO, CO₂ and CH₄ at 800 °C, it can be concluded that CO formation on NFZ in CO₂ phase has two plateaus: the fast CO formation until 50 s at the beginning of CO₂ phase and the continuous but slower CO formation in the rest part of CO₂ phase. In CH₄ phase, CH₄ concentration for NFZ increases faster and reaches higher value than that for NZ, showing the activity reducing of CH₄ decomposition. Strikingly, CO₂ and CO formation at the beginning of CH₄ phase is notably enhanced, which proves the strong oxidative ability of NFZ. The enhancement on the oxidative ability by Fe agrees with

previous reports^{19,20}. The oxidative sites generated via Fe addition get reduced in CH₄ phase via oxidising CH₄ to CO and CO₂, then become re-oxidised by CO₂ in CO₂ phase, causing CO₂ conversion without contributing removal of coke. This explains the high ratio of converted CO₂ to CH₄ on NFZ. Besides, the oxidative sites re-oxidisation may also contribute to the second plateau of CO concentration curve in CO₂ phase. In a conclusion, iron addition is unfavourable for ZrO₂ supported Ni catalyst applied to CLDR process.

La promoter promotes both CO₂ and CH₄ conversion at the whole studied temperatures, and these conversions continuously increase with temperature rise, as well as the ratio of converted CO₂ to converted CH₄ that even gets close to 1 at 800 °C. These demonstrate the positive effect of La addition. Moreover, almost full CH₄ conversion is observed in the concentration profile of NLZ, and the full CO₂ conversion length (90 s) is doubled comparing to that (45 s) for NZ (Figure 7.6). More importantly, the CO and CO₂ formation in CH₄ phase is prominently suppressed. Therefore, La promoter truly enhances the catalytic performance of ZrO₂ supported Ni catalyst for CLDR process.

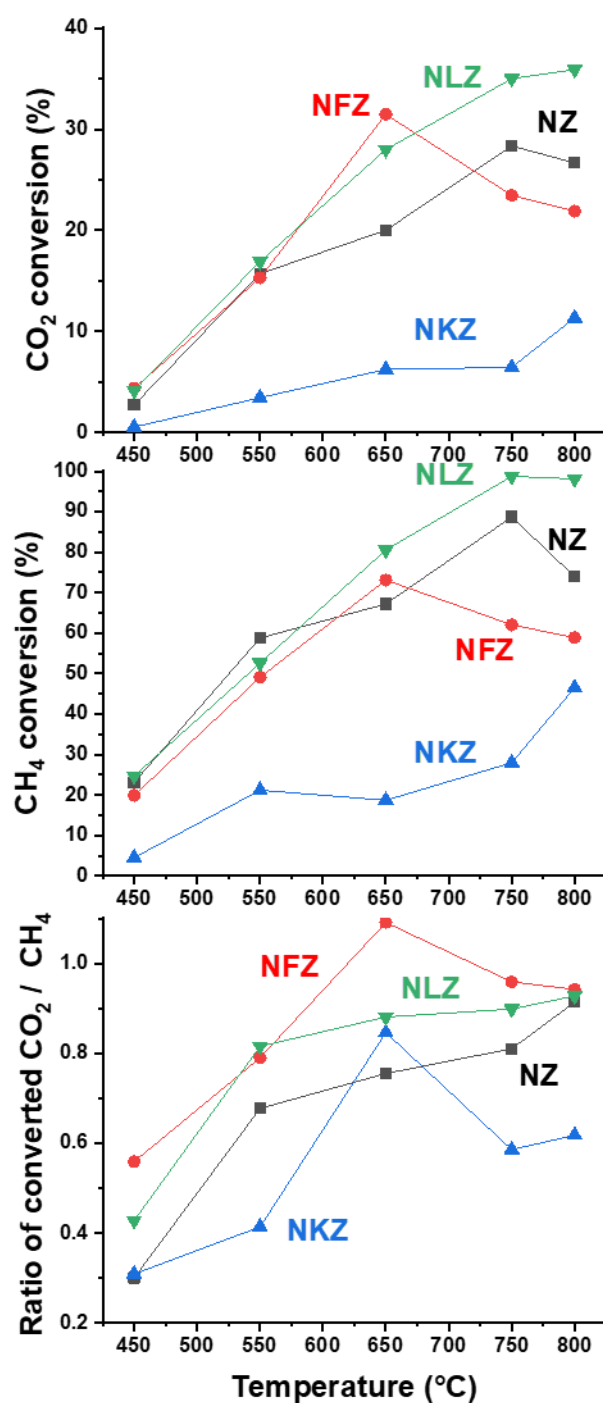


Figure 7.5 - CO₂ conversion (top panel), CH₄ conversion (middle panel) and ratio of converted CO₂ to converted CH₄ (bottom panel) on ZrO₂ supported Ni catalyst (black, NZ) without / with Fe (red, NFZ), potassium (blue, NKZ) and La (green, NLZ) promoters during CLDR at 450 °C, 550 °C, 650 °C, 750 °C and 800 °C.

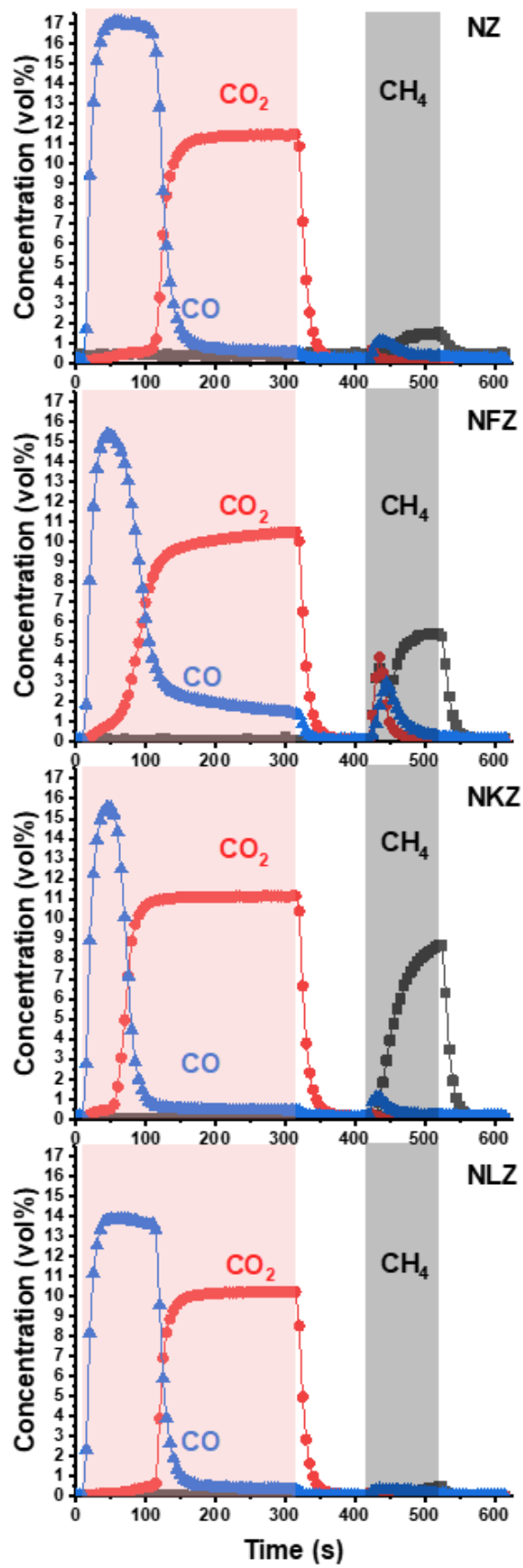


Figure 7.6 - Averaged concentration profiles of CO₂ (red), CH₄ (black) and CO (blue) in one cycle of CLDR at 800 °C on Ni/ZrO₂ (top panel, NZ), Ni-Fe/ZrO₂ (second panel, NFZ), Ni-K/ZrO₂ (third panel, NKZ), Ni-La/ZrO₂ (bottom panel, NLZ): CO₂ phase is in pink area (10.6 vol% CO₂ in He, 50 mL/min), CH₄ phase is in grey area (11.2 vol% in N₂, 50 mL min⁻¹) and flushing phase is in white area (pure He, 50 mL/min).

7.3.4 The effect of CH₄ phase length on CO₂ conversion

To be noticed in Figure 7.6, the peak value of CO concentration in CO₂ phase for NLZ (13.9 vol%) is relatively lower than that for other three catalysts (above 15.5 vol%), which reflects the initial slow kinetics of CO₂ conversion. As CH₄ is almost fully converted on NLZ, it suggests the large amount of coke formed in CH₄ phase may change the reactivity of the coke or cover the active sites, hindering CO₂ conversion in CO₂ phase. To verify that, we conducted the CLDR process with different length of CH₄ phase (33 s, 55 s, 105 s) on NLZ at 800 °C.

Figure 7.7 displays the corresponding peak value of CO concentration in CO₂ phase and when it appears based on the concentration profiles obtained from the above experiments. The lowest peak value of CO concentration and shortest time to reach the peak value of CO concentration are both shown when the CH₄ phase length is 30 s, which can be assigned to the least available coke formed during CH₄ phase. Interestingly, the highest peak value of CO concentration and the longest time to get the peak value of CO concentration appear with different length of CH₄ phase: the former is with 55 s of CH₄ phase and the latter is with 105 s of CH₄ phase. This manifests that the coke amount really affects its gasification rates. Less coke accelerates carbon gasification reaction kinetics. As reported, CH₄ decomposition can form different types of coke such as polymeric, filamentous, and graphitic coke²¹. And the reactivity of carbon in its gasification is related with carbon type²². Hence, one plausible explanation is that varying CH₄ phase length changes the type of coke formed via CH₄ decomposition, finally affects the kinetics of CO₂ conversion in CO₂ phase. Further investigation can be done for the identification of the coke type.

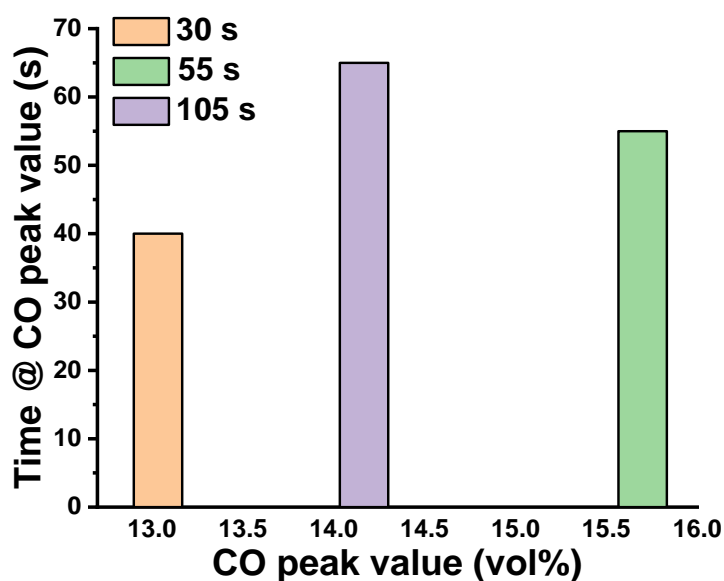


Figure 7.7 - The time when the peak value of CO concentration shows vs. corresponding the peak value of CO concentration in the concentration profiles obtained on NLZ during CLDR with different length of CH₄ phase (30 s, 55 s and 100 s) at 800 °C.

7.4 Conclusion

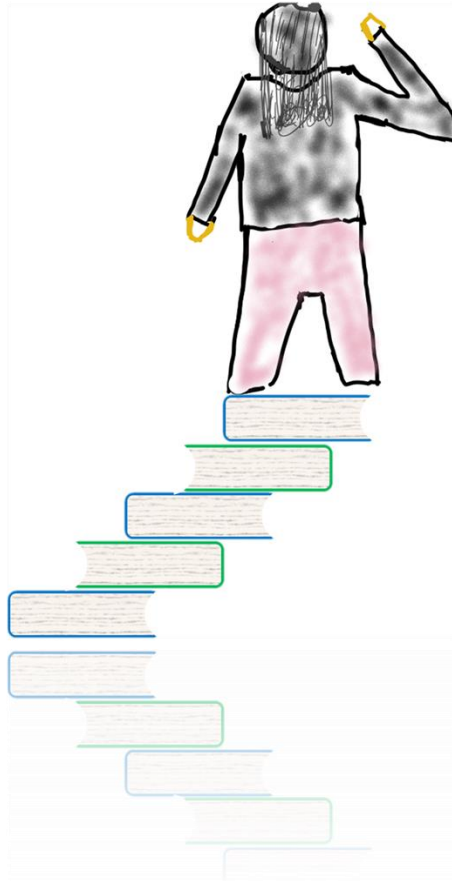
Chemical looping dry reforming of methane (CLDR) has been successfully applied to functionalising both CO₂ and CH₄ for independent CO and H₂ synthesis using Ni-based catalysts. Three support materials, SiO₂, Al₂O₃ and ZrO₂, have been studied and ZrO₂ gives the optimal performance among these materials. Based on ZrO₂ supported Ni catalyst, the positive effect of temperature on both CO₂ conversion and CH₄ conversion is viewed and it is found that CO₂ conversion step is more temperature-dependent. Iron, potassium and lanthanum have been investigated as promoters for CLDR. Based on the catalytic performance of these catalysts under CLDR condition at different temperatures, Fe addition is proved to enhance the oxidizability of the catalyst, causing over-oxidation of CH₄ during CH₄ decomposition step. Different from the case in the co-feed dry reforming of methane reaction, K addition suppresses both CO₂ conversion and CH₄ conversion. La is the promising promoter for CLDR process due to its effective improvement on both CO₂ and CH₄ conversion, which makes it possible to achieve full conversion of both CO₂ and CH₄ in one CLDR process. Besides, the length of CH₄ phase is found to have effect on the

kinetics of CO₂ conversion step. And this is suggested to refer to coke types formed via CH₄ decomposition. Further studying can be conducted for its clarification.

Bibliography

1. M. Bowker, *ChemCatChem*, 2019, **11**, 4238-4246.
2. L. Liu, S. Das, T. Chen, N. Dewangan, J. Ashok, S. Xi, A. Borgna, Z. Li and S. Kawi, *Appl. Catal. B-Environ*, 2020, **265**, 118573.
3. P. Gangadharan, K. C. Kanchi and H. H. Lou, *Chem. Eng. Res. Des.*, 2012, **90**, 1956-1968.
4. M. Ding, Y. Yang, Y. Li, T. Wang, L. Ma and C. Wu, *Applied Energy*, 2013, **112**, 1241-1246.
5. I. C. Yates and C. N. Satterfield, *Energy & fuels*, 1992, **6**, 308-314.
6. A. A. Lemonidou and I. A. Vasalos, *Applied Catalysis A: General*, 2002, **228**, 227-235.
7. L. S. Gangurde, G. S. J. Sturm, M. J. Valero-Romero, R. Mallada, J. Santamaria, A. I. Stankiewicz and G. D. Stefanidis, *Chemical Engineering and Processing - Process Intensification*, 2018, **127**, 178-190.
8. M. K. Nikoo and N. A. S. Amin, *Fuel Process. Technol.*, 2011, **92**, 678-691.
9. Y. Wang, L. Yao, S. Wang, D. Mao and C. Hu, *Fuel Process. Technol.*, 2018, **169**, 199-206.
10. D. Chen, R. Lødeng, A. Anundskås, O. Olsvik and A. Holmen, *Chem. Eng. Sci.*, 2001, **56**, 1371-1379.
11. A. W. Budiman, S.-H. Song, T.-S. Chang, C.-H. Shin and M.-J. Choi, *Catalysis Surveys from Asia*, 2012, **16**, 183-197.
12. O. Muraza and A. Galadima, *International Journal of Energy Research*, 2015, **39**, 1196-1216.
13. J. R. Rostrup-Nielsen, *Catalysis Today*, 1993, **18**, 305-324.
14. J. R. Rostrup-Nielsen, J. Sehested and J. K. Nørskov, in *Advances in Catalysis*, Academic Press, 2002, vol. 47, pp. 65-139.
15. M. Tang, L. Xu and M. Fan, *Applied Energy*, 2015, **151**, 143-156.
16. S. Assabumrungrat, S. Charoenseri, N. Laosiripojana, W. Kiatkittipong and P. Praserttham, *International Journal of Hydrogen Energy*, 2009, **34**, 6211-6220.
17. M. Zhang, J. Zhang, Y. Wu, J. Pan, Q. Zhang, Y. Tan and Y. Han, *Appl. Catal. B-Environ*, 2019, **244**, 427-437.
18. J. Juan-Juan, M. C. Román-Martínez and M. J. Illán-Gómez, *Applied Catalysis A: General*, 2006, **301**, 9-15.
19. M. Najera, R. Solunke, T. Gardner and G. Veser, *Chem. Eng. Res. Des.*, 2011, **89**, 1533-1543.
20. A. More, S. Bhavsar and G. Veser, *Energy Technology*, 2016, **4**, 1147-1157.
21. J. Guo, H. Lou and X. Zheng, *Carbon*, 2007, **45**, 1314-1321.
22. P. Lahijani, Z. A. Zainal, M. Mohammadi and A. R. Mohamed, *Renewable and Sustainable Energy Reviews*, 2015, **41**, 615-632.

8 CONCLUSION AND OUTLOOK



8.1 Summary of the thesis

Due to the resources and environment issues, effective utilisation of both CH₄ and CO₂ is crucial for modern industry, making the two processes attractive in C1 chemistry. However, the relatively inert property of these two molecules makes the two processes very challenging. To meet the challenge, the thesis focuses on three catalytic reactions aiming at utilising CH₄ and CO₂, oxidative coupling of methane (OCM), CO₂ methanation and dry reforming of methane (DRM).

Firstly, a versatile setup with online gas chromatograph (GC), infrared spectrometer and mass spectrometer (MS) as the detectors was designed and built in the lab (Chapter 2). The setup has a flexible gas controlling part with two electric-actuated 4-way valves. It enables both cofeed mode, namely steady state operation, and unsteady state operations, making it possible to conduct the reactions under different modes. A lab-designed furnace reactor was built, allowing the efficiently localised heating of the catalyst bed, meeting the high temperature requirement of OCM. A compact microwave reactor was also customized. Both furnace reactor and microwave reactor with an open window on the top, can be attached to the gas controlling component, allowing the study about the effect of different heating ways on the reaction, while the visualisation of temperature and catalyst bed is achieved with the USB camera and infrared camera. Besides, a spatial-resolved gas sampling and temperature measurement tool was built and integrated to the setup for the *operando* spatial analysis of gaseous concentration and temperature.

Secondly, catalytic OCM was conducted under steady state at different temperatures on MgO and La₂O₃ based catalysts (Chapter 3). CH₄ conversion and C₂ (C₂H₆ and C₂H₄) yield were higher obtained on La₂O₃ than that on MgO, especially at low temperature range (< 700 °C). The spatial analysis revealed that reactions fiercely took place in the front, the superiority of La₂O₃ was originated from its high selectivity to partial oxidation of CH₄ in the front of catalyst bed, which resulted in the larger temperature gradient in the front of catalyst bed by the burning of formed H₂. It further implies the irrationality of simply study the catalytic performance via the conventional method, analysing the gaseous composition of the effluent at the end of catalyst bed. Therefore, the unsteady-state operation was applied to study the intrinsic activity of

the catalysts. It confirmed the high activity of La_2O_3 towards partial oxidation reaction and the relatively higher C_2 selectivity of the lattice oxygen on MgO comparing to La_2O_3 . A homogeneously dominated reaction mechanism was proposed for OCM on the two simple metal oxides, MgO and La_2O_3 . With Sr dopant on La_2O_3 (Sr/ La_2O_3) and Li doping into MgO (Li/MgO), the catalytic behaviour was significantly changed, especially for Li/MgO. The spatial analysis suggested a different reaction mechanism for the doped catalysts, heterogeneously dominated reaction mechanism.

To further study the activity of MgO and La_2O_3 towards CH_4 activation, unsteady-state operation was applied in different modes (Chapter 4), i.e. reasonably arranging the gas fed into the reactor. The activity of different active oxygen species was discussed. On MgO, both lattice oxygen and strongly adsorbed oxygen species could activate CH_4 , lattice oxygen was more selective to C_2H_4 formation and mainly activated at high temperature (≥ 800 °C). Different from MgO, only one type of active oxygen species was assigned to activate CH_4 on La_2O_3 . Furthermore, this active oxygen site showed higher selectivity to CO formation without the presence of gaseous O_2 , which contributed to the lower intrinsic OCM activity of La_2O_3 than MgO.

Then, a customized microwave reactor was used to explore the possibility of inhibiting unselective oxidation of methyl radical in gas phase during OCM via changing the heating method (Chapter 5). By comparing the catalytic performance obtained with furnace and microwave reactor using the above MgO and La_2O_3 based catalysts, microwave heating demonstrated its advantage of enhancing CH_4 conversion and C_2 selectivity at low temperature (< 700 °C) via suppressing further oxidation of hydrocarbons in gas phase. A hotspot was observed in the middle of catalyst bed, which was caused by the nonuniformity of the catalyst material. The phenomenon counteracted the advantage of microwave heating at high temperature, deteriorating C_2 selectivity. To avoid that, the catalyst active to both microwave and OCM with uniform structure was important while applying microwave heating in OCM system.

Thirdly, targeting CO_2 utilisation, a novel CO_2 capture and reduction (CCR) approach was applied to CO_2 methanation (Chapter 6). The CCR approach enabled CO_2 capture and conversion steps in one isothermal process, allowing the direct utilisation of CO_2 in the industrial effluent, which made the process more economic than the conventional CO_2 capture and storage strategy. In the thesis, ZrO_2 supported Ni

(Ni/ZrO₂) catalysts with two promoters, K and La, were investigated to implement CCR process. Although K increased the capacity CO₂ capture more significantly than La, La enhanced the rate of CO₂ methanation and made the efficient utilisation of H₂, while K slowed down CO₂ methanation process in H₂ feed. H₂-temperature-programmed reduction (H₂-TPR), reductive CO₂-temperature-programmed desorption in H₂ atmosphere (reductive CO₂-TPD) revealed that La improved the reducibility of Ni/ZrO₂ without changing formate-mediated reaction mechanism proved by space- and time-resolved *operando* (DRIFTS). The *operando* DRIFTS also showed that K promotion led to the formation of different intermediates, formyl species cooperated with bidentate carbonates, which resulted in the slower CO₂ methanation process, especially at low temperature (< 350 °C). The study proved the potential of conducting CO₂ methanation at low temperature (250 °C) via CCR process with La-promoted Ni/ZrO₂. K could be an effective promoter for catalysts used at high temperature (>350 °C) for CCR process.

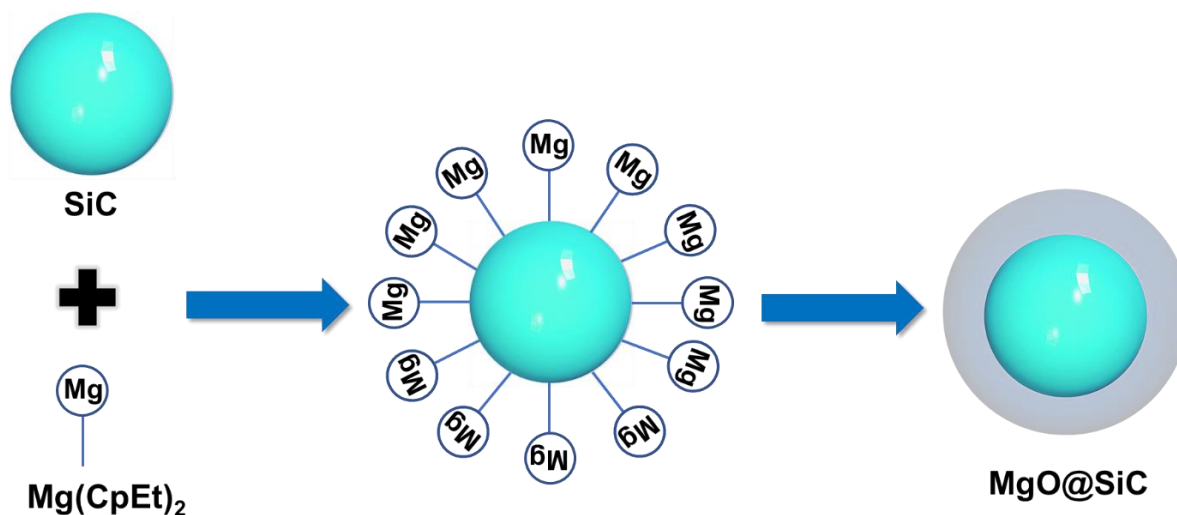
At the end, the study focused on the reaction combining CH₄ and CO₂ utilisation, dry reforming of methane (DRM). Based on the reaction mechanism of DRM, the reaction was split into two independent process, CH₄ decomposition to coke and coke re-oxidation by CO₂, to meet the challenge of catalyst deactivation in the cofeed DRM. It was also called chemical looping dry reforming of methane (CLDR). Ni-based catalyst was used in the work due to its proved activity to DRM. ZrO₂ was selected firstly as the optimal support among three support materials, SiO₂, Al₂O₃ and ZrO₂, for further investigation. By performing CLDR at different temperatures with Ni/ZrO₂, high temperature was found to benefit both CO₂ conversion and CH₄ decomposition processes, especially for the former process. After that, the role of three promoters, Fe, K and La was investigated. Among them, La gave the best promotion on both two processes, while Fe led to over-oxidation of CH₄ during CH₄ decomposition process via strongly increasing the oxidizability of the Ni/ZrO₂, and K was detrimental to both processes. Besides, the types of coke formed during CH₄ decomposition was believed to affect the kinetics of its re-oxidation by CO₂ to produce CO. Further studying with *operando* Raman and transmission electron microscope (TEM) should help to clarify the phenomenon.

8.2 Outlook

CH₄ and CO₂ functionalisation play critical role in building sustainable carbon cycle for modern industrials. As well known, the challenge lies in activating the thermodynamically stable CH₄ and CO₂ molecule and guiding them to form more valuable products. The thesis has made effort on this topic via elucidating the real obstacles in implementing OCM, exploring the possibility of applying more economic and industrially operable approaches to CO₂ hydrogenation and DRM.

According to the study of catalytic OCM, we have learnt that the oxidation of hydrocarbons by gaseous O₂ is the main culprit for the loss of C₂ selectivity in cofeed OCM (Chapter 3), which can be suppressed via using microwave heating that selectively heats the catalyst (Chapter 5). To apply microwave heating to OCM, the catalyst that has both high intrinsic activity to OCM and strong adsorption of microwave radiation is required. Furthermore, the structure of the catalyst has to be uniform to avoid hotspot, as indicated in Chapter 5. MgO is proved to have relatively high intrinsic OCM activity at high temperature (≥ 800 °C) via unsteady state operations in Chapter 4. However, MgO is relatively inert to microwave radiation, while SiC that is inert to OCM has strong adsorption of microwave radiation.

Hence, integrating the two materials together in a core-shell structure with SiC as the core (MgO@SiC) could be the solution. Atomic layer deposition method (ALD) could be used to synthesize MgO@SiC, due to its specializing in synthesis of nanomaterials with core-shell structure¹⁻⁴. As reported, Bis(ethylcyclopentadienyl) magnesium (Mg(CpEt)₂) has been successfully used as the precursor for forming the shell of MgO⁵. With the nanosized SiC, it is possible to get MgO@SiC with ALD, as shown in Scheme 8.1. After obtaining MgO@SiC with uniform structure, it should exert the advantage of microwave heating in OCM system, efficiently enhancing C₂ yield.



Scheme 8.1 Synthesis of MgO@SiC with Bis(ethylcyclopentadienyl) magnesium ($\text{Mg}(\text{CpEt})_2$) and nanosized SiC via ALD.

For CH_4 functionalization in DRM, microwave heating could also be interesting. Its positive effect has already been demonstrated with Ru-doped SrTiO_3 perovskite catalysts during DRM in co-feed mode⁶. Regarding to CLDR, microwave heating could significantly lower down the temperature required for CO_2 conversion based on theoretical calculation, as shown in Figure 8.2⁷. In CLDR, CO_2 conversion process has higher temperature dependence than CH_4 conversion (Chapter 7). This makes CO_2 conversion lower than CH_4 conversion in isothermal condition. To achieve CO_2 and CH_4 conversion in the stoichiometric ratio, the function of microwave demonstrated in Figure 8.2 meet exactly the challenge. Meanwhile, the Ni-based catalysts studied for CLDR in Chapter 7 showed considerable adsorption of microwave radiation in our preliminary test. Hence, the catalysts active to DRM could be directly used in microwave reactor. In a conclusion, applying microwave heating to CLDR is a promising strategy to improve the catalytic performance.

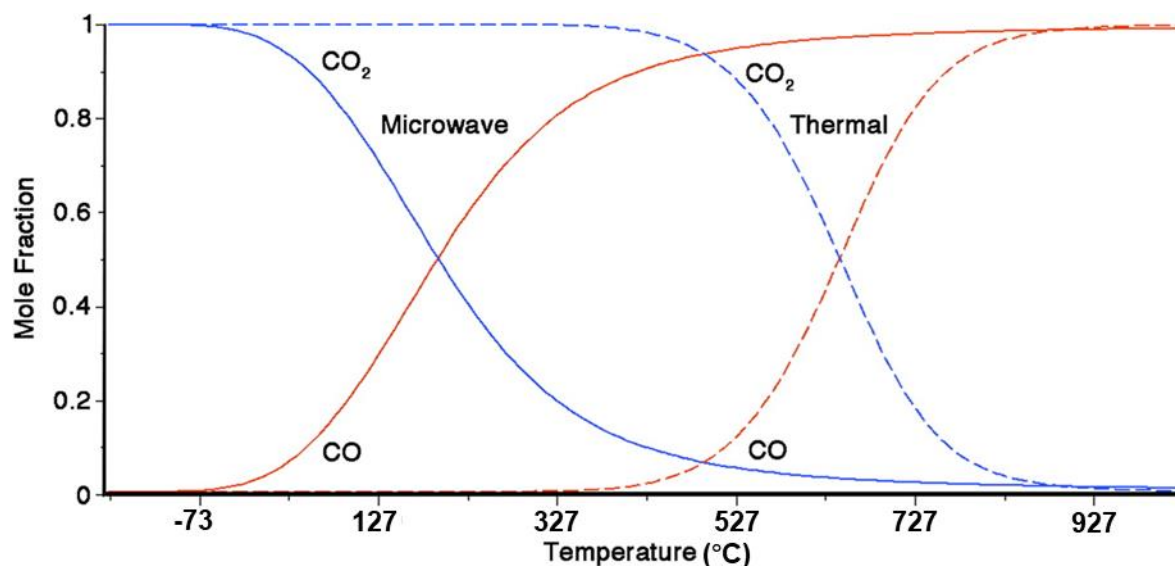


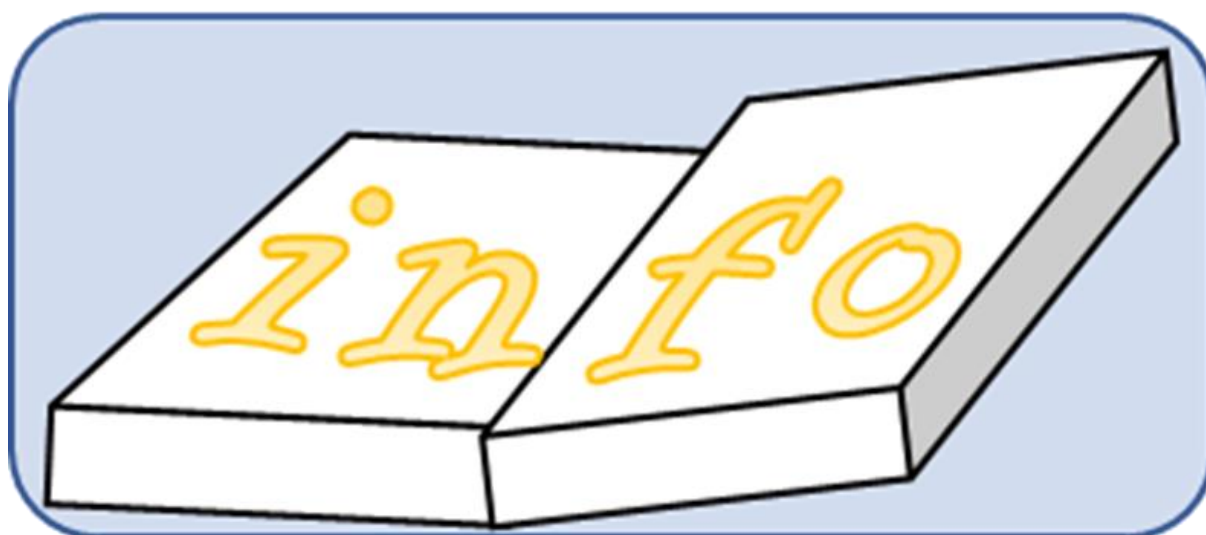
Figure 8.2. Mole fraction of CO (red line) and CO₂ (blue line) as a function of temperature for the microwave (solid) and thermal (dashed) Boudouard reaction, predicted from the calculated equilibrium constants and assuming 1 atm of pressure⁷.

In addition, the selective heating of the catalyst via microwave enables fast change of the catalyst temperature. Therefore, microwave heating is also advantageous for non-isothermal operation. This expands the potential of microwave heating in those chemical-looping type reactions, such as our CCR process and CLDR.

Bibliography

1. V. Ganapathy, B. Karunakaran and S.-W. Rhee, *J. Power Sources*, 2010, **195**, 5138-5143.
2. M. J. Weber, A. J. M. Mackus, M. A. Verheijen, C. van der Marel and W. M. M. Kessels, *Chem. Mater.*, 2012, **24**, 2973-2977.
3. H. Wang, C. Wang, H. Yan, H. Yi and J. Lu, *J. Catal.*, 2015, **324**, 59-68.
4. F. Kayaci, S. Vempati, C. Ozgit-Akgun, I. Donmez, N. Biyikli and T. Uyar, *Nanoscale*, 2014, **6**, 5735-5745.
5. M.-G. Jeong, S. Y. Kim, D. H. Kim, S. W. Han, I. H. Kim, M. Lee, Y. K. Hwang and Y. D. Kim, *Applied Catalysis A: General*, 2016, **515**, 45-50.
6. L. S. Gangurde, G. S. J. Sturm, M. J. Valero-Romero, R. Mallada, J. Santamaria, A. I. Stankiewicz and G. D. Stefanidis, *Chemical Engineering and Processing - Process Intensification*, 2018, **127**, 178-190.
7. J. Hunt, A. Ferrari, A. Lita, M. Crosswhite, B. Ashley and A. E. Stiegman, *J. Phys. Chem. C*, 2013, **117**, 26871-26880.

9 APPENDICES



Appendix A Supporting information of Chapter 3

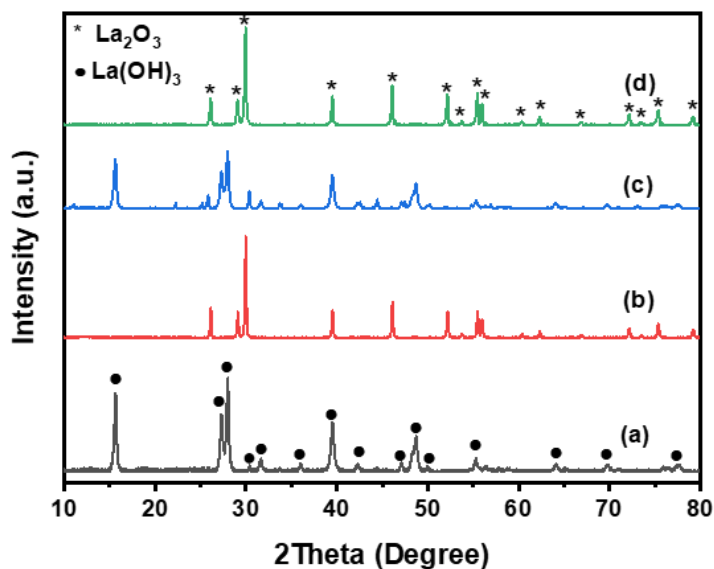


Figure 9.1 XRD profile of La_2O_3 sample with different treatment: (a) directly purchased La_2O_3 ; (b) after calcining (a) at $700\text{ }^\circ\text{C}$ in air for 5 h; (c) after keeping (b) in a closed sample vial at room temperature for 1 day; (d) after calcine (a) in 50 vol.% O_2 in He (50 mL/min) at $700\text{ }^\circ\text{C}$ for 30 min

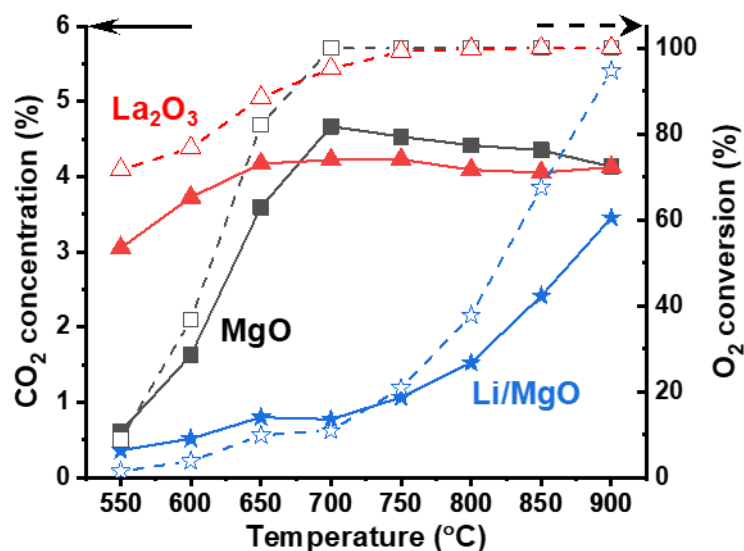


Figure 9.2 Comparison of OCM catalytic behaviour over MgO (black), La₂O₃ (red) and Li/MgO (blue) in terms of CO₂ concentration (solid lines) and O₂ conversion (dash lines).

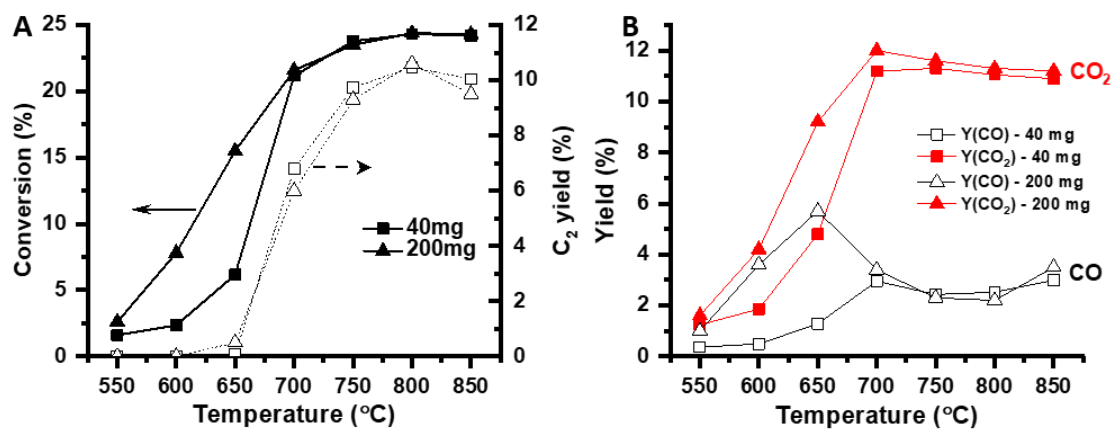


Figure 9.3 Comparison of catalytic performance over MgO with different amount (40 mg and 200 mg) in terms of CH₄ conversion & C₂ yield (A) and CO & CO₂ yield (B)

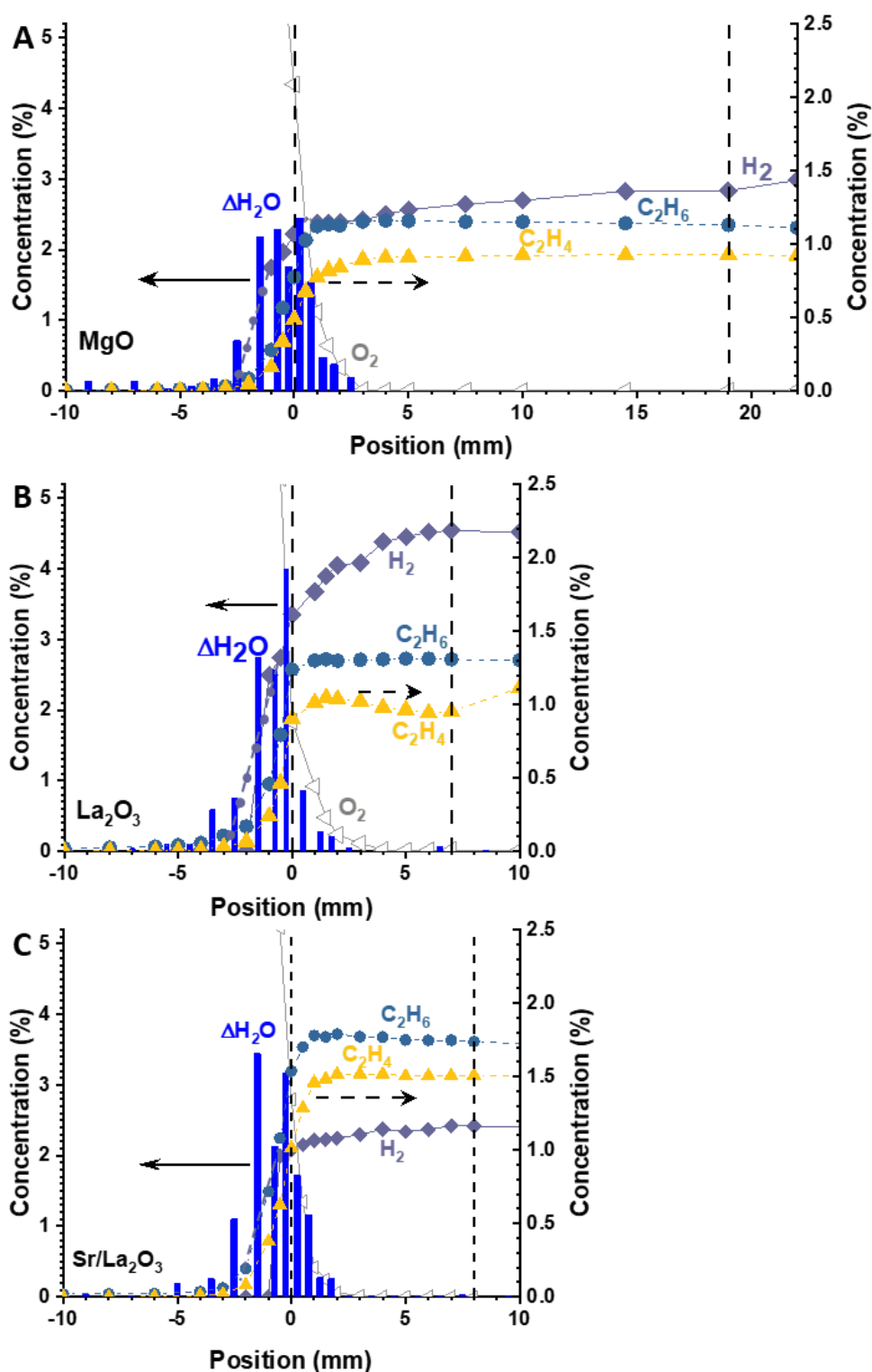


Figure 9.4 Spatial concentration profiles of O_2 , C_2H_6 , C_2H_4 , H_2 and formed water (ΔH_2O) measured on MgO (A), La_2O_3 (B) and Sr/La_2O_3 (C) during OCM under steady state operation at 800 °C. ΔH_2O is the difference value

between H₂O amount at one position and H₂O amount at previous front neighbour position, H₂O amount is calculated based oxygen balance.

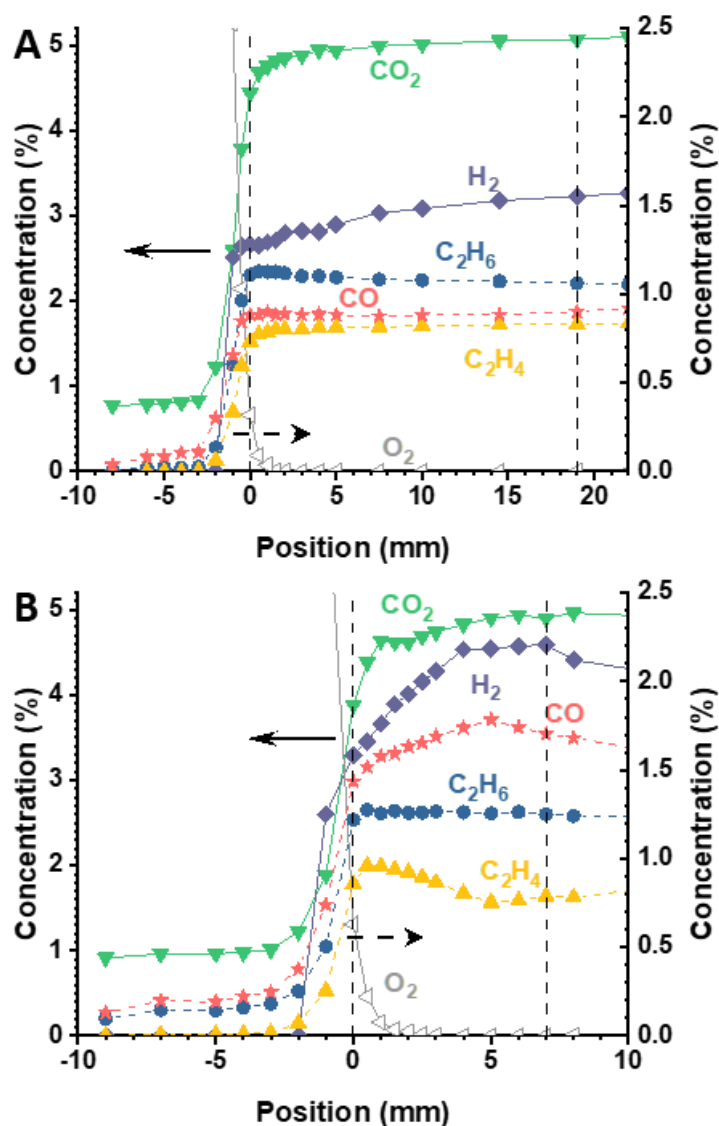


Figure 9.5 Spatial concentration profile of O₂, C₂H₆, C₂H₄, CO₂, CO and H₂ during OCM under steady state operation over MgO (A) and La₂O₃ (B) with 4 mm SiC in front at 800 °C

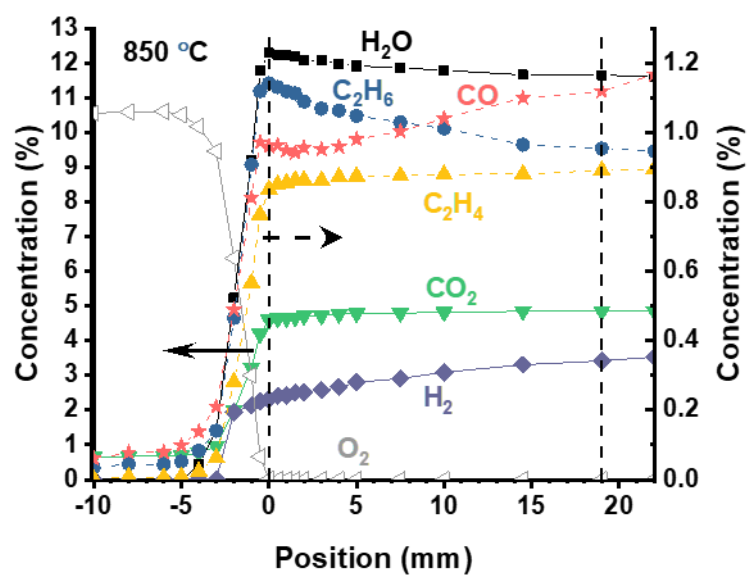


Figure 9.6 Spatial concentration profile of O₂, C₂H₆, C₂H₄, CO₂, CO, H₂O and H₂ during OCM under steady state operation over MgO at 850 °C, H₂O is calculated based oxygen balance

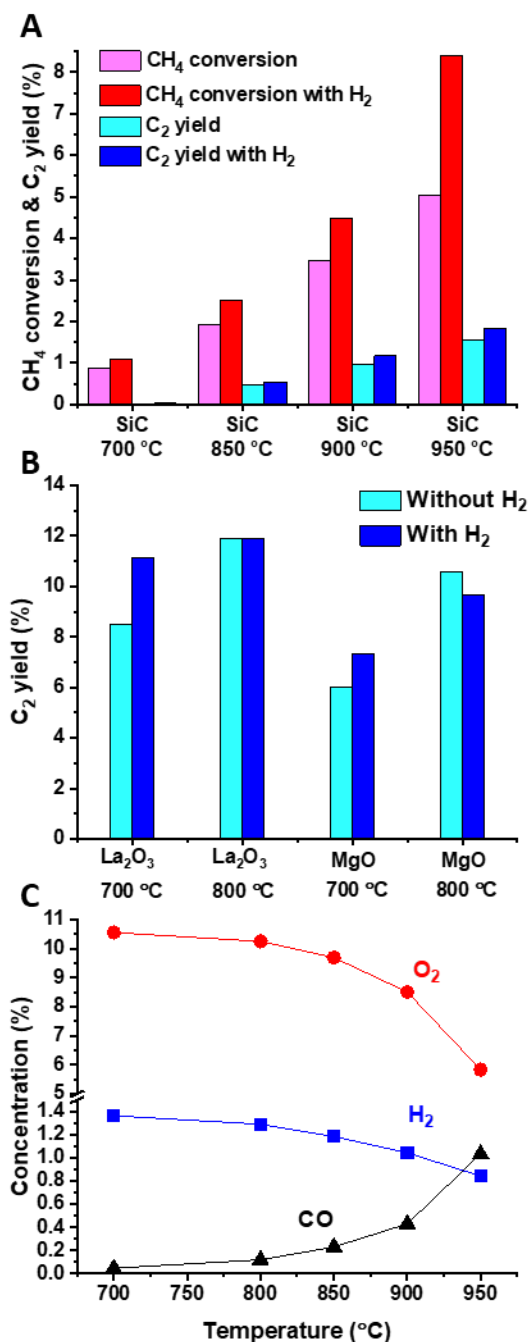


Figure 9.7 CH₄ conversion and C₂ yield during OCM over SiC (A) and C₂ yield during OCM over La₂O₃ and MgO (B) with/without H₂ in the feed under steady state operation at different temperatures, and concentration of O₂, H₂ and CO during OCM over SiC with H₂ in the feed under steady state operation (C). It shows H₂ addition participates in O₂ consuming and lifts up CH₄ conversion and C₂ yield when SiC is applied, and it enhances C₂ yield at 700 °C but lowers that at 800 °C when La₂O₃ and MgO are used. The harm to C₂ yield at high temperature of H₂ addition is because that the

temperature rise caused by H₂ burning shifts the reaction system to its activity dropping range (≥ 850 °C).

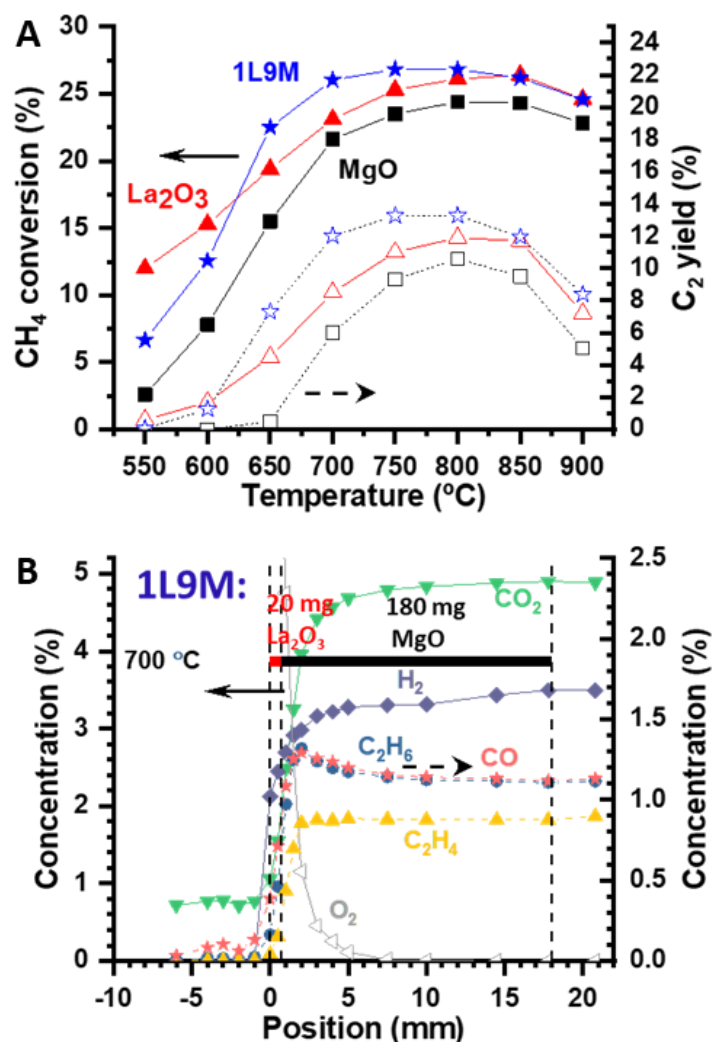


Figure 9.8 Comparison of OCM catalytic activity over La₂O₃, MgO and 1L9M under steady state operation at different temperatures in terms of CH₄ conversion and C₂ yield (A), and spatial concentration profile of O₂, C₂H₆, C₂H₄, CO₂, CO and H₂ during OCM under steady state operation over 1L9M (B).

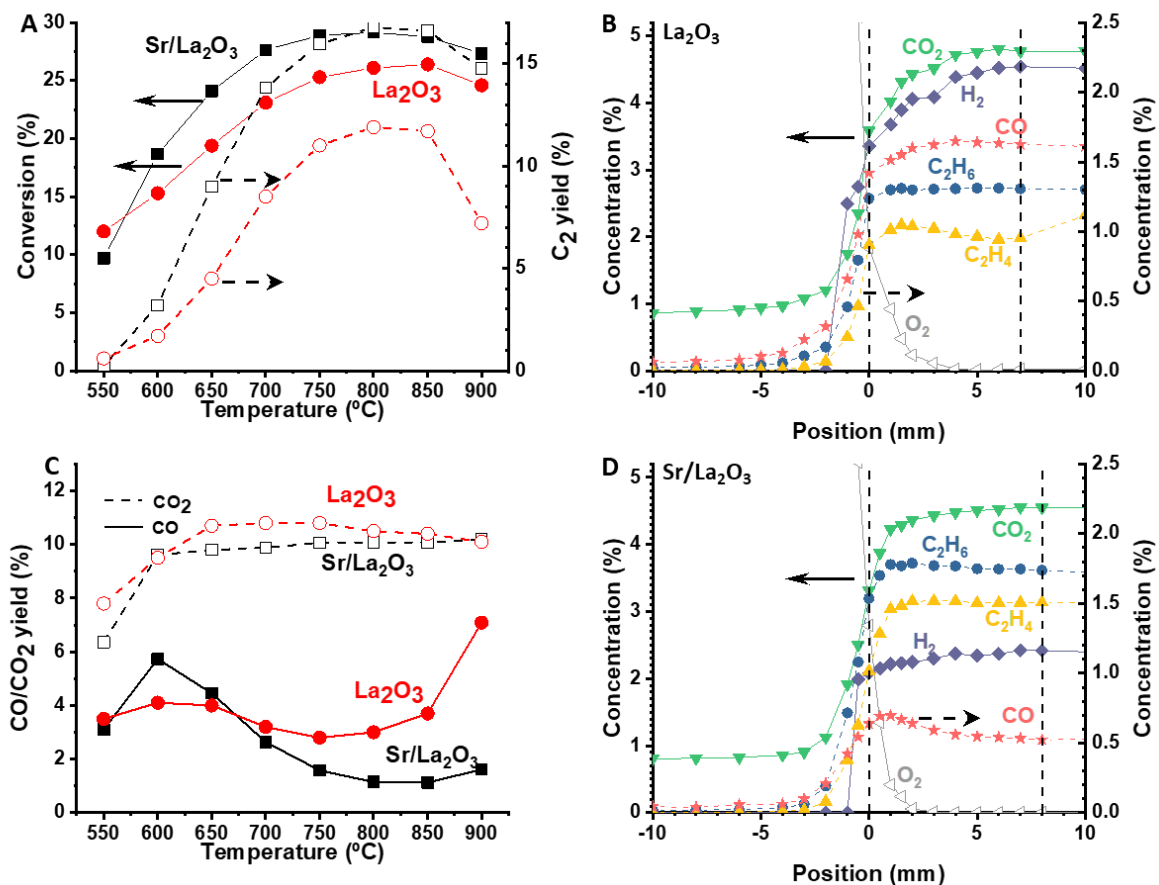


Figure 9.9 Comparison of La₂O₃ and Sr/La₂O₃ catalytic activity in terms of CH₄ conversion & C₂ yield (A), CO&CO₂ yield (C) and spatial gas concentration profile of O₂, C₂H₆, C₂H₄, CO₂, CO and H₂ during OCM under steady state operation over La₂O₃ (B) and Sr/La₂O₃ (D) at 800 °C.

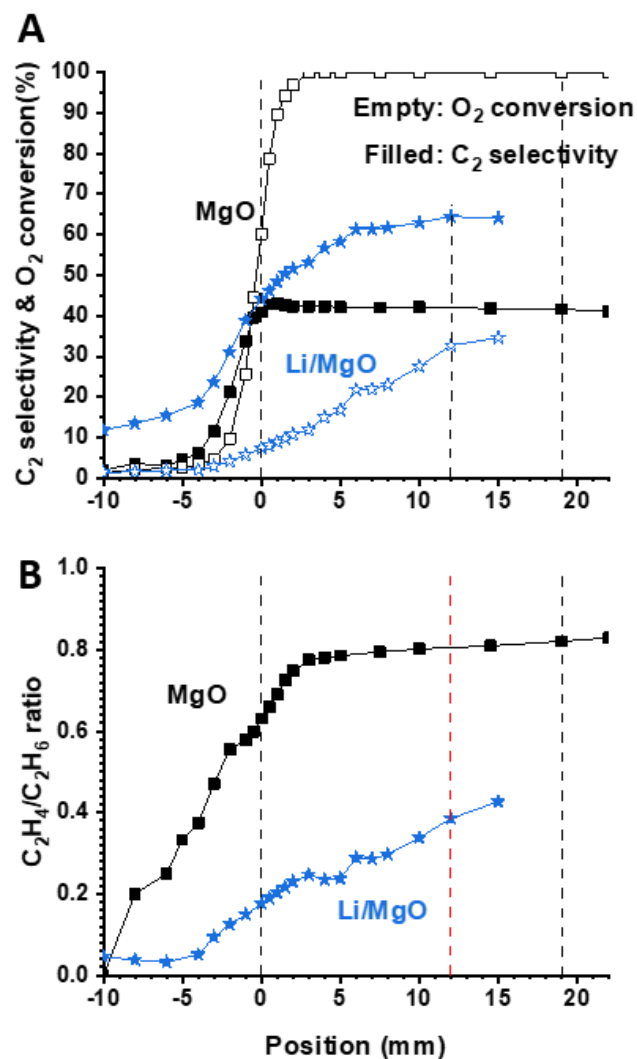


Figure 9.10 Comparison of MgO (black) and Li/MgO) spatial catalytic behaviour in terms of C₂ selectivity, O₂ conversion (A) and the ratio of C₂H₄/C₂H₆ (B)

SHORTHAND AND GLOSSARY

$\Delta H^\circ_{298\text{ K}}$	Standard enthalpy of reaction
BET	Brunauer-Emmett-Telle
C₂	Ethane and ethylene
CCR	CO ₂ capture and reduction
CLDR	Chemical looping of dry reforming of methane
CO_x	CO and CO ₂
DRIFTS	Diffuse Reflectance Infrared Fourier Transform Spectroscopy
DRIFTS-MS	Diffuse reflectance infrared Fourier Transform spectroscopy combined with mass spectrometric
DRM	Dry reforming of methane
F phase	Flushing phase
FID	Flame Ionization Detector
FT	Fischer-Tropsch
GC	Gas chromatography
H₂-TPR	H ₂ temperature programmed reduction
ID	Inner diameter
IR	Infrared
MFC	Mass flow controller
MIESR	Matrix isolation electron spin resonance
MPI-TOFMS	Multiphoton ionization time-of-flight mass spectrometry
MS	Mass spectrometry

MTO	Methanol to olefins
MWCNT	Multiwall carbon nanotubes
OCM	Oxidative coupling of methane
OD	Outside diameter
ODH	Oxidative dehydrogenation of ethane
P	Product
PI	Pressure indicator
PID	Proportional–integral–derivative
PXRD	Power X-ray diffraction
Re	Reactant
RWGS	Reverse water gas shift reaction
SRM	Steam reforming of methane
SVUV-PIMS	Synchrotron vacuum ultraviolet photoionization mass spectroscopy
TCD	Thermal conductivity detector
TEM	Transmission Electron Microscopy
X phase	Oxidant phase
XANES	X-ray absorption near edge structure spectroscopy
Y phase	Reductant phase

LIST OF PUBLICATIONS

Journal publications

1 Continuous CO₂ capture and reduction in one process: CO₂ methanation over unpromoted and promoted Ni/ZrO₂.

Lingjun Hu and Atsushi Urakawa. *Journal of CO₂ Utilization* 25 (2018): 323-329.

2 CO₂ activation over catalytic surfaces.

Andrea Álvarez, Marta Borges, Juan José Corral-Pérez, Joan Giner Olcina, **Lingjun Hu**,

Damien Cornu, Rui Huang, Dragos Stoian, and Atsushi Urakawa. *ChemPhysChem* 18 (2017): 3135-3141.

3 Fe, Pd Co-Incorporated LaCoO₃ Perovskites: Modification of Thermal Stability and Catalytic Activity for Gasoline Vehicle Exhaust Purification.

Lingjun Hu, Chen Zhou, Chunzheng Wu, Shenghu Zhou, Wei Guo Wang, Hongfeng Yin. *European Journal of Inorganic Chemistry* 13 (2015): 2317-2322.

4 Solvothermal synthesis of Fe-doping LiMnPO₄ nanomaterials for Li-ion batteries.

Lingjun Hu, Bao Qiu, Yonggao Xia, Zhihong Qin, Laifen Qin, Xufeng Zhou, Zhaoping Liu. *Journal of Power Sources* 248 (2014): 246-252.

5 Synthesis, Characterization, and Catalytic Activity of Mn-doped Perovskite Oxides for Three-Way Catalysis.

Chen Zhou, Yexin Zhang, **Lingjun Hu**, Hongfeng Yin, Wei Guo Wang. *Chemical Engineering Technology* 38 (2015): 291-296.

6 Enhanced catalytic activity for NO oxidation over Ba doped LaCoO₃ catalyst.

List of publications

Chen Zhou, Zijian Feng, Yexin Zhang, **Lingjun Hu**, Rong Chen, Bin Shan, Hongfeng Yin, Wei Guo Wang, Aisheng Huang. *RSC Advances* 5(2015): 28054-28059.

Book Chapter publications

1 Active reactions and spatial gradients in oxidative coupling of methane.

Lingjun Hu, Donato Pinto, and Atsushi Urakawa. *Catalysis* 32 (2020): 203-223.

Conference contributions

1 Ni-based catalysts for CO₂ methanation via CO₂ capture and reduction.

June 2017, 1st ICIQ PhD Day, Tarragona (Spain): **Oral (flash) presentation.**

2 Ni-based catalysts for CO₂ methanation via CO₂ capture and reduction.

August **2017**, 13th European Congress on Catalysis - A bridge to the future, Florence (Italy) – **Poster presentation.**

3 Continuous CO₂ capture and reduction in one process: CO₂ methanation by unpromoted and promoted Ni/ZrO₂.

June 2018, 2nd ICIQ PhD Day, Tarragona (Spain): **Poster presentation.**

4 Catalytic oxidative coupling of methane: homogeneous or heterogeneous reaction?

October **2019**, 16th Netherlands Process Technology Symposium (NPS-16), Eindhoven (Netherlands) – **Oral presentation.**

CURRICULUM VITAE

PERSONAL INFORMATION

Name: Lingjun Hu
Date of Birth: May 12th, 1990
Nationality: Chinese
Email: lindhotch@gmail.com

Education

PhD student *Chemical Science and Technology*
NOV. 2015 – PRESENT Institute of Chemical Research of Catalonia (ICIQ), Tarragona, Spain

M. Eng. *Materials Physics and Chemistry*
JULY. 2013 – JULY. 2015 Ningbo Institute of Material Technology and Engineering (NIMTE), Chinese Academy of Science, Ningbo, China

SEPT. 2012 – JULY. 2013 University of Chinese Academy of Sciences (UCAS), Beijing, China

B. Eng. *Materials Science and Engineering*
SEPT. 2008 – Hainan University, Haikou, China
JUNE. 2012

Research Experience

NOV. 2015 – **PhD student**
PRESENT *Institute of Chemical Research of Catalonia (ICIQ), Tarragona, Spain*
Heterogeneous catalysis in CO₂ hydrogenation, oxidative coupling of methane (OCM) and dry reforming of methane (DRM) reactions

Applied a novel strategy- CO₂ capture and reduction (CCR)-to CO₂ methanation based on unpromoted and promoted Ni/ZrO₂.

Studying OCM reaction based on single metal oxides under steady and unsteady state modes with spatial analysis and visualization technologies.

Applying chemical looping strategy to DRM based on supported Ni catalysts.

JULY. 2011 – JUNE. 2015 **Graduate student**

*Ningbo Institute of Material Technology and Engineering,
Chinese Academy of Science, Ningbo, China*

Perovskites as three-way catalysts

Studied the effect of B-site doping on the catalytic performance of LaCoO₃ and investigated the mechanism of improvement.

JULY. 2019 – MAR. 2020 **Visiting PhD student**

Delft University of Technology (TU Delft), Delft, Netherlands

Heterogeneous catalysis in dry reforming of methane (DRM) reaction

Applying chemical looping strategy to DRM based on supported Ni catalysts.

FEB. 2012 – SEP.2012 **Internship**

*Ningbo Institute of Material Technology and Engineering,
Chinese Academy of Science, Ningbo, China*

Cathode materials for lithium ion batteries

Synthesized Fe-doped LiMnPO₄ with different morphologies via solvothermal method; investigated electrochemical performance of as-synthesized materials.

NOV. 2008 – DEC. 2011 **Undergraduate (Learning in a lab during extracurricular time)**

Hainan University, Haikou, China

Bacterial cellulose as biomedical materials

Participated in the graduate research projects on the biosynthesis and biocompatibility investigation of bacterial cellulose.

Skills

Lab skills:	<p>Experience in material synthesis with wet impregnation, ball-milling, solvothermal, sol-gel and soft-templated methods;</p> <p>Experience in material characterization tools such as TEM, SEM, XRD, ICP, BET, TPR, TPD and general electrochemical characterizations;</p> <p>Heterogeneous catalysis study with operando DRIFTS and spatial analysis;</p> <p>Reaction set-ups and analysis tools design and building</p>
Computer skills:	MATLAB, AutoCAD, LabVIEW, Visual Basic and Python
Languages:	Chinese (Native), English (IELTS: 6.5); French (Beginner)

